Étude de la formation et de l'activité catalytique de nanoparticules durant les premiers instants de la croissance de nanotubes de carbone par dépôt chimique en phase vapeur assisté par aérosol

Yang Ma

To cite this version:

Yang Ma. Étude de la formation et de l'activité catalytique de nanoparticules durant les premiers instants de la croissance de nanotubes de carbone par dépôt chimique en phase vapeur assisté par aérosol. Autre. Université Paris Saclay (COmUE), 2016. Français. NNT : 2016SACLC047 . tel-01369840

HAL Id: tel-01369840
https://theses.hal.science/tel-01369840v1

Submitted on 21 Sep 2016

NNT : 2016SACLC047

THESE DE DOCTORAT
DE
L'UNIVERSITE PARIS-SACLAY
PREPAREE A
CENTRALESUPELEC

ECOLE DOCTORALE N° 579
Sciences mécaniques et énergétiques, matériaux et géosciences

Spécialité de doctorat: Génie Mécanique

Par

M. Yang MA

Étude de la formation et de l'activité catalytique de nanoparticules durant les premiers instants de la croissance de nanotubes de carbone par dépôt chimique en phase vapeur assisté par aérosol

Thèse présentée et soutenue à CentraleSupélec, Châtenay-Malabry, le 30 juin 2016 :

Composition du Jury :

M. Christophe LAURENT	Directeur du CIRIMAT, Université de Toulouse	Président
Mme Alix GICQUEL	Directrice du Labex SEAM, Université Paris 13 - CNRS	Rapporteur
Mme Catherine JOURNET-GAUTIER	Professeur des Universités - UCB Lyon1	Rapporteur
M. Anthony DICHIARA	Professeur adjoint, University of Washington Seattle	Examinateur
M. Laurent ZIMMER	Chargé de recherche, CentraleSupélec	Co-encadrant de thèse
M. Jinbo BAI	Directeur de Recherche, CentraleSupélec	Directeur de thèse

Titre : Étude de la formation et de l'activité catalytique de nanoparticules durant les premiers instants de la croissance de nanotubes de carbone par dépôt chimique en phase vapeur assisté par aérosol

Mots clés : Nanotube de carbone ; Catalytique ; Nanoparticules ; Dépôt chimique en phase vapeur ; in-situ diagnostic ; Laser-induced incandescence

Résumé : De par leurs propriétés remarquables, les nanotubes de carbone (NTCs) reçoivent beaucoup d'attention et de nombreuses recherches sont menées sur ces matériaux depuis les dernières décennies. Le nombre d'applications envisagées mais aussi la quantité demandée de NTCs augmentent chaque année. Pour atteindre une production à grande échelle et contrôlée, il est nécessaire d'avoir une bonne compréhension des mécanismes de croissance des NTCs. Dans ce manuscrit, la formation de nanoparticules (NPs) par dépôt chimique en phase vapeur assisté par aérosol (CVD) sont étudiées expérimentalement, pour analyser le processus d'évolution des NPs et leur relation avec les NTCs.

Dans le chapitre 1, nous présentons une introduction générale sur des structures, les méthodes de synthèse, les propriétés et les applications envisagées des NTCs, ainsi que l'état de l'art concernant l'étude des mécanismes de croissance des NTCs.

Dans le chapitre 2, nous décrivons le système de dépôt chimique en phase vapeur avec catalyseur flottant, ainsi que les méthodes de diagnostic in- situ/ex-situ utilisées dans cette étude. La technique d'incandescence induite par laser (LII) est particulièrement importante dans ce chapitre, car cette technique nous permet de réaliser un diagnostic in situ sur la quantité/taille des NPs déposées pendant le processus de synthèse.

Dans le chapitre 3, nous présentons l'évolution des NPs lors de la synthèse ainsi que les influences des différents paramètres de CVD (température, quantité de carbone/catalyseur, composition du gaz, etc.) sur les gouttelettes et les NPs respectivement. Un modèle pour la formation de NPs est proposé à la fin de ce chapitre.

Dans le chapitre 4, les résultats des expériences sur l'évolution de la composition du gaz sont révélés. Ces résultats donnent des informations concernant les réactions chimiques ayant lieu dans la phase gazeuse lors de la synthèse des NTCs.

Dans le chapitre 5, une étude détaillée de l'influence des paramètres de CVD sur les produits NTCs est menée, et les relations entre les NPs et les NTC sont discutées.

Pour finir, des conclusions générales ainsi que les perspectives prévues pour les travaux futurs sont présentées

Title : Study on the formation and catalytic activity of nanoparticles in early stages of carbon nanotubes growth under aerosol-assisted chemical vapor deposition

Keywords : Carbon nanotube; Catalytic; Nanoparticles; Chemical vapor deposition; in-situ diagnostic; Laser-induced incandescence

Abstract : Due to the outstanding properties in various aspects, carbon nanotubes (CNTs) received worldwide attentions and intensive investigations are carried out in the last decades. While the number of applications as well as the quantity demanded of CNTs are increasing year after year, to achieve large scale production of the desired structures in a controlled way, it is highly required having a clear understanding about the CNTs growth mechanism. In this study, the formation of nanoparticles (NPs) under aerosol-assisted chemical vapor deposition (CVD) is experimentally investigated, aiming to study the NPs evolution process and their relation with the CNTs products.

In chapter 1, we provide a general review of CNTs structures, synthesis methods, properties as well as applications. Moreover, the current situation of CNTs growth mechanism study is presented.

In chapter 2, the floating catalyst chemical vapor deposition synthesis system, and the in-situ/ex-situ diagnostic methods used in this study are introduced. Laser induced incandescence technique (LII) is particularly explained in this chapter, which permits to achieve an in-situ diagnostic of the NPs quantity/size during the synthesis process.

In chapter 3, the evolution of NPs during the synthesis is presented, in which the influences of different CVD parameters (temperature, carbon/catalyst quantity, gas composition etc.) on the droplets as well as on the NPs are investigated respectively. A NPs formation model is proposed based on the NPs variation information at the end of this chapter.

In chapter 4, the experimental results of the gas composition evolution in chemical vapor deposition reactor are revealed, which reflect the gas phase chemical reactions information during the CNTs synthesis.

In chapter 5, a detailed investigation about the influence of CVD parameters on the CNTs products is explained. And the relation between the NPs and CNTs is discussed.

In the end, general conclusions are formed according to works and perspectives are provided for the improvement of the future work.

Acknowledgement

First of all, I would like to express my most sincere appreciation to Professor Jinbo BAI, under his supervision this work was done. I also would also like to express my sincere gratitude to my co-encadrant Mr. Laurent ZIMMER for his continuous support on my PhD study and related research works. Their constant encouragement, guidance, suggestions and time were invaluable. I learned a lot from them: hard-working spirit, serious attitude towards research, etc. Meanwhile, I feel very grateful for the financial support from China Scholarship Council (CSC).

I would like to thank the members of the jury: Madame Alix GICQUEL and Madame Catherine JOURNET-GAUTIER who had the difficult task to make a report on my manuscript, Monsieur Anthony DICHIARA, Monsieur Christophe LAURENT et Monsieur Philippe SERP who made me the honor to examine my work.

Special gratitude is extended to engineers of laboratory who have helped me to do the measurements: Monsieur Thomas REISS for SEM, Monsieur Paul HAGHI-ASHTIANI for TEM, and Madame Pascale GEMEINER for Raman. I am also indebted to Madame Djebarri FARIDA, Konate SOKONA, Monsieur Perrin ERIC as well as all staffs of Lab. MSSMat, I would like to express my thanks for their assistance.

I also owe my sincere gratitude to my friends and my fellows who gave me their help and I treasure the time we have spent together: Ahlem RAIES, Benhui FAN, Delong HE, Lynda BELKADI, Minhao YANG, Salem DIANA, Shan FENG, Weikang LI, Xiaoxin LU, Yiguo XU, Yu LIU.

My thanks go to my beloved parents for their loving consideration and great confidence in me all through these years. I hope that I can make them proud of me and I will be able to spend more time with them in the future.

Content

Acronyms and Symbols

Acronyms

AFM	Atomic Force Microscopy
CNTs	Carbon Nanotubes
CVD	Chemical Vapor Deposition
DTG	Derivative Thermogravimetric Analysis
FCCVD	Floating catalyst chemical vapor deposition
FWHM	Full width at half maximum
EDS	Energy Dispersive Spectrometer
GPC	Gas Phase Chromatography
HAADF	High-Angle Annular Dark-Field imaging
HRTEM	High-resolution transmission electron microscopy
LIBS	Laser Induced Breakdown Spectroscopy
LIF	Laser Induced Fluorescence
LII	Laser Induced Incandescence
MS	Mass Spectrometry
MWNTs	Multi-Walled Carbon Nanotubes
NP	Nanoparticle
PMT	Photomultiplier
SEM	Scanning Electron Microscope
SWNTs	Single-Walled Carbon Nanotubes
TEM	Transmission Electron Microscope
TGA	Thermogravimetric Analysis
TRLII	Time Resolved Laser Induced Incandescence
VdW	Van der Waals

Symbols

a	Length of unit vector
c	Speed of light (2.998×10^{10} cm/s)
$\overline{C}$	Chiral vector
C_{p_g}	Molecular heat capacity of gas ($\mathrm{J \cdot mol^{-1} \cdot K^{-1}}$)
C_{p_p}	Specific heat of nanoparticle ($\mathrm{J \cdot g^{-1} \cdot K^{-1}}$)
d	CNTs diameter
D_p	Diameter of the nanoparticle (nm)
D_{tube}	Inner diameter of the quartz tube (cm)
$E(m)$	Dimensionless refractive index
F_{gas}	Total gas flow rate ($\mathrm{L \cdot min^{-1}}$)
F_{H_2}	Hydrogen flow rate ($\mathrm{L \cdot min^{-1}}$)
h	Planck constant ($6.626 \times 10^{-34}\,\mathrm{J \cdot s}$)
ΔH_V	Average enthalpy of formation of sublimed carbon species ($\mathrm{J \cdot mol^{-1}}$)
k_B	Boltzmann constant ($1.381 \times 10^{-23}\,\mathrm{J \cdot K^{-1}}$)
L_C	Length of the chiral vector C
L_{tube}	Length of the quartz tube (cm)
n_i	Amount of substance for the gas component i (mol)
M	Nanoparticle mass (g)
m_g	Average gas molecular weight ($\mathrm{g \cdot mol^{-1}}$)
n	Levels of the Taguchi factor
P_{H_2}	Hydrogen percent in the gas (%)
p_V	Average partial pressure of sublimed carbon species (bar)

P_g	Gas pressure (Pa)
p_{ref}	Reference pressure in Antoine and Clausius-Clapeyron equations (Pa)
$q(t)$	Laser temporal intensity ($\mathrm{J \cdot cm^{-2}}$)
$\dot{Q}_{abs}$	Rate of energy gained by laser absorption (J)
$\dot{Q}_{cond}$	Rate of energy lost by conduction to the surrounding gases (J)
$\dot{Q}_{rad}$	Rate of energy lost by radiative emission (J)
$\dot{Q}_{\mathrm{Sub}}$	Rate of energy lost by sublimation and photo desorption (J)
r_p	Radius of the nanoparticle (nm)
R	Gas constant ($8.3145\mathrm{J \cdot mol^{-1} \cdot K^{-1}}$)
R_m	Gas constant in effective mass units ($8.3145 \times 10^7 \mathrm{g \cdot cm^2 \cdot mol^{-1} \cdot K^{-1} s^{-2}}$)
R_p	Gas constant in effective pressure units ($83.145\mathrm{bar \cdot cm^3 \cdot mol^{-1} \cdot K^{-1}}$)
S_{bb}	Measured signal from a black body ($\mathrm{J \cdot cm^{-2}}$)
S_{LII}	Calculated LII signal ($\mathrm{J \cdot cm^{-2}}$)
S_p	Measured LII signal intensity ($\mathrm{J \cdot cm^{-2}}$)
t	Time (s)
Δt	Tiny period of time (s)
T_{bb}	Particle temperature of black body (K)
T_g	Temperature of the surrounding gas (K)
T_p	Particle temperature (K)
T_{ref}	Reference temperature used in Clausius–Clapeyron equation (K)
U_{int}	Internal energy for a single spherical particle (J)
V_{tube}	Volume of the quartz tube (L)
W_V	Average molecular weight of sublimed carbon species ($\mathrm{g \cdot mol^{-1}}$)

Y_i	Corresponding result in Taguchi method
α_T	Thermal accommodation coefficient
α_M	Mass accommodation coefficient of vaporized carbon clusters
γ	Heat capacity ratio of the gas
ε	Emission coefficient of nanoparticle
λ	Laser wavelength (nm)
λ_{det}	Detection wavelength (nm)
λ_{flitre}	Effective band for filter (nm)
λ_w	Effective band for laser (nm)
ρ_p	Density of the nanoparticle ($\mathrm{g \cdot cm^{-3}}$)
σ	Stefan-Boltzmann constant ($5.6704 \times 10^{-12} \mathrm{W \cdot cm^{-2} \cdot K^{-4}}$)

Résumé en français

Titre: Étude de la formation et de l'activité catalytique de nanoparticules durant les premiers instants de la croissance de nanotubes de carbone par dépôt chimique en phase vapeur assisté par aérosol

Mot clés : Nanotube de carbone ; Catalytique ; Nanoparticules ; Dépôt chimique en phase vapeur ; in-situ diagnostic ; Laser-induced incandescence

Résumé :

De par leurs propriétés remarquables, les nanotubes de carbone (NTCs) reçoivent beaucoup d’attention et de nombreuses recherches sont menées sur ces matériaux depuis les dernières décennies. Le nombre d'applications envisagées mais aussi la quantité demandée de NTCs augmentent chaque année. Pour atteindre une production à grande échelle et contrôlée, il est nécessaire d'avoir une bonne compréhension des mécanismes de croissance des NTCs. Dans ce manuscrit, la formation de nanoparticules (NPs) par dépôt chimique en phase vapeur assisté par aérosol (CVD) sont étudiées expérimentalement, pour analyser le processus d'évolution des NPs et leur relation avec les NTCs.

Dans le chapitre 1, nous présentons une introduction générale sur des structures, les méthodes de synthèse, les propriétés et les applications envisagées des NTCs, ainsi que l’état de l’art concernant l’étude des mécanismes de croissance des NTCs.

Dans le chapitre 2, nous décrivons le système de dépôt chimique en phase vapeur avec catalyseur flottant, ainsi que les méthodes de diagnostic in-situ/ex-situ utilisées dans cette étude. La technique d’incandescence induite par laser (LII) est particulièrement importante dans ce chapitre, car cette technique nous permet de réaliser un diagnostic in situ sur la quantité/taille des NPs déposées pendant le processus de synthèse.

Dans le chapitre 3, nous présentons l'évolution des NPs lors de la synthèse ainsi que les influences des différents paramètres de CVD (température, quantité de carbone/catalyseur, composition du gaz, etc.) sur les gouttelettes et les NPs respectivement. Un modèle pour la formation de NPs est proposé à la fin de ce chapitre.

Dans le chapitre 4, les résultats des expériences sur l'évolution de la composition du gaz sont révélés. Ces résultats donnent des informations concernant les réactions chimiques ayant lieu dans la phase gazeuse lors de la synthèse des NTCs.

Dans le chapitre 5, une étude détaillée de l'influence des paramètres de CVD sur les produits NTCs est menée, et les relations entre les NPs et les NTC sont discutées.

Pour finir, des conclusions générales ainsi que les perspectives prévues pour les travaux futurs sont présentées.

General introduction

Title: Study on the formation and catalytic activity of nanoparticles in early stages of carbon nanotubes growth under aerosol-assisted chemical vapor deposition

Keywords: Carbon nanotube; Catalytic; Nanoparticles; Chemical vapor deposition; in-situ diagnostic; Laser-induced incandescence

Abstract:

Due to the outstanding properties in various aspects, carbon nanotubes (CNTs) received worldwide attentions and intensive investigations are carried out in the last decades. While the number of applications as well as the quantity demanded of CNTs are increasing year after year, to achieve large scale production of the desired structures in a controlled way, it is highly required having a clear understanding about the CNTs growth mechanism. In this study, the formation of nanoparticles (NPs) under aerosol-assisted chemical vapor deposition (CVD) is experimentally investigated, aiming to study the NPs evolution process and their relation with the CNTs products.

In chapter 1, we provide a general review of CNTs structures, synthesis methods, properties as well as applications. Moreover, the current situation of CNTs growth mechanism study is presented.

In chapter 2, the floating catalyst chemical vapor deposition synthesis system, and the in-situ/ex-situ diagnostic methods used in this study are introduced. Laser induced incandescence technique (LII) is particularly explained in this chapter, which permits to achieve an in-situ diagnostic of the NPs quantity/size during the synthesis process.

In chapter 3, the evolution of NPs during the synthesis is presented, in which the influences of different CVD parameters (temperature, carbon/catalyst quantity, gas composition etc.) on the droplets as well as on the NPs are investigated respectively.

A NPs formation model is proposed based on the NPs variation information at the end of this chapter.

In chapter 4, the experimental results of the gas composition evolution in chemical vapor deposition reactor are revealed, which reflect the gas phase chemical reactions information during the CNTs synthesis.

In chapter 5, a detailed investigation about the influence of CVD parameters on the CNTs products is explained. And the relation between the NPs and CNTs is discussed.

In the end, general conclusions are formed according to works and perspectives are provided for the improvement of the future work.

ChapterⅠ Carbon nanotubes and their applications

1.1 Background

Our universe contains many species of atoms, according to their number of protons in their atomic nuclei, these atoms have been identified each having a chemical element name. In the elements, carbon is the fourth most abundant element (0.5%) in the universe by mass after hydrogen (75%), helium (23%) and oxygen (1%), and the 15th most abundant element in the earth's crust (0.03%). It has a very close relation with human, since the human body contains 18% carbon that exists in DNA, proteins, fats, and carbohydrates etc., and carbon in its miscellaneous forms like charcoal, graphite, carbon black, coal etc. has already been used in art and technology since prehistoric times [1-4].

The carbon's ability to subtly bind with a wide range of elements to form complex materials is due to its specific arrangement of the electrons around the nucleus of atom[5]. As it has six electrons sharing 1s, 2s and 2p orbital, its original electronic structure is $1s^2 2s^2 2p^2$, however, since the 2p atomic orbitals can hold six electrons, the electrons at 2s could be promoted to 2p to form covalent bonds, and result in multiple orbital hybridizations. In these orbital hybridizations, sp^1, sp^2 and sp^3 are formed respectively depending on how many p orbitals are involved. According to the orbital hybridizations type, carbon binds different bonds σ and π while forming a molecule: two σ bonds and two π bonds are formed by sp^1 hybridized carbon atom, while three σ bonds and one π bond for sp^2, and four σ bonds for sp^3. The orbital geometry changes also with the hybridization type, for sp^1, sp^2 and sp^3, as the geometries are linear (two orbitals separated by 180°), plane (three orbitals separated by 180°) and tetrahedral (four orbitals separated by 109.5°) respectively. As the hybridization type determines the final molecules nature and properties, influenced by the orbital hybridization differences, even pure carbon can form different structures, known as the allotropes of carbon. According to the study of Bundy, F., et al., the transformation between these carbon allotropes could be achieved under certain pressure/ temperature with the relating catalyst[6], as shown in Fig.1-1.

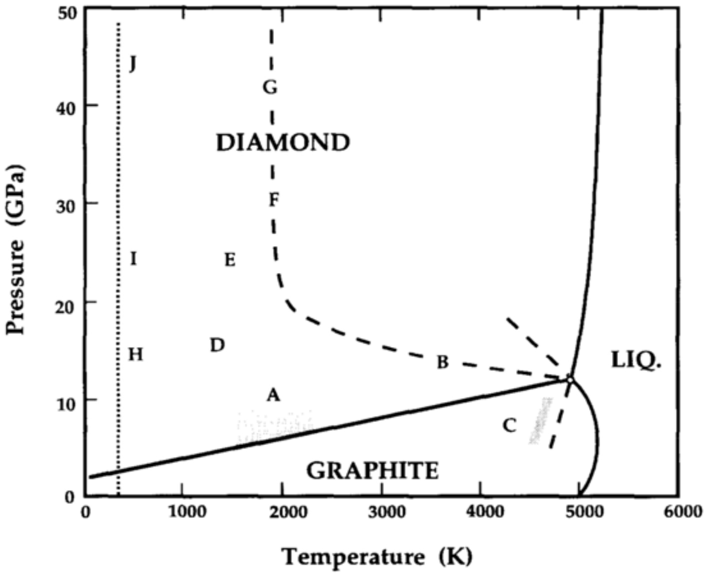

Fig. 1-1 *Temperature-pressure dependent phase diagram for carbon, in which the letters from A to J signify different processes or threshold to achieve the transformation, for detailed information, see reference [6]*

Among these allotropes mentioned above, graphite and diamond are relatively stable and have regular structures, comparing to the carbon allotropes like carbon black, soot, coke etc. in which carbon is arranged in an amorphous way. For graphite, it is the sp^2 orbital hybridization that determines its structure, so the geometry for the carbon arrangement is plane, in which each carbon atom strongly connects to three nearest other carbon atoms by σ and π bonds in a plane. This connection between the atoms determines a hexagonal network for carbon, known as graphene sheet, while weak Van der Waals (VdW) forces contributes to the parallel stack of these sheets to form the graphite, with the distance between two neighbor graphene layers ~0.334nm. For diamond, the carbon atoms in this material are connected with σ bonds by the sp^3 orbital hybridization, each carbon atom is at the center of a rigid tetrahedral network that is constructed by its nearest four carbon atoms, and the distance between the these carbon atoms is always a constant (~0.154nm). Rather that the two-dimensional structure of graphene sheet, the diamond owns a three dimensional structure. If compared, the diamond is less stable that graphite, and can be converted to graphite at 1700°C under normal pressures[7]. Due to their structure differences, graphite and diamond have their own special properties and applications. For example, graphite is soft but has good electrical conductivity, while diamond is known as one of the hardest materials and owning extraordinary optical characteristics. The schematic of the graphite and diamond structures are shown in Fig. 1-2 below.

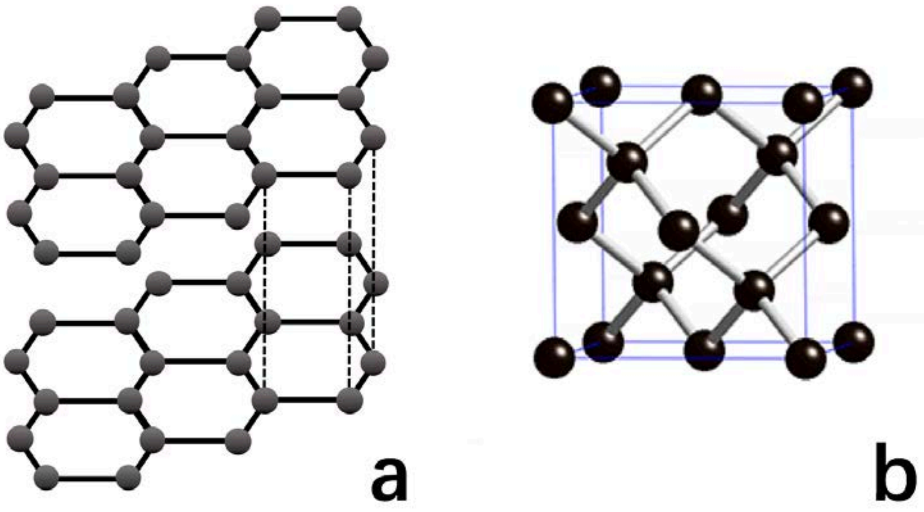

Fig. 1-2 *Schematic of the graphite (a) and diamond (b) structures*

In addition to the graphite and diamond, there are also other carbon allotropes which owning a regular atom arrangement structure, for example the fullerenes. For this kind of carbon allotropes, they are closed-cage carbon molecules in the form of a hollow sphere, ellipsoid, tube and many other shapes. In the year 1985, the first fullerene buckminsterfullerene (C_{60}) was firstly discovered during the experiments in which graphite was vaporized by a Nd:YAG laser[8]. It was found containing 60 carbon atoms and forming a soccer ball like structure with twelve pentagonal rings and twenty hexagonal rings (shown in Fig. 1-3). Even the C_{60} has a structure of unique stability and symmetry, its low production quantity limited the study progress on this kind of carbon allotropes at that time. Eventually, after years of hard work, in the year 1990, bulk production for fullerenes has been finally achieved using a much simpler method[9]. From then on, numerous studies have been carried to investigate the fullerenes physical and chemical properties, and a series of fullerene derivatives have been synthesized.

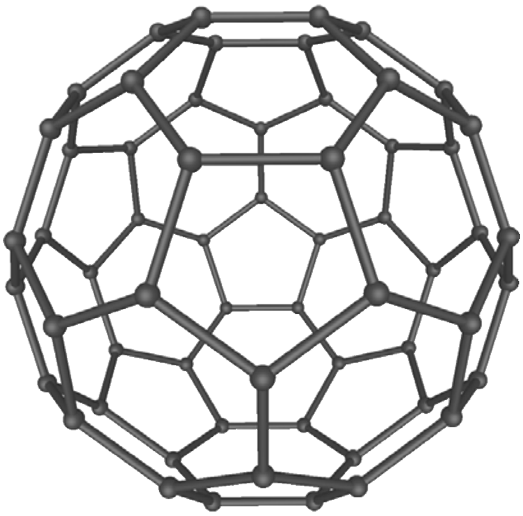

Fig. 1-3 *Molecular structure of buckminsterfullerene (C_{60})*

Carbon nanotubes (CNTs) are perhaps one of the most important results of the studies on the fullerene. Inspired by previous work on fullerene, an electron microscopist Sumio Iijima paid his attention on the depositions that were formed on the graphite cathode after arc-evaporation. In these depositions, many new graphitic structures were found, including very special long hollow graphitic carbon nano-tubules. He published his founding in the year 1991, which prompted fullerene scientists to look into this new structure of fullerene[10]. Fig. 1-4 shows the microtubules of graphitic carbon photos that were reported by Iijima in his paper, in which the graphitic sheet number differs.

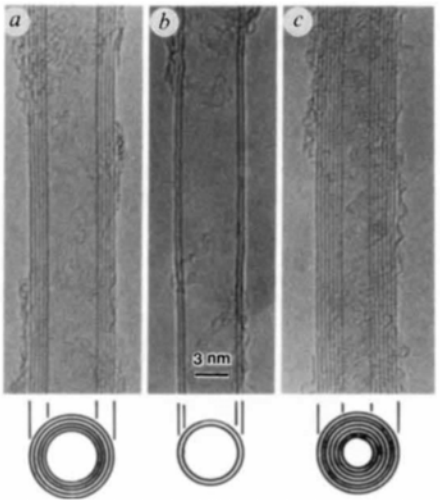

Fig. 1-4 *TEM observations of graphitic carbon microtubules reported by Iijima*[10]

In fact, Iijima is not the first person that discovers this kind of structure. Before him there are already several reports that have been published mentioning the carbon nanotubes structure[11-13], however none of these reports have drawn such great attention as the Iijima's paper did. As the carbon products presented by Iijima in 1991 usually have multi concentric graphene sheets wrapped as nano cylinder, they are named as multi-walled carbon nanotubes (MWNTs). Two years later, the synthesis of single-walled nanotubes (SWNTs) was reported separately by Iijima and Toshinari Ichihashi of NEC[14], and Donald Bethune and colleagues of the IBM Almaden Research Center[15]. From then on, there are more and more studies that have been made over the world to investigate the properties, synthesis as well as applications of the nanotubes, especially after the year 2000 (see Fig. 1-5[7]).

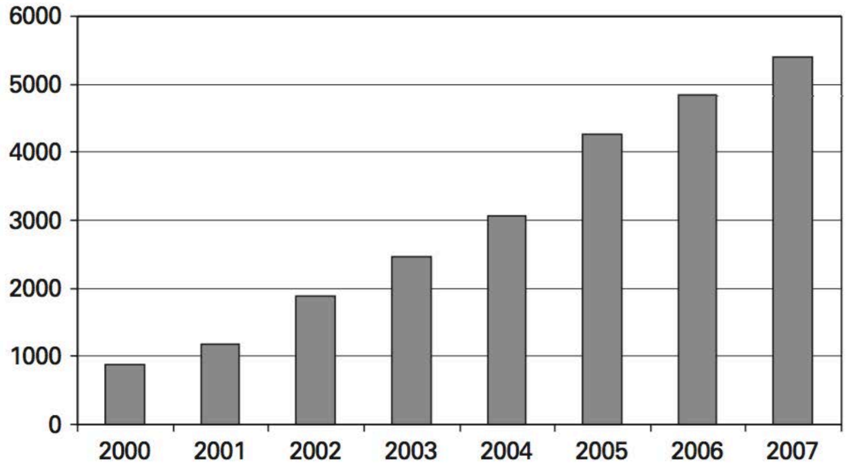

Fig. 1-5 *Papers number on carbon nanotubes published annually from 2000 to 2007*[7]

1.2 Carbon nanotubes structures

For the mentioned carbon allotropes structures, they could be divided according to their dimensions, for example, the diamond and graphite have three-dimensional structures, the graphene has two-dimensional structure etc. For CNT, as its length-to-diameter aspect ratio could be as much as 28,000,000:1 in some cases[16], it is a good example as the one dimensional material. However, only the dimensional description is not sufficient. As has been mentioned in the former section, CNTs could be seen as nano cylinder formed by wrapping graphene sheets, CNTs could be classified as SWNTs and MWNTs according to their graphene sheets numbers. For the SWNT, generally its diameter is 0.5~5nm, and its length varies from micrometers to centimeters[16]. For MWNT, as it has multi concentric cylinders of wrapping graphene sheets, its diameter size may arise from several to hundred nanometers. The distance between the neighboring sheets in MWNTs is ~3.4Å, which is much close to interval 3.35Å in graphite.

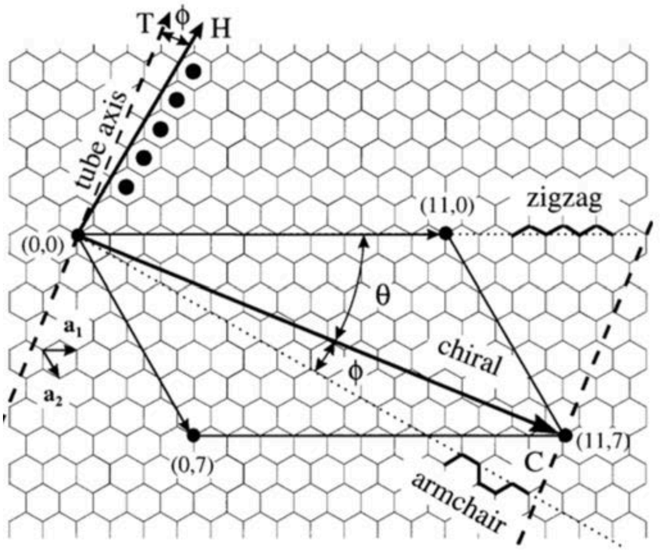

Fig. 1-6 *Various CNT configurations as a function of the Hamada indices (n, m)*[17]

Besides the graphene number difference, the CNTs could also be classified according to their corresponding graphene sheet rolling up direction. A vector $\overline{C}$ named chiral vector is taken use of here to specify this difference. It is normal to the tube axis $\overline{T}$, and is defined by the Hamada indices (*n, m*) and two basis vectors $\overline{a_1}$ and $\overline{a_2}$ of the graphene network lattice. The equation for $\overline{C}$ is shown below:

$$\overline{C} = n\overline{a_1} + m\overline{a_2}$$

For this chiral vector, its length L_C has a direction relation with the tube diameter d, as

$$d = \frac{L_C}{\pi} = \frac{\sqrt{n^2 + m^2 + nm}}{\pi} a$$

in which a is the length of unit vector 2.46 Å. To describe the graphene rolling up direction, the chiral angle is used, which is defined either with respect to the zigzag axis (*θ*) or to the armchair axis (*φ*=30-*θ*), it has the relation as below

$$\tan\theta = \frac{\sqrt{3}m}{2n+m}, (0 \le |\theta| \le 30^\circ)$$

According to these definitions, the Hamada indices (*n, m*) could be used to specify the unique nanotube diameter and the chiral angle, even there are infinite possibilities for carbon nanotube structures. For example, the n=1, m=0 ($\theta = 0^\circ$) is for the zigzag CNTs, the n=1, m=1 ($\theta = 30^\circ$) is for the armchair CNTs and the cases where $0^\circ < \theta < 30^\circ$ are for the chiral CNTs. All the mentioned vectors are presented in Fig. 1-6.

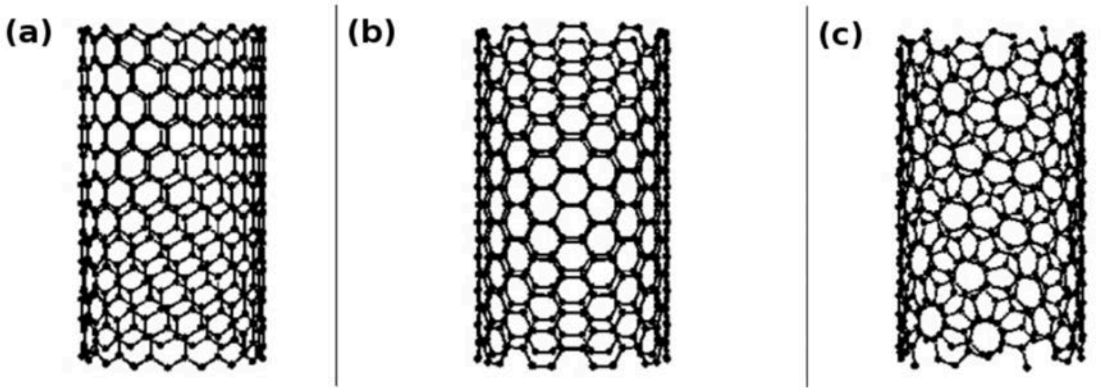

Fig. 1-7 *Examples of zigzag (a), armchair (b) and chiral (c) carbon nanotubes[18]*

1.3 Carbon nanotubes synthesis routes

1.3.1 Arc-evaporation

As has been mentioned in section 1.1, both the highly perfect multi wall tubes produced by Iijima in 1991[10] and the first single wall nanotubes achieved in 1993 [14, 15] involves the same CNTs synthesis technique arc-evaporation, it suggests that this arc-evaporation method has play a very important role for the CNTs synthesis. An example for typical arc-evaporation equipment is shown below in Fig. 1-8. This equipment involves several components. Firstly it's the gas flow system, it includes He inlet and a diffusion pump, by which a controlled continuous flow of He could be achieved to create a static gas atmosphere for the CNTs synthesis. Secondly, it's a pair of electrodes, in which both cathode and anode are usually composed of high purity graphite, and the positions of the electrodes should be paid attention to ensure that there is always a gap between them. To start the CNTs synthesis, a stable voltage is applied (~20V), and the anode is pushed gradually towards to the cathode until the arcing occurs. Then the anode position will be maintained (usually the distance between the rods is ~1mm) for the stable arc, and the rod will be consumed for the CNTs synthesis (usually it's the rod on anode which will be consumed, and creates the product deposition on the cathode).

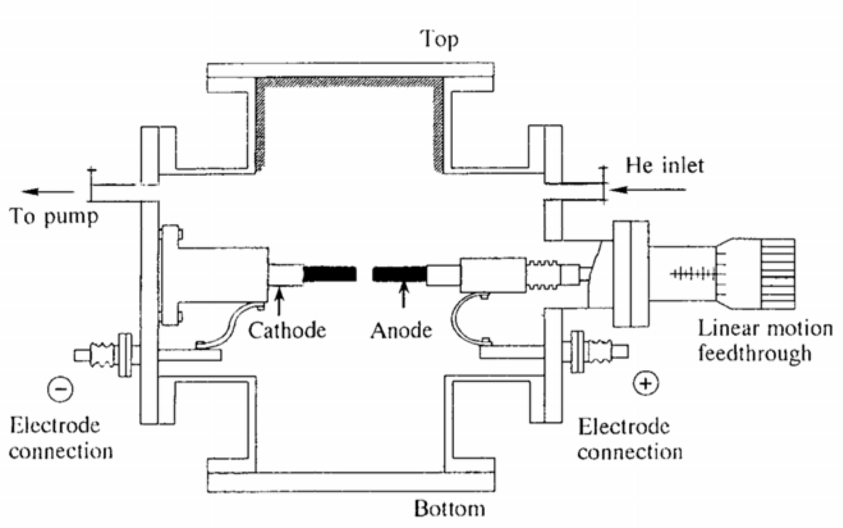

Fig. 1-8 *Schematic of the CNTs growth by arc-evaporation method[19]*

For the arc-evaporation method, there are several critical factors during the synthesis process that have considerable influences for the CNTs product quality. According to the study of Ebbesen and Ajayan[20], CNTs production could be highly promoted at an optimum pressure, either too high or too low pressure disfavor a high quality bulk production. The direct current induced by the applied voltage is also very important and should be kept as low as possible, as when the current intensity is too high, it will result in hard, sintered material in which quite few nanotubes could be found[21, 22].

Based on the general principle shown in Fig. 1-8, there are various modifications that have been made. For example, there are many studies suggesting that He could be replaced by other gas, including H_2[23, 24], N_2[25], CF_4[26] , organic vapors[27] etc., and arc-discharge was proved could work under water or in solution[28-32]. What's more, the electrodes materials have also been developed, the synthesis using coal instead of graphite as the electrode material produced successfully the CNTs[33, 34]. All these studies have expanded the applicability of the arc-evaporation method, and contribute a better control for the production quality.

1.3.2 Laser ablation

In the year 1995, Smalley and his colleagues firstly demonstrated the CNTs synthesis by laser ablation[35]. The principles and mechanisms of this method are quite similar to the arc-evaporation method. A typical laser ablation CNTs synthesis is carried out in a high temperature furnace under a flow of inert gas (typically argon) at controlled pressure, in which the carbon source (graphite) target doped with a small amount of metal catalyst will be vaporized with the help of laser pulse to achieve the CNTs production, as illustrated in Fig. 1-9[36].

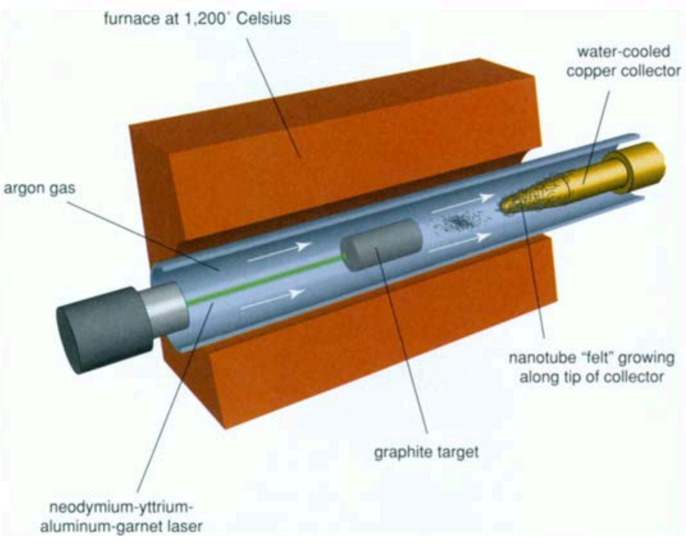

Fig. 1-9 *Schematic of the CNT growth by laser ablation*

For this CNTs synthesis process, many studies have been developed trying to augment its production yield. According to the study of Thess et al[37], a double laser pulse is favorable in this case, as it can promote the target evaporation, thus highly increase the CNTs production yield. The use of CO_2 laser is also reported, in which SWNTs were found produced even at room temperature[38]. Nowadays, laser ablation is usually known as one of the superior methods to grow high quality/purity SWNTs.

1.3.3 Chemical vapor deposition

Besides the arc-evaporation and laser ablation methods that have been mentioned above, the chemical vapor deposition (CVD) method is also commonly used owing to its high yield[39-41], relatively low technical needs[42] and easy control of the reaction parameters[43]. For a typical CVD synthesis process, carbon sources are firstly introduced into a temperature-control (usually ranging from 600 to 900°C for MWNTs, and from 900 to 1200°C for SWNTs[44]) system by carrier gas. Then their catalytic/pyrolytic decomposition process occurs, by which the reactive carbonaceous species are released. And finally these reactive species will contribute to the CNTs growth assisted by the catalytic action. An example for CVD synthesis process is shown in Fig. 1-10. Besides the horizontal furnace depicted in this figure, there are also other forms like fluidized bed reactor, vertical furnace and basic plasma enhanced CVD etc.[45].

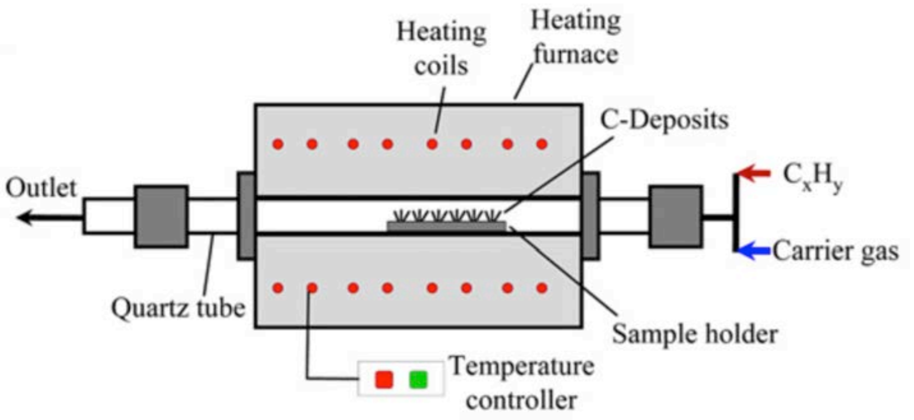

Fig. 1-10 Schematic of the CNTs growth by chemical vapor deposition[46]

For the CVD synthesis of CNTs, there are various carbon sources from gaseous state (methane, acetylene, ethylene, etc.) to liquid state (ethanol, benzene, toluene, xylene, etc.) that can be chosen according to different experimental conditions[41, 47-55]. Catalyst is another critical factor during CVD synthesis. Transition metals like Fe, Co, Ni are usually taken as catalysts [48, 52, 54] because of their relatively high carbon solubility and the high carbon diffusion rate in these metals[56]. For these catalysts, they can be not only in situ produced by the decomposition process of organometallics during the synthesis, but also pre-treated before the introduction of carbon feedstock[57]. To introduce carbon/catalyst sources into CVD system, argon and nitrogen are widely used as the carrier gas[57-59]. In many research, certain amount of hydrogen is also added to assist the CNTs synthesis simultaneously. It is commonly believed that the hydrogen contributes to morphologies and properties control of CNTs, which helps to prevent catalyst deactivation and carbon impurities formation [60-64]. Besides the factors mentioned above, there are also parameters like temperature[40], substrate[57], and other gas composition[65] that can influence the properties of the final products. As there are so many factors involved during the CVD synthesis process, a thorough understanding of the CNT growth mechanism is therefore needed for a better control of the CNTs quantity/quality.

1.3.4 Other methods

There are also other CNTs synthesis methods that are less commonly used, such as heat treatment, flame pyrolysis, electrolysis, solar method etc. For heat treatment method, it originates from the high-temperature heat treatments study on fullerene, in which a small amount of short MWNTs was occasionally found in the heat-treated soot[66]. Based on this phenomenon, a solid phase MWNTs growth model was proposed and further studies were made. It was found that by annealing the fullerene soot made by arc evaporation under certain conditions, the MWNTs of several microns meters length could be obtained in the presence of amorphous boron[67]. With the development of the research, more and more materials like sucrose carbon and carbon black have been proved being able to act as the carbon sources precursor for this CNTs synthesis process[68-70]. Even in synthetic graphite samples made by high-temperature heat treatment from solid precursors the MWNTs were found[71], like shown in Fig. 1-11

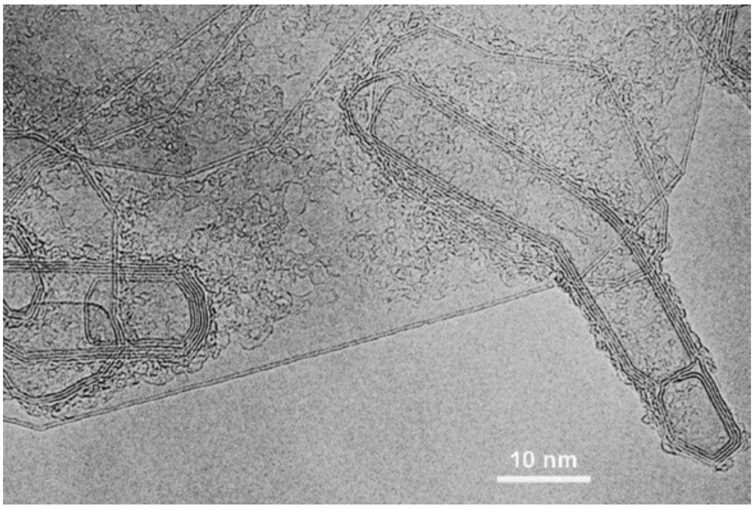

Fig. 1-11 *MWNTs and nanoparticles found on graphite sample*[71]

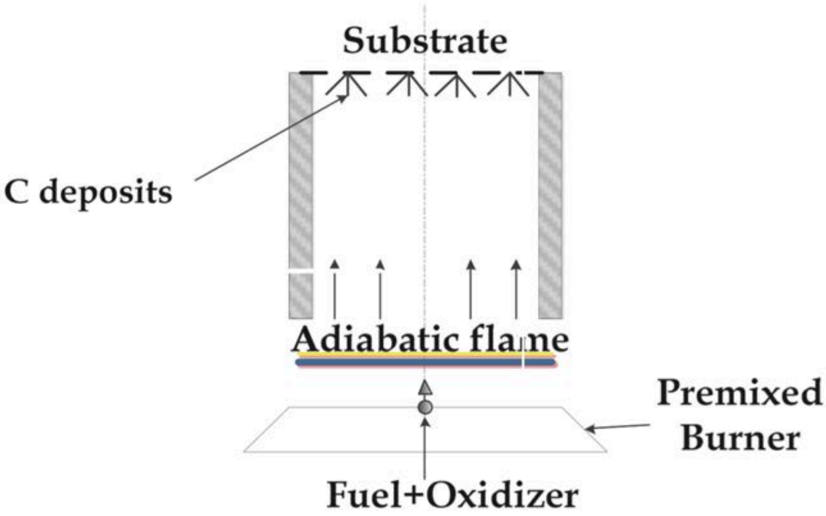

Fig. 1-12 *Schematic of the CNTs growth by flame pyrolysis[72]*

Flame pyrolysis is another CNTs synthesis method that is studied by several groups [73-76]. Its general synthesis process is depicted in Fig. 1-12, in which fuel and oxidizer are premixed firstly then react in a flame, resulting in elevated temperature and gaseous mixture that contribute for the following CNTs growth. Catalysts are also involved in the synthesis, they are either located at the deposition substrate or as aerosol particles. Except the premixed type (fuel and oxidizer mixed before burning) shown in the Fig. 1-13, there are also other flame types like non-premixed (fuel issued from inner tube while the oxidizer from outer tube) and partially premixed. Besides the flame type, the choice of carbon sources/catalyst also has important influence on the CNTs production. Methane, ethylene, and acetylene are usually used as carbon sources, while the transition metals like iron, nickel and cobalt as well as alloys of transition with other metals like chromium, copper and zinc etc. are used as catalysts. Sometimes diluents are also applied in the flame pyrolysis, in which nitrogen and argon are the mostly used gases[72].

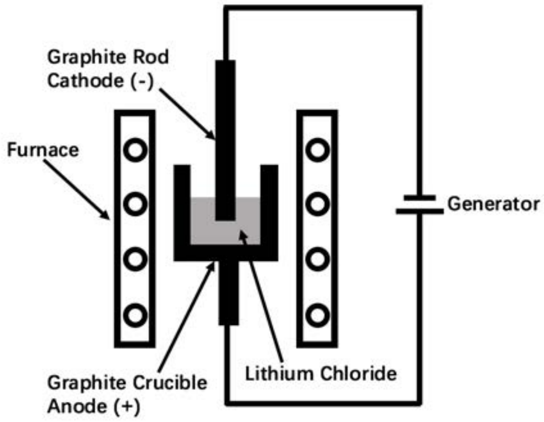

Fig. 1-13 *Schematic of the CNTs growth by electrolysis[77]*

Electrolysis method for CNTs synthesis is based on previous study about the electrochemical synthesis of fullerene-related carbon nanomaterials[77, 78]. As shown in Fig. 1-13, by the molten ionic salts (~ 600°C LiCl in this figure), the graphite crucible anode is indirectly connected with the graphite rod cathode. Then a current is supplied, which promotes the electrolysis synthesis of carbonaceous material at the cathode. After the synthesis process, the apparatus is cooled down to room temperature, and the nanomaterial products contained in the crucible will be extracted. The product components are very complex, which consist of CNTs, encapsulated metal particles, amorphous carbon, carbon filaments and various intermediate structures. To increase the CNTs yield and control other components quantities, further studies on this low cost electrolysis synthesis method are highly required.

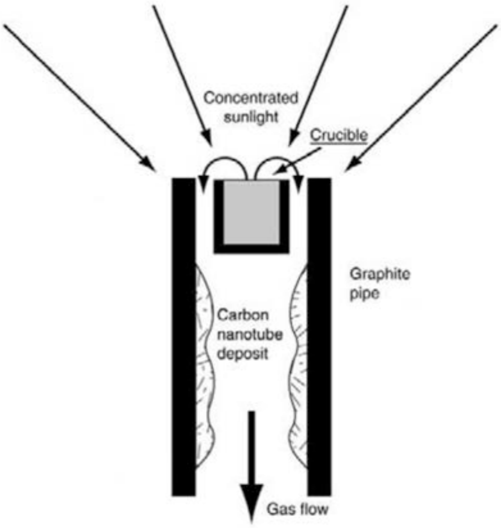

Fig. 1-14 *Schematic of the CNT growth in the solar reactor*[79]

Solar reactor can be used for CNTs synthesis also. Its critical component is shown in Fig. 1-14[79], which is composed of a graphite crucible surrounded by a graphite pipe. To begin the CNTs synthesis, the crucible filled with a graphite/catalyst mixture will be exposed to concentrated sunlight, resulting in carbon vaporization. With the protection of inert gas atmosphere, this vaporization will be brought to the low temperature zone by the gas flow, and deposit on the graphite pipe wall. A cellulose filter is connected to the pipe, which is for the soot collection. For the product synthesis by this method, it generally composed of CNTs, encapsulated catalyst particles, empty carbon vesicles as well as amorphous carbon. By changing the synthesis parameters like catalyst type, pressure, temperature and gas flow, the product properties as well as yield could be varied.

1.4 Carbon nanotubes properties and applications

In the previous sections the very special CNTs structures have been discussed. As the materials properties are highly depend on their structures, it is reasonable to conclude that the CNTs have some extraordinary characteristics. In this section, the CNTs properties on different aspects and their relating applications will be presented, which explains why in recent years the CNTs have attracted so much attention over the world.

1.4.1 Carbon nanotubes properties

1.4.1.1 Electronic properties

As CNTs could be considered as rolled up graphene sheets that form seamless concentric nanocylinders. It is reasonable to suspect that the nanotube's chiral angle as well as its diameter may influence its electronic properties. For the chirality property, according to the study of Dresselhaus et al[80-82], in SWNTs the metallic conduction occurs when the equation below is satisfied:

$$n-m=3q$$

in which the n and m are the Hamada indices that have already been discussed in section 1.2. Based on this fact, it could be concluded that all armchair SWNTs should be metallic, while one-third of zigzag and chiral SWNTs are semiconducting. For the atomic dimensional diameter, as graphene rolling up process leads to curvature for the SWNTs structure, it is supposed that the sp^3 orbital hybridization character will be brought into the bonding, especially for the cases where the diameter is quite small. To study the possible influence of this curvature, much work has been done[83, 84].

According to the results of these studies, it has been found that the influence also depends on the tube chirality, for armchair tubes, the effect of curvature doesn't lead to any obvious changes for their electronic property, these tubes are still metallic. However, for non-armchair tubes, the curvature leads to open up a gap, and its magnitude is proportional to $1/d^2$ (d is the nanotube diameter). This gap is negligible when the diameters are larger than 20nm, but could achieve even 10meV for the small diameter nanotubes. For metallic SWNT, as ballistic electrons transport could be achieved in this material, it is quite near to be an ideal one-dimensional quantum wire which could be used for carrying large current without energy dissipation[85]. However, for the semiconducting SWNTs, the electrons transport is diffusive rather than ballistic, the energy dissipation is no more negligible[86].

As MWNTs consist of multi rolled up graphene sheets, their electronic property is more complex than that of the SWNTs. The first experimental measurements on individual MWNTs were made in 1996, it was found the MWNTs resistance rose with the decrease of temperature, suggesting that the sample MWNTs are semiconducting[87]. Later another test was made using a four-probe resistance measurement on eight different nanotubes[88], the results varied from $0.051\mu\Omega$m to 8mΩm. As the electrical resistivity of semiconductor is between 1mΩ·cm～1GΩ·cm at room temperature, it suggests that MWNTs can express a range of electronic behavior that both metallic and semiconducting properties could be achieved according to their structures. The four-probe technique has also been used to measure the metallic SWNTs ropes resistivity, which is in the order of $10^{-4}\Omega\cdot$cm at 300K, being noted as the most highly conductive carbon fibers known[37]. As the CNTs have such good conductivity, their electronic transport limit was studied[89]. It was found that contrary to the metal wires case where the electrical breakdown occurs in a continuous current, for the MWNTs, they usually fail with a series of sharp current steps, which suggests that the electrical breakdown is due to the destruction of individual nanotube shells in a succession. In addition, superconductivity studies using pure CNTs or SWNT ropes have been reported by several groups[90-93], which suggest a new direction for CNTs electronic properties research.

1.4.1.2 Mechanical properties

CNTs are expected to have special mechanical properties because of their strong sp^2 bonds between the atoms and their very special tubular structure, thus many studies have carried out in this field. In the year 1997[94], Jian Ping Lu investigated the elastic properties of CNTs using an empirical force-constant model. According to his results, he declared that the elastic properties are not sensitive to the CNTs structure like diameter or chirality, and the Young's modulus is ~1TPa for the CNTs, which is comparable to that of diamond. One year later[95], using a nonorthogonal tight-binding scheme, E. Hernández et al. studied the elastic properties of C and $B_xC_yN_z$ composition nanotubes, they found the Young's modulus for CNTs is from 1.22 to 1.25TPa varying with the structure difference, based on their results, the independence of CNTs elastic properties was proved again. However, in the following studies, this independent behavior has been proved wrong[96-100], where the Young's modulus has a big range (from 0.5 to 5.5TPa), and the stiffness has a decrease tendency for smaller CNTs diameters. For the CNTs fracture process, the maximum tensile strain has been determined at 0.2~0.256, if exceeded, the bond between the carbon atoms will be broken[101-103].

During the study process of CNTs mechanical properties, various techniques like AFM, TEM and SEM have been applied in experiments, which contribute to a better understanding about CNTs mechanical behavior. Fig. 1-15 shows a bent MWNT (made by arc-evaporation) with ~400nm radius of curvature[104], it could be found that for this MWNT, there are regularly arranged bucks occur, and no broken layers are observed. In fact, if the constraining stress is released, the bent MWNTs can even return to its original form[105]. This phenomenon suggests excellent MWNTs resilience as well as outstanding flexibility for the graphene sheets within, which indicates the possibility to increase the material deformation recovery by adding MWNTs. This diagnostic has also been done by other groups on different CNTs like aligned MWNTs[106] and SWNTs[107], similar behaviors were observed.

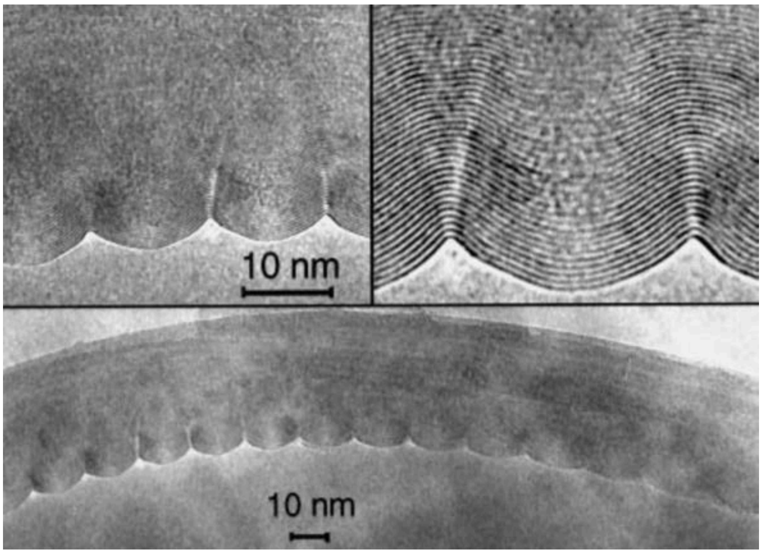

Fig. 1-15 *TEM image for a bent CNT with ~400nm radius of curvature*[104]

Besides the qualitative diagnostic that is mentioned above, the quantitative measurement of CNTs mechanical properties assisted by TEM was carried out firstly in 1996[108], however, by analyzing the temperature dependent results, it was found that for the MWNTs samples, their Young's modulus vary from 0.41TPa to 4.15TPa, and its average value is 1.8TPa, there exist great uncertainties for the results. After this attempt, there are more and more quantitative measurements carried out, using AFM, TEM as well as SEM[105, 109-115], their results indicate that the MWNTs have exceptional stiffness and strength, with the Young's modules 0.81~1.28TPa, and the tensile strength 11~150GPa, the variation for these values is mainly induced by the defect on the MWNTs. SWNTs mechanical properties were also tested, suggesting that the Young's modulus is 1~1.25TPa, and the tensile stress is 13~52GPa[116-118].

In summary, despite of the results diversity shown in different literatures, the

CNTs have revealed extraordinary mechanical properties that are much better than steel (for stainless steel, its Young's modulus is ~0.2TPa, its tensile strength 0.65~3GPa). These properties, coupled with their low density, make the CNTs a very promising material in a whole range of structural applications.

1.4.1.3 Thermal properties

Since the carbon allotropes diamond and graphite have good thermal properties, especially relatively high thermal conductivity[119], many studies have been carried out on the CNTs thermal behavior. According to the measurement results, it indicates linear specific heat and thermal conductivity above 1 K and below room temperature, while a $T^{0.62}$ behavior of the specific heat below 1 K[120].

Under room temperature, the thermal conductivity differs with the CNTs structures, which is about 3500$Wm^{-1}K^{-1}$ for a metallic SWNT, more than 3500 $Wm^{-1}K^{-1}$ for arc-evaporation made MWNTs, and only 200 $Wm^{-1}K^{-1}$ for catalytic CVD produced MWNTs respectively [121-123]. The difference between the latter two suggests that the CVD synthesis process has introduced more thermally opaque defects on CNTs, which impede the phonons diffusion. Comparing these results with the thermal conductivity of copper, which is ～398 $Wm^{-1}K^{-1}$ at room temperature, the well synthesized CNTs have been proved a much better thermal conductor in the property aspect.

1.4.2 Potential and current applications

In the previous section 1.4.1, the amazing CNTs properties have been presented. These properties have made the CNTs one of the most popular scientific topics over the world, and stimulated people's enthusiasm for exploring CNTs applications in various aspects, such as electronic device, energy storage, probe/sensor, nanotube composite, hydrogen storage media, bio-engineering, radar absorption, water treatment etc. In this section, several major applications will be introduced, which reveals how CNTs have influenced our world.

1.4.2.1 Electronic devices

CNTs electronic properties have been discussed in section 1.4.1.1, based on these properties, many studies have been conducted to explore the nanoelectronic devices. According to previous studies about the elbow connection[124, 125], Cees Dekker and his colleagues have experimentally proved that a kinked nanotube connecting between a metallic and a semiconducting materials will form a nanoscale diode, in which the current can only pass in one direction[126]. The nanotube diodes could also be produced by other methods[127, 128]. For example, it can be obtained by half doping a semiconducting SWNT with K, in this case the doped half and the no doped half of the SWNT will act as the n and p type semiconductors respectively, and form a SWNT p-n junction diode.

CNTs are also involved for the field effect transistor (FET) production, in which the traditional channel material Si is replaced by an individual semiconducting SWNT. This kind of carbon nanotube FET was firstly produced in 1998[129]. Then many studies about this topic have been done, in which various fabrication methods, application as well as properties influential factors were discussed[130-133].

Besides the nanoscale diode and CNTs FET, nanotube field emitter is another CNTs electronic application. Many field emission experiments have been conducted on individual tubes, tubes clusters as well as CNTs array since 1995[134, 135]. Compared to the traditional materials, CNTs provide the advantages like stable emission, adequate luminance and long lifetimes for field emission[136]. Using the CNTs field emission technique, some display prototypes have been produced, as shown in Fig. 1-16.

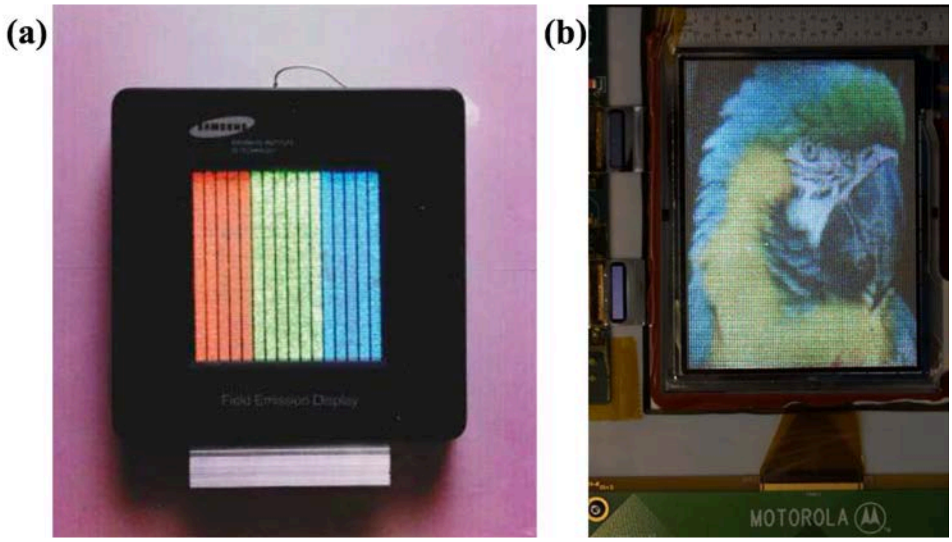

Fig. 1-16 *(a) Samsung 4.5 inch SWNT flat panel display at color mode with red, green, and blue phosphor columns*[137] *(b) Motorola lab 4.6 inch-diagonal NED (0.726-mm pixel) showing a color video image of a parrot*[138]

1.4.2.2 Energy storage

The energy storage is another application aspect based on CNTs electronic properties, CNTs are often used as the electrode materials or the conductive filler for the active materials in the energy storages systems, which include Li-ion batteries, supercapacitors, fuel/solar cells as well as actuators etc.[139]

In Li-ion batteries, energy store/release processes are achieved by lithium ions transfer between the anode and cathode electrodes. CNTs can serve directly as anode material in the batteries, as they are capable to absorb large amount of lithium ions, while their reversible capacity can as much as 1000 mA h g^{-1}[140, 141]. However, the high irreversible capacities of this kind batteries and the lack of stable voltage plateau for CNTs electrodes during discharge have impeded their practical application, so further studies need to be done to overcome this obstacle. In this case, using CNTs as additives in anode materials seems a possible alternative solution. According to the experimental results, it has been proved that the original silicon electrode only has a 300 mAh g^{-1} reversible capacity, and usually fails after 10 cycles, however, a simple mechanical addition of CNTs has highly enhanced the electrode performance, which shows a capacity of 1200 m Ah g^{-1} and an initial coulombic efficiency of 80%[142]. Even better battery performance could be achieved either by incorporating CNTs with other materials or changing the incorporating methods, which suggest that CNTs have a very promising potential for further Li-ion batteries development[140].

To satisfy the growing demand for electronic devices of high power density and long cycle life (for example electronic vehicles), the supercapacitors have been developed. Compared with the tradition batteries, supercapacitors with CNTs usually have higher power density (20 kW kg^{-1} at energy densities of ~7 W h kg^{-1} for MWCNT electrodes), higher capacitance (180/102 F g^{-1} for SWNT/MWNT electrodes), faster charge/discharge speed (7 ms for 10 MWCNT capacitors connected in series which operated at up to 10 V) as well as longer cycle life [143-145]. Their advanced performance needs both improved methods to form the CNT layers and the development of hybrid supercapacitors[139].

For fuel cells, CNTs are usually utilized as catalyst support, comparing with the traditional carbon black material, the CNTs can effectively reduce Pt usage[146]. For solar cells, by addition of the CNTs in a proper way, the optical absorption and carrier transport could be enhanced, which contribute to development of lightweight, flexible polymeric solar cells[147].

Electromechanical actuators based on sheets of SWNTs are firstly reported in 1999[148]. They can generate higher stress than that of natural muscle, and higher strain than high modulus ferroelectrics at low applied voltages (typically a few volts). However, inhibited by the limited control over the SWNT properties, studies have been made to find the possible substitute. In the year 2005[149], due to the relatively high purity, no chirality-related restriction, as well as lower cost of MWNTs, the

MWNTs actuators are proposed, compared with the ancient SWNTs actuators (maximum strain between 0.06~0.2% in aqueous electrolytes, electrochemical capacitance ~30F g^{-1}), the MWNTs actuators have been proved having better performance (maximum stain ~0.2%, electrochemical capacitance ~113F g^{-1}).

Except the devices mentioned above, there are also other electronic device like super CNT springs, foam-like vertically aligned CNTs films as well as many batteries of different form [106, 140, 150], which indicates the CNTs great potential in the energy storage application.

1.4.2.3 Probe and sensor

Due to the outstanding mechanical properties of CNTs, as well as their high length-to-diameter aspect ratio, it suggests that CNTs could be very promising to act as the ideal tips for atomic force microscopy (AFM). Currently, most AFM probes used are made from silicon, borosilicate glass as well as silicon nitride, whose tip diameters range from a few nanometers to a few tens of nanometers. However, these probes are considered consumables, which are often changed when the tip apex becomes dull or contaminated or broken, while each change results in tens of dollars cost at least. Compared with these defects, CNTs can achieve higher diagnostic resolution with a narrower diameter, while its excellent mechanical properties guarantee its long service time. Generally there are two methods for preparing the CNT tips of AFM probes: either attaching previously synthesized nanotube to the probe, or growing the tube in-situ. Fig. 1-17 shows a CNT tip probe[151], which is made by the former method.

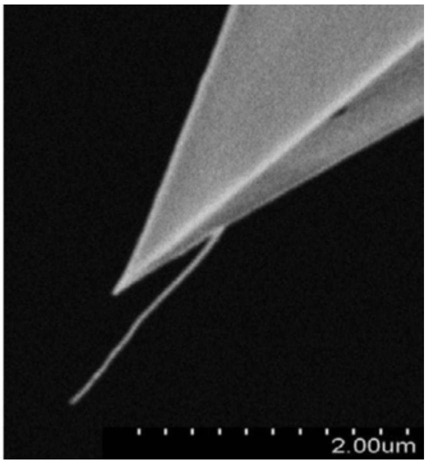

Fig. 1-17 *SEM image for the carbon nanotube tip probe*

CNTs sensor is another application that takes use of CNTs extraordinary properties to achieve specific diagnostic, which includes gas sensor, biosensor, physical sensor, etc. For gas sensors, its principle is the SWNT conductivity change with different gas composition. Now many studies have been carried out in this aspect[133, 152-160], various gases like H_2, CH_4, NH_3, H_2S, O_2, NO_2, insert gas etc. can now be detected by this technique. During the study of biosensors, the addition of CNTs has led better performance compared with the conventional sensors, including more direct diagnostic, higher selectivity for the testing results, as well as high sensitivity[161]. In the physical sensor aspect, besides the CNT tip probe, the use of CNTs as pressure sensors, flow sensors as well as nanobalances have been investigated, which revealed the diversity of CNTs application[104, 162-164]. However, there is still much work to be done to achieve the practical use of these techniques.

1.4.2.4 Carbon nanotubes composite

In order to take full advantage of CNTs outstanding properties, it usually involves the process in which the CNTs composites are prepared. Solution mixing is perhaps the simplest method to obtain the CNTs composites, which can be further used to make CNTs fibers and ribbons[165-168]. In this course, CNTs are firstly dispersed with the polymer solution, and then the solvents are evaporated in a controlled way. A lot of polymers can been used for the solution mixing method, like polyvinyl alcohol, polystyrene, polycarbonate etc. However, as CNTs tends to aggregate in the solution, high speed stirring, ultra sonication and addition of a surfactant are often applied to the solution, while the functionalization of CNTs is made for a better CNTs dispersion, but these treatments may induce side effect for the product properties.

As there are the polymers that can't easily dissolve in common solvents to form the solution, the melt processing method is applied as an alternative for the thermoplastic polymers. A range of polymers has been studied to form the CNTs composites using this method, including polyethylene, polystyrene, polypropylene, polycarbonate, poly (methyl methacrylate) (PMMA), acrylonitrile-butadiene-styrene etc.[169-177]. In this melting process method, the dispersion of CNTs is more difficult than in the solution, and it is harder to reach high CNTs concentration due to the high viscosities. In order to keep CNTs from agglomeration during the process, special approaches like calendaring process, stir and extrusion are usually used to supply sufficient energy to disperse them. Fig. 1-18 shows an example for the calendaring machine with three-roll mills and its general configuration/operating mechanism[178].

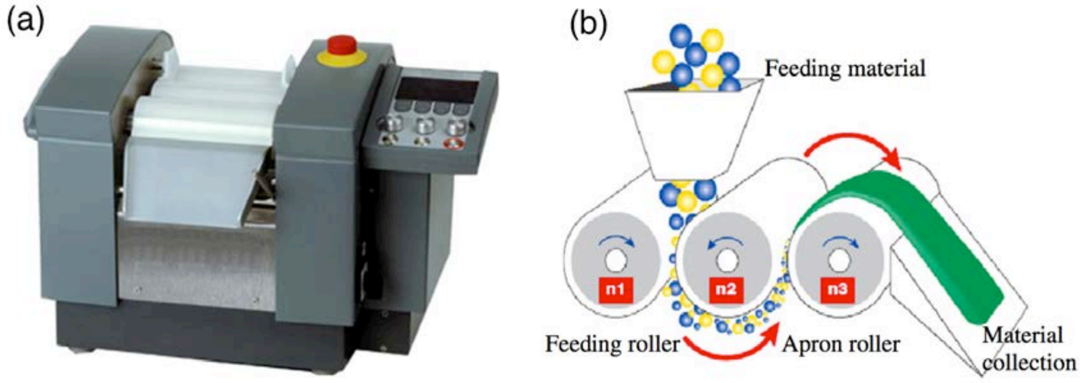

Fig. 1-18 *Calendaring machine used for CNTs dispersion into a polymer matrix (a) and corresponding schematic showing the general configuration and its working mechanism (b)*[178]

There is another method for preparing the CNTs composites that is called in-situ polymerization. In this method, CNTs are firstly mixed with monomers, and then the in situ polymerization process will be carried out via addition or condensation reactions with a hardener or curing agents at an elevated temperature. During the in-situ polymerization process, the covalent bonding between the functionalized CNTs and the polymer matrix could be formed, which can significantly enhance the composite properties. Wolfgang K Maser et al. are among the first to apply this method[179], and they prepared a MWNT/polyaniline composite containing ~50 wt% MWNT. Since then many studies have been done on this aspect, and the composite like MWNT/polystyrene, MWNT/polypyrrole, MWNT/polyurethane and MWNT/nylon were made[180-184].

Latex technology is a relatively new method for the CNTs composite preparation. In this method, the polymer is firstly synthesized from the dispersed discrete polymer particles in the medium, then the CNTs that have a stable dispersion due to the surfactant treatment will be added for mixing. With the subsequent steps like freeze-drying and melt processing, the final CNTs composites will be obtained[185-187]. Besides the latex technology and the other CNTs composite preparation processes that have been mentioned above, other methods like densification, spinning of coagulant, layer-by-layer deposition, pulverization etc. [178] are also applied, each method has its special application range and advantage. In order to obtain the CNTs composite with desired properties, the choice of preparation processes must be thoroughly considered.

CNTs composites made by the preparation processes mentioned above usually have excellent properties. In the mechanical aspect, due to the good interfacial load transfer from low- modulus matrix to high-modulus CNTs, the CNTs composites usually have improved Young's modulus and tensile strength, which are mainly influenced by the CNTs diameter, aspect ratio, loading quantity, dispersion state, alignment, as well as the interface interaction in matrix[185, 188, 189]. For example, according to a study of Moniruzzaman et al[190], in the CNTs/nylon composite case, only 2 wt% addition of SWNTs can result in a 214% improvement in elastic modulus and a 162% increase in yield strength over pure nylon. In the electrical aspect, due to their high performance, CNTs are generally used to increase the CNTs composites conductivity. The percolation theory is usually referred during the relating investigation process, trying to obtain the desired electric properties while not causing negative influences on the CNTs composites properties of other aspects[191-196]. There is a wide range of applications for the conducting CNTs composites[178, 197, 198], such as electrically conducting adhesives, antistatic coatings and films, electromagnetic interference shielding materials, etc. In the thermal aspect, there are some critical factors that determine the thermal conductivity/stability of CNTs composites, such as the CNTs content/ aspect ratio/ dispersion state as well as the CNTs-matrix interfacial interaction[185]. With the investigation progress of these factors, the CNTs composites with high thermal conductivity are synthesized and gradually applied in the applications like connectors, electric motors and generators, heat sinks, thermal interface materials etc.[185]

As mentioned above, CNTs composites made by CNTs and polymer have excellent properties and have been applied in various aspects. However, there still exist other CNTs composites types, where CNTs are mixed with other materials rather than polymer, like CNTs/ceramic composites, CNTs/carbon composites as well as CNTs/metal composites. For CNTs/ceramic composites, their preparations using SiC, hydroxyapatite and a series of oxides like alumina, silica, TiO_2, V_2O_5, nickel oxide etc. have been reported[145, 199-204]. According to the results of these studies, it has been found that the addition of CNTs results in good mechanical and electric properties, and make this kind of composites have various applications in optical wave guides, conductive films, sensors, electrodes, supercapacitors and biomedical applications etc. For CNTs/carbon composites, the CNTs are incorporated into carbon matrices like carbon fibers and graphite. It has been proved that for the composites fibers, their tensile strength, modulus as well as electrical conductivity are greatly enhanced[205, 206], and the CNTs/graphite composites have a great contribution for the enhancement of batteries performance[207, 208]. For CNTs/metal composites, Toru Kuzumaki and his colleagues carried out their pioneering work in 1998, in which CNT/aluminium composites having a significant mechanical properties improvement were prepared[209]. Since then the following studies have been done, other metals like titanium and magnesium are involved for the CNTs/metal composites preparation[210, 211].

1.5 Carbon nanotubes growth mechanism in floating catalyst chemical vapor deposition

To achieve large-scale production of CNTs with well-defined configurations, it's indispensable to have a full understanding about the CNTs growth mechanism. Many studies have been carried out on this aspect right from the CNTs discovery, not only by simulation but also by experiments. However, this topic still has the debatable points even nowadays, which needs supplementary works to provide a more detailed explanation of the whole CNTs growth process.

1.5.1 General mechanism

Detailed insights into the CNTs growth mechanism have their roots in the study of Baker et al. in 1973[212]. In this study, the base growth and tip growth modes of carbon filaments were proposed, which are shown in Fig. 1-19. Generally there are three periods in the growth process, in which the temperature and concentration gradients were proposed as the main driving forces. In the first period, the carbon feedstock will decompose on the exposed surface of the metal particle to release carbon, and the released carbon will dissolve in the particle. For the following step, the dissolved carbon will diffuse through the particle, and then be precipitated for the tubular filament growth, as the tubular structure is more energetically favorable than other forms which have the dangling bonds[213]. Finally, caused by the deactivation of metal catalyst or the lack of carbon source, the growth process ends. The tip growth and base growth modes differ at this carbon precipitation step, which are mainly determined by the interaction between the metal particle and the substrate. For example, for Ni particles on SiO_2, the interaction is relatively weak, thus results in tip growth[214], however, for Co or Fe particles on SiO_2, the interaction is much stronger, which favors the base growth mode[47, 215].

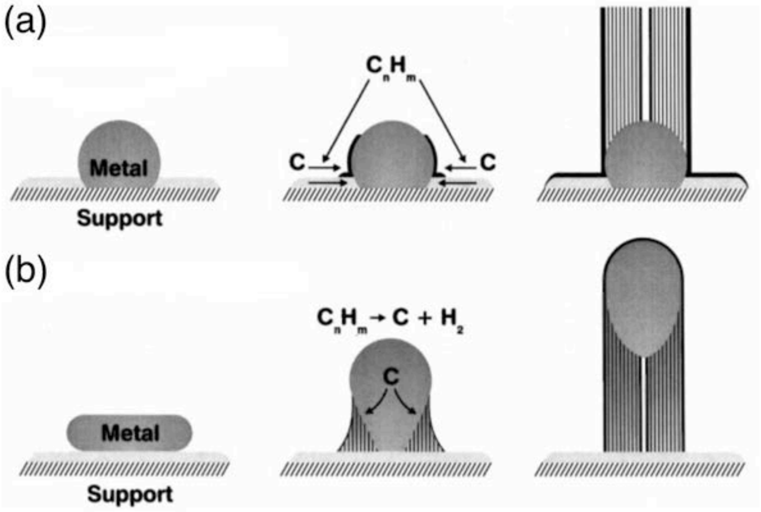

Figure 1-19 *Schematics of (a) base-growth and (b) tip-growth modes for carbon filament growth[216]*

Based on the models mentioned above, in the year 1984, a growth mechanism concerning the catalytically produced MWNTs was proposed[217], which could be described as vapour-liquid-solid (VLS), as it suggests that the catalytic particles might be liquid during the CNTs growth process. However, there may exist problems for this assumption, as even the influences of the particle size and the metal-carbon eutectic state are taken into account, the melting point of the particles is still higher than the CNTs synthesis temperature in some cases[7, 218, 219]. For the chemical state of the catalyst particles, there also exist conflicting reports, in which the carbides state and the metallic state of the particles are supported respectively[13, 220-222].

1.5.2 Mechanism in floating catalyst chemical vapor deposition

Floating catalyst chemical vapor deposition (FCCVD) is commonly used nowadays, as it has all the advantages of the CVD method, and is more convenient for a continuous CNTs production. In FCCVD, carbon sources and catalyst sources are injected simultaneously into the reaction system, thus the catalyst particles formation begins at the gas phase. Compared to the supported catalyst cases discussed in the former paragraph where the catalysts are pre-deposited, CNTs growth by FCCVD is obviously even more complex. Trying to explain the CNTs growth process by FCCVD, a three steps particle-wire-tube mechanism was proposed in 2006[223], as shown in Fig 1-20, with the steps presented as follows: (a) Nanoparticles form from the gaseous C_n species condensation; (b) Self-assembling the nanoparticles into nanowires driven by anisotropic interaction; (c) Nanowires develop into nanotubes by the hollow channel formation.

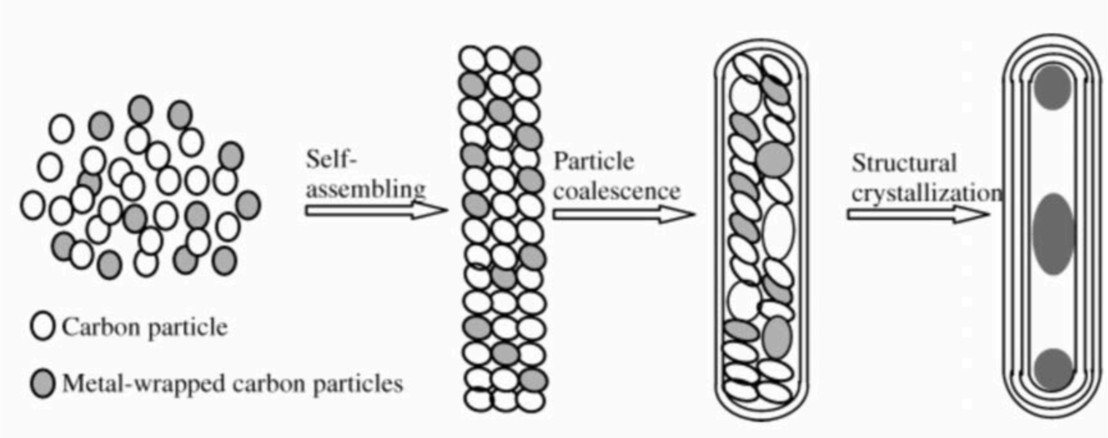

Fig. 1-20 *Schematic diagram of the particle-wire-tube mechanism for nanotube evolution in FCCVD[223]*

For the process presented in Fig. 1-20, there are two key questions need to be paid high attention. The first question is why the NPs are anisotropic, which contribute to a 1D mode assembling. In the report, it suggested that during the NPs formation, numerous defects (including sp^3 carbons, non-hexagonal rings, disconnected bonds etc.) occur, especially at the two edges of the around-curved carbon (not graphite) layers. These defective layered structures might be kinetically stabilized by defect-defect interactions, lip-lip interactions[224] and metal-carbon conjugations[225], which could obstruct their closure into the isotropic graphitic particles and competitively enhance the probability of directional particle-particle interaction and assembling[223]. The second key question is how a nanowire transforms to a nanotube by the hollow channel formation. The structural crystallization and extension due to the relatively low stability of the carbon NPs were believed to be responsible for this transformation. As under thermal annealing, the NPs would exhibit a coalescence tendency and form more extended structures, accompanied with structural crystallization[223]. However, this model is far from perfect to well describe the complex CNT nucleation and growth processes, as there are many factors like catalyst type, CNTs growth location, substrate influence etc. that haven’t been taken into consideration.

From the explanation for the mechanisms presented above, it could be observed that the catalysts play an irreplaceable role on the CNTs growth. However, as the catalyst NPs are formed in the gas phase during FCCVD, it appears very difficult to achieve accurately control over their formation process. Therefor it’s necessary to make further study of catalysts formation control, as well as the relation between the catalyst particles and the final CNTs. Although non-metal catalysts like SiC, Ge and Si have been reported[226, 227], the main catalysts for FCCVD are still transition metals like Fe, Co, Ni, which are in-situ produced by the organometallics decomposition. Therefore in this study, we will focus the attention on the transition metal catalysts, and more particularly on iron (released by the ferrocene decomposition).

1.5.2.1 Beginning location for the carbon nanotube growth

To study the CNTs growth mechanism in FCCVD, it needs to firstly find out the answers for the following questions: (1) whether the CNTs growth begins at gas phase or at substrate; (2) what's the influence of the continuous catalyst supply. A study made by Khavrus et al. in 2010[228] may contribute to answer the first question. In this study, the simultaneous growth and separation of both SWNTs and MWNTs during the same CVD synthesis were achieved, in which the catalysts are the iron particles released by the ferrocene decomposition. It was found that SWNTs were originated in the gas phase, while MWNTs were formed only after the NPs deposition on the substrate. Based on this result, they suggested that the diameter difference of the iron particles could be responsible for this variation. For the very small iron particles (~1nm), they are the origin for the spontaneous growth of SWNTs, and these lightweight SWNTs are carried away with the gas flow. For the larger iron particles, as they are relatively heavier, they are much easier to drop on the substrate before CNTs are growing.

1.5.2.2 Influence of the continuous catalyst supply

During the study of CNTs growth mechanism, it has been proved that CNTs are capable of drawing materials inside[229-233]. Based on this assumption, Rong Xiang et al[234] have designed un experiment, in which they used a sequential feeding of two different catalyst sources Fe and Ni for the CNTs growth, and the catalyst distribution was tracked. The experiment results suggested two conclusion: (a) the bottom ends of CNTs are active growth sites, thus the base growth mode is favorable during the synthesis; (b) catalyst particles experience a constant encapsulation by CNTs, which are kept drawn upward into CNT cavities with the growing CNTs. But the continuous catalyst supply can compensate this catalyst consumption, and result in a continuous CNTs growth. This experiment not only answered the question about the influence of the continuous catalyst supply, but also supported the base growth mode of CNTs. The SEM photo of the synthesized CNT is shown in Fig. 1-21.

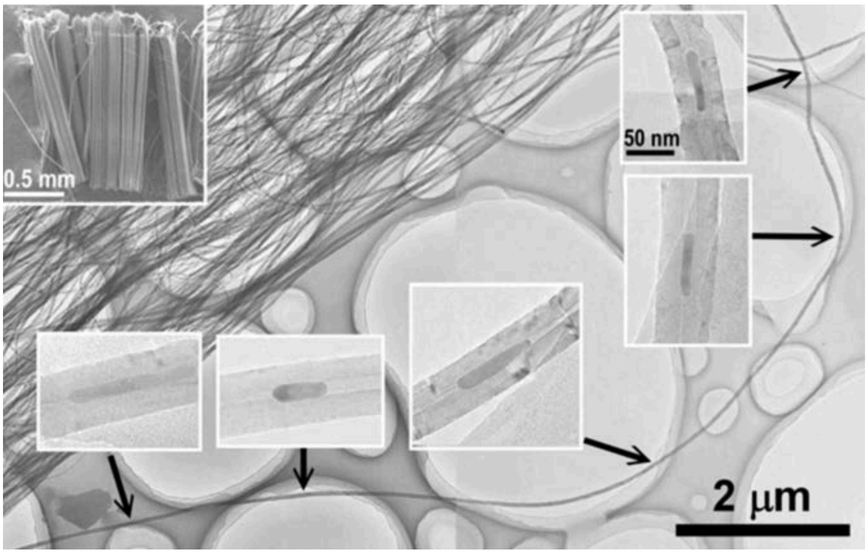

Fig. 1-21 *SEM image of an as-grown 1.5 mm array of CNTs grown by a floating catalyst CVD method with the insets showing the catalyst particles encapsulated all along the CNT*[234]

1.5.2.3 Substrate influence

Except the growth location and continuous catalyst supply influences, there still exist many points remaining open issues. More than the determination of the tip/base growth mode, the variation of substrate can induce significant differences on catalyst features, which will subsequentially influence the CNTs growth mechanism and kinetics. For example, the Al_2O_3 is a commonly used substrate in the Fe-catalyzed CNTs production, as the Fe 2+ and 3+ formed at the interface can effectively restricts Fe surface mobility, and lead to a narrow catalyst particle size distribution with dense vertically-aligned CNTs[235]. The CNTs growth direction is also influenced by the substrate, as Su et al.[236] reported the preferred 2D orientations of SWCNTs grown on silicon-based surfaces, in which the SWNTs grown on Si (100)-based surfaces took two perpendicular directions, but those grown on Si (111)-based surfaces took one of the three directions separated by 60°. The observed orientations were the result of interactions between the nanotubes and the substrate surface lattices, as the surface lattice guided the SWNTs growth to follow a potential minimum path. What's more, for certain substrates, the CNTs growth could even occur without the catalyst, successful CNTs growth was achieved on carbon-implanted SiGe islands[237] and porous alumina[238] respectively, which suggests that more studies should be carried out to search for other high performance substrates.

1.5.2.4 Carbon nanotube nucleation sites

CNTs nucleation process is another key point that needs to be paid high attention. Thanks to the in-situ time-resolved HRTEM technique, the dynamics of this process could be observed and recorded at the atomic scale. Using this technique, Helveg et al. reported the CNTs growth process from methane decomposition over supported nickel nanocrystals[239], as shown in Fig. 1-22. It could be found that the CNT growth was driven by the Ni nanocrystals shape change, as the dynamic formation and restructuring of mono-atomic step edges contributed to the nucleation and growth of graphene layers, resulting in the graphene layers nucleating between a pair of these steps by surface diffusion of carbon toward the edge. The density-functional theory calculation was made for this process, according to its calculation results, the following conclusion could be obtained: (a) Carbon binds more strongly to Ni step edges than to the free closepacked facets on Ni, which contributes to graphene growth at the step edges; (b) The surface transport of C atoms is the rate- limiting step for the CNTs growth. In the view of energy, carbon atoms tend to precipitate from the step edges onto the catalyst surface to form graphene, thus local energy at the step edge site will be decreased.

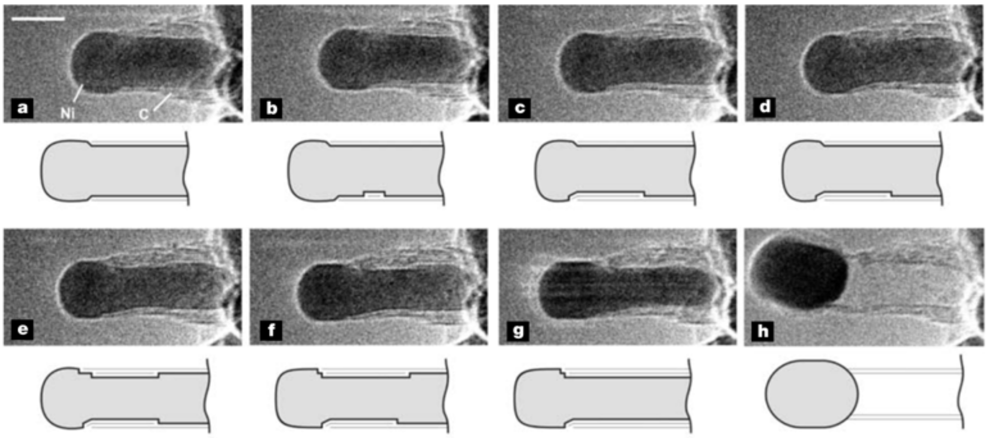

Fig. 1-22 *TEM Images a–h illustrate the elongation/contraction process of a nickel crystal. Drawings are included to guide the eye in locating the positions of mono-atomic Ni step edges at the C–Ni interface. The images are acquired in situ with* $CH_4:H_2= 1:1$ *at a total pressure of 2.1 mbar with the sample heated to 536 °C, with scale bar= 5 nm.[239]*

1.5.2.5 Relation between the carbon nanotube chirality and nucleation

During numerous studies that have been done both experimentally and theoretically for the CNT nucleation process, it has been found that the carbon cap structure is frequently observed in the catalyst NPs[240-243], as shown in Fig. 1-23. This structure consists of six pentagons and some hexagons, like a half fullerene. Generally the caps number increases with the CNTs diameter, and a finished cap results in one nanotube[244]. The influence of this cap structure on the CNT chirality has been widely discussed. In the year 2006, Stephanie Reich et al. [245] carried out a study about controlling the chirality of carbon nanotubes by epitaxial growth. According to their calculation results, they suggested that the CNTs chirality is determined during the nucleation process, and the formed cap has a direct relation with the final CNT, thus by well controlling the cap geometry, structure and energy at the early nucleation stage, the chirality-selective growth of CNTs could be achieved.

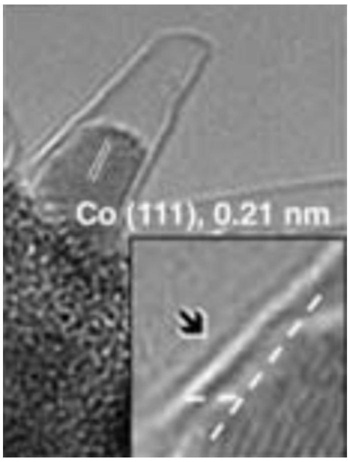

Fig. 1-23 *A step site on the surface of a Co nanoparticle, with an enlarged view in the inset. The lattice fringes corresponds to the (111) lattice plane of cobalt*[240]

In summary, catalyst particles with high local curvature surface are indispensable for the CNTs growth. The dynamic formation and restructuring of mono-atomic step edges on catalyst particles contributes to the nucleation and growth of graphene layers. The diameter and structure of nanotubes are controlled by the geometry, size and orientation of catalyst particles. During the CNTs growth process, carbon atoms could diffuse through catalyst particle by bulk or (and) surface diffusion. The CNTs growth rate is determined by the reshaping process of catalyst, as well as the carbon adsorption, diffusion or precipitation on the catalyst particles.

1.6 Conclusion

In this chapter, we have firstly introduced some basic knowledge about the CNTs origin and their perfect 1D structure. After years of study, various CNTs synthesis routes like arc-evaporation, laser ablation, chemical vapor deposition as well as many other methods have been designed to serve different requirements. The synthesized CNTs reveal extraordinary properties in different aspects, which attract high attention over the world to explore their huge application potentials such as electronic devices, energy storage, probe and sensor etc. Especially, a variety of the CNT composites are largely investigated because of their novel properties and attractive application potentials in a wide range of fields. In order to achieve large-scale production of CNTs with well-defined configurations, the CNTs growth mechanism study has been carried out for years. However, due to the complexity of the multi physical-chemical process, further study is highly required to achieve a better control on the CNTs synthesis.

Chapter Ⅱ Experimental procedure

Due to their extraordinary intrinsic properties, CNTs are highly desired for a wide range of applications from energy storage[140, 246] to environmental remediation[247, 248] and structural composites[249]. These properties of CNTs, such as conductivity, thermal stability, stiffness, and surface area are determined by their length, diameter, wall numbers and how the carbon atoms are arranged within the graphene wall[250]. However, the ability to produce CNTs with specific and uniform properties at a large scale still remains an unsolved challenge and often requires several post-treatment steps[251]. Researches on the CNTs growth process, especially on the early stages need to be promoted to provide new insights on the CNTs formation principle.

In this chapter, the CNTs synthesis process through aerosol-assisted floating catalyst chemical vapor disposition (FCCVD) is presented firstly, including the materials and equipment used in this research. Various diagnostic methods conducted during/after this process are introduced subsequently. These diagnostic methods have been classified as ex-situ characterization methods and in-situ characterization methods. The former includes microscope, Raman, Thermogravimetric Analysis (TGA) etc., by which samples information are collected after the CNTs synthesis. The latter includes Laser Induced Incandescence (LII), Mass Spectrometry (MS), thermocouple thermometer, etc., by which the information about the synthesis can be obtained real-timely.

2.1 Floating catalyst chemical vapor deposition synthesis of carbon nanotubes

2.1.1 Materials

In this research, several materials are used including carrier gas, carbon/catalyst sources and substrates. Main involved materials are listed in Table 2-1, in which the micro alumina particles exhibited a multiphase crystallographic structure, containing mostly the thermodynamically stable hexagonal α-Al2O3, and to a lesser extent metastable tetragonal δ and monoclinic θ phases, and no evident phase-transformation occurred when the micro alumina particles were heated at temperatures up to 800°C[252].

Table 2-1. *Information of main materials used in this experiment.*

Materials	Molecular formula	Physical states	Purity	Notes
Argon	Ar	Gas		Carrier gas
Acetylene	C_2H_2	Gas		Carbon source
Ferrocene	$Fe(C_5H_5)_2$	Solid	99%	Alfa Aesar
Hydrogen	H_2	Gas		Carrier gas
Micro alumina particles	Al_2O_3	Solid (size in 3-10 μm)	99.8%	Containing SiO_2 (800ppm), Na_2O (600ppm), Fe_2O_3 (150ppm) and CaO (70ppm)
Xylene	C_8H_{10}	Liquid	98.5+%	Assay, isomers plus ehtylbenzene, Alfa Aesar

2.1.2 Experiment system and process

Before the synthesis process by the floating catalyst chemical vapor deposition (FCCVD), the solid-state catalyst precursor ferrocene was firstly dissolved into the carbon source solvent xylene to form a solution. A spray composed of two concentric tubes of 0.5 mm diameter was used to bring this solution into the reactor, and make the solution change from its liquid state into small droplets (aerosol). As shown in Fig. 2-1, the tube above was connected with the gas flow, which was controlled by digital mass flow meters (Bronkhorst, France). The tube below was connected with the liquid solution, which was controlled by a syringe system fitted with a liquid flow meter (Razer Science, R99-E). Once the liquid solution comes out at the nozzle of the tube, the high-speed gas flow will favor the atomization of the liquid, producing small droplets and bring them into the reaction zone, thus increase the liquid-gas interfacial between the liquid droplets with the surrounding gas atmosphere. To achieve a better vaporization of this spray, a preheating system was set up at the spray position, giving an extra heating for the droplets. For both the high-speed gas flow and the preheating system, they achieve an energy transfer to the liquid solution, thus increase the surface energy of the small droplet and favors the dispersion of the carbon/catalyst precursors[18].

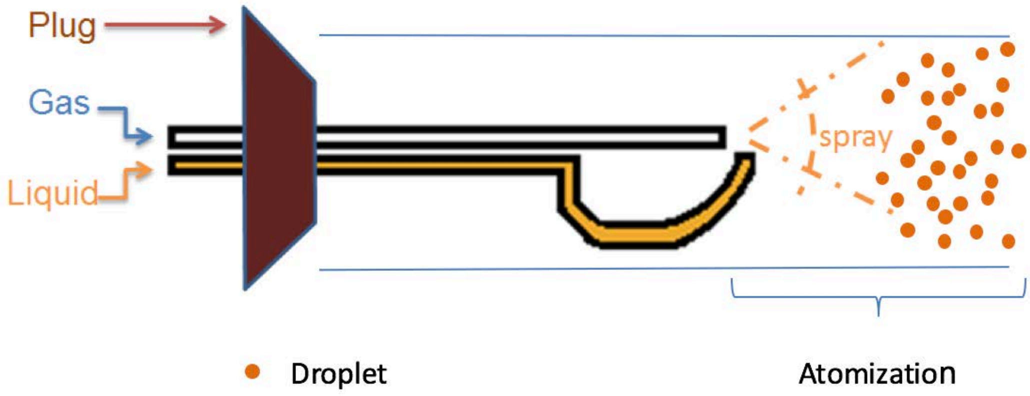

Fig. 2-1 *Scheme illustration of the solution spray*

After the solution atomization process, nanoparticles (NPs) and CNTs were synthesized under atmospheric pressure in a horizontal CVD reactor using a 1,200 mm long quartz tube with an inner diameter of 45 mm as the reactor (Fig. 2-2). The reactor was heated by a three-zone electrical furnace (CARBOLITE HZS) to preset temperature (ranging from 550℃ to 850℃) under 1 L·min^{-1} argon flow. The length of the heating zone is 60cm. The temperature profiles along the heated zone under the mentioned gas flow rate at the temperatures ranging from 550℃ to 750℃ are shown in Fig. 2-3. The exact values for these profiles are shown in Table 2-2. The abscissa distance increases along with the gas flow direction. All these temperature data were tested by testo-922 thermocouple.

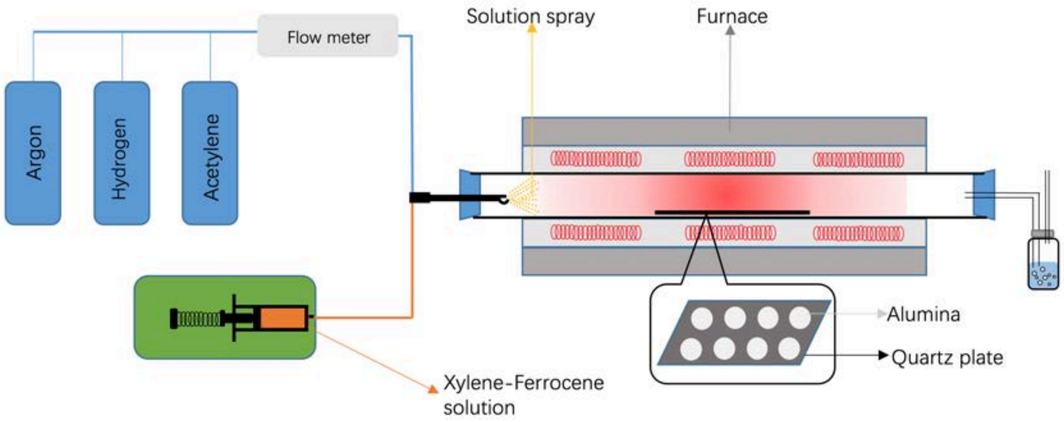

***Fig. 2-2** Scheme illustration of the FCCVD system*

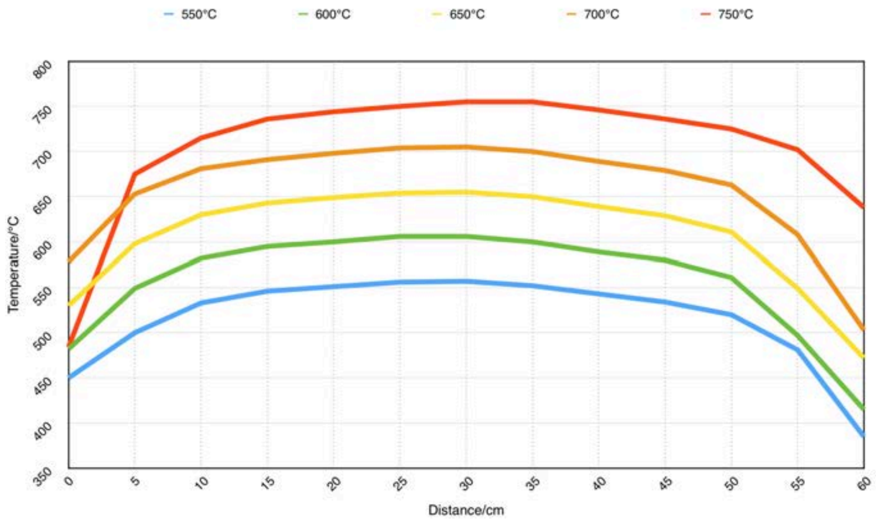

Fig. 2-3 *Temperature profiles along the reactor of the 45 mm diameter quartz tube at different setting temperatures.*

Table 2-2. *Temperature values measured along the center of the high temperature furnace at different set temperatures.*

Distance/cm	550 °C	600 °C	650 °C	700 °C	750 °C
0	450	482	530	578	484
5	500	549	598	653	675
10	533	582	630	681	715
15	546	595	643	691	736
20	551	600	649	698	744
25	556	606	654	704	750
30	557	606	655	705	755
35	552	600	650	700	755
40	543	589	639	689	746
45	534	580	629	679	736
50	520	561	611	663	725
55	481	497	549	608	702
60	385	415	472	503	638

Once the reactor reached the given temperature, hydrogen was introduced and the system was stabilized for 15 min. To eliminate possible side effects from impurities in the gas composition, high purity hydrogen (99.99%) was utilized with levels of O_2 and H_2O as low as 0.1 and 0.5 ppm, respectively. According to the tube size, we know the relations below,

$$V_{tube} = \frac{1}{4}\pi D_{tube}^2 L_{tube}$$
$$P_{H_2}^{After} \cdot V_{tube} = P_{H_2}^{Before} \cdot V_{tube} + F_{H_2} \cdot \Delta t - P_{H_2}^{Before} \cdot F_{gas} \cdot \Delta t$$

where V_{tube}, D_{tube}, L_{tube}, P_{H_2}, F_{H_2}, F_{gas}, Δt are volume of the quartz tube, inner diameter of the quartz tube, length of the quartz tube, hydrogen percent in the gas, hydrogen flow rate, total gas flow rate and tiny period of time respectively.

Based on the relations above, simulation was made and the results were shown in Fig.2-4. The vertical axis represents the ratio between the hydrogen percentage in the reactor and hydrogen percentage in the injected gas flow. It could be found that the necessary stabilization time decreases with the augmentation of the total gas flow, as the stabilization time is 5 min, 10 min and 20 min corresponding to $2\,\mathrm{L\cdot min^{-1}}$, $1\,\mathrm{L\cdot min^{-1}}$ and 0.5 $\mathrm{L\cdot min^{-1}}$ flow rate respectively. As in this research the total gas flow always keeps at $1\,\mathrm{L\cdot min^{-1}}$, 15 min is enough to achieve the gas composition stabilization. Once the reaction atmosphere became stable, the processor was injected into the reactor by the syringe system. Acetylene was also added to the system at varying flow rate to serve as an additional carbon source. For the CNTs synthesis experiments, the injection of all carbon and catalytic sources was stopped after 10 min and the reactor was cooled down to room temperature under argon and hydrogen atmospheres. For the nanoparticle evolution research, this experiment time was augmented according to study requirement. Two different substrates were used in this study: quartz plates and micro-spherical alumina particles (μAl_2O_3, size ranging in 3-10 μm, with 99.8% purity including 800 ppm SiO_2, 600 ppm Na_2O, purchased from Performance Ceramic company, Peninsula, OH, USA). The CNTs growth on these substrates was generally located at a fixed position in the middle of the heated zone

(20-30 cm) where the temperature was constant, except the case in which the position influence was studied.

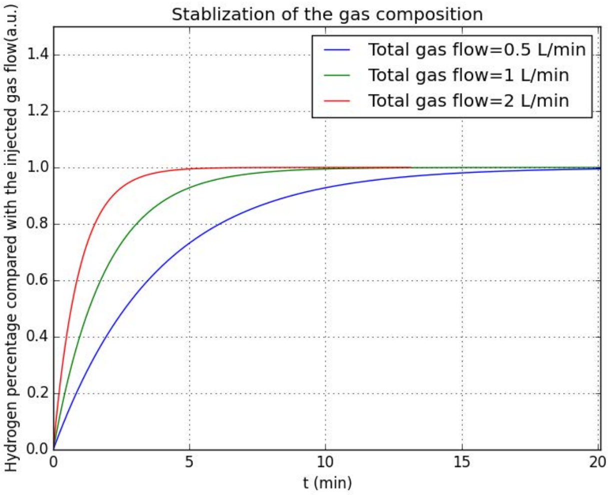

Fig.2-4 *Simulation for the gas stabilization time*

2.2 Ex-situ characterization methods

In this study, the ex-situ characterization methods include microscopy, Raman, TGA etc., by which samples information are collected after the CNTs synthesis. These characterization methods, as well as their applications are introduced below.

2.2.1 Microscopy

The microscopes system used in this research includes an optical microscopy, a scanning electron microscopy (SEM) as well as transmission electron microscopes (TEM). The optical microscope is Leica DMLM, the SEM is a ZEISS LEO 1530 Gemini FEG instrument, and the TEM was performed using JEOL 1200 EX and a FEI Titan instrument equipped with an aberration-corrected condenser. For the optical microscope, it was mainly used to observe the droplet size evolution along with the experiment conditions such as preheat temperature, solution concentration and injection speed. The sample of the optical microscope is illustrated in Fig.2-5 (a). SEM gives direct observation of CNTs morphology with its example show in Fig.2-5 (b). However, when the magnification is highly augmented (more than 100k), the focus adjusting becomes difficult and it's hard to get distinct images. At this time TEM was used, which achieves a much high magnification. The TEM also allows seeing the inner diameter/wall numbers of the synthesis CNTs, as well as the nanometer scale nanoparticles. The TEM sample of CNTs is shown in Fig.2-5 (c) below. Besides the morphology observation function, the TEM FEI Titan includes the energy dispersive spectrometer (EDS) module, by which the sample's elemental composition information could be obtained.

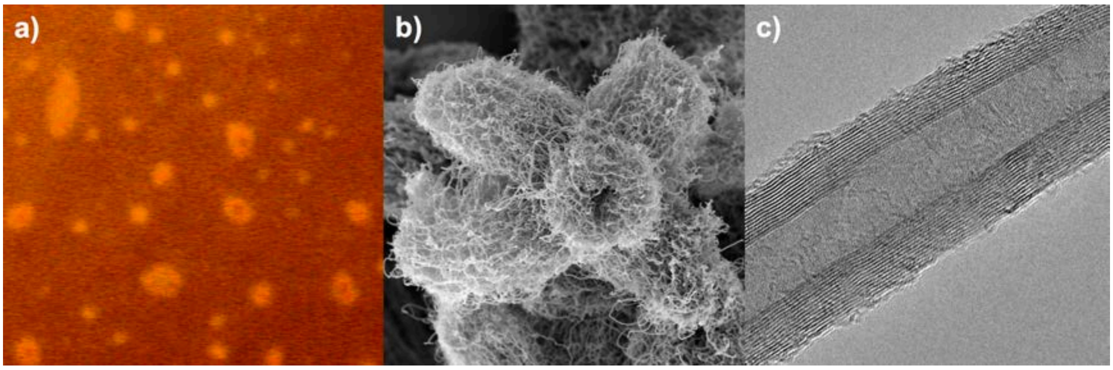

Fig. 2-5 *Sample images taken by (a) optical microscope (b) SEM and (c) TEM*

2.2.2 ***Raman spectroscopy and Thermogravimetric analysis***

Raman spectroscopy and Thermogravimetric analysis (TGA) were also ex-situ characterization methods used in this research. For Raman test, the results were recorded over the range of 1000–2000 cm^{-1} with a spectral resolution of 1 cm^{-1} by a LabRAM Horiba Raman spectrometer using the 632.8 nm emission of a He-Ne laser source. Samples were analyzed by registering the spectra for each specimen randomly on three different positions. All recorded curves were baseline and fitted using Lorentzian line shapes. In this study the two main vibrational modes G (~1580 cm^{-1}) and D (~1330 cm^{-1}) bands are paid close attention. For the G band, it is attributed to the orders sp^2 hybridized carbon network, while the D band corresponds to sp^3[253]. As the CNTs are comprised of one or several sheets of hexagonally packed carbon atoms rolled into concentric seamless cylinders, the graphite mode G band is favorable for a no imperfection structure while the D band is related to local defects. Therefore the D- and G-peak intensities were used for the calculation of the I_G/I_D ratios to evaluate the nanostructure state of CNTs[254].

TGA analyses were conducted in air on a Netzsch analyzer (STA 449 F3 Jupiter) using a thermo-program between 50 and 900 °C at a heating rate of 10 °C/min. In the analyses process, with the gradual augmentation of temperature, the mass loss of the production increases, due to the oxidation of the tested sample. By this result the TGA/DSC curves could be drawn, which reveals the information of thermo stabilization quality of the product. For the CNTs samples in this study, the mainly mass loss is due to the oxidation of CNTs, the carbon element transforms into CO_2 during the process, with iron (from the decomposition of ferrocene) changing to iron oxides, so the TGA result could be used to evaluate the ratio between amorphous carbon and the total production mass, which contributes to the CNTs quality analyses. The reaction occurring during TGA is shown below[18]:

$$3C + 2O_2 \rightarrow 2CO + CO_2$$

$$4Fe + 3O_2 \rightarrow 2Fe_2O_3,\ \ 3Fe + 2O_2 \rightarrow Fe_3O_4$$

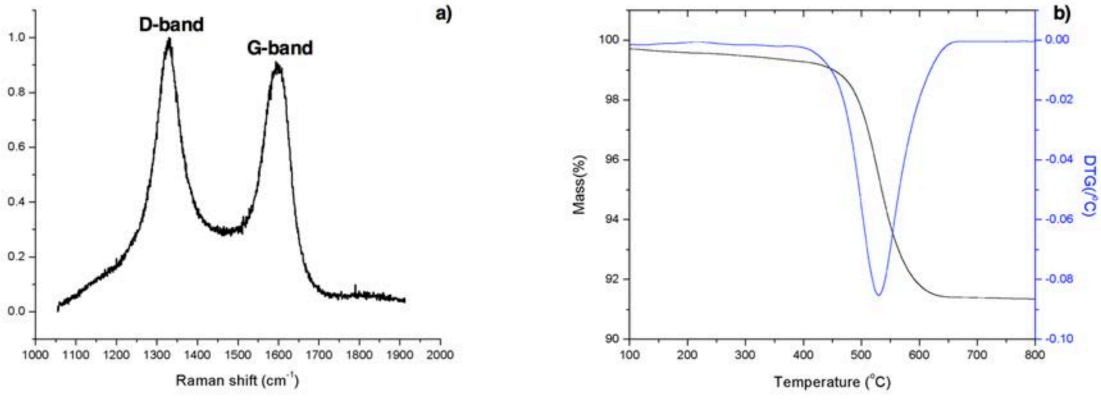

Fig.2-6 *Examples for the (a) Raman (b) TGA/DTG results for CNTs samples under*

experiment conditions: Reactor temperature 650°C, 0.88L/min argon, 0.1L/min H_2, 0.02L/min C_2H_2, ferrocene/xylene solution 0.01g/mL with 0.2mL/min solution injection speed, alumina substrate.

2.3 in-situ characterization methods

Besides the results that can be obtained by the ex-situ characterization methods, there are still many evolutions/reactions during the experiment process that need to be uncovered and give out a real-time feedback, such as temperature profile variation, the gas composition change and the precursor transformation. This information will give evidence to analyze what exactly happen during the synthesis, thus contributes to uncover the unknown of the CNTs growth mechanism, and results in better control and optimization of the CNTs production. So in this study the in-situ characterization methods such as thermocouple, MS and laser induced incandescence technique (LII) were applied. As the thermocouple thermometer has been mentioned in the description of FCCVD system, the LII and MS will be presented below.

2.3.1 Laser induced incandescence technique

2.3.1.1 Laser induced incandescence history

In the 1970s, the laser-based diagnostic technique LII technique was firstly presented by Weeks and Duley[255] and by Eckbreth[256]. It has been found that when an intense laser pulse is applied to the soot particles, the particles irradiated will release a momentary emission of light that related to the particle size and composition information. Many researches has been made based on this finding since then, at the year 1984, Melton published his work, in which the equations governing the laser heating and vaporization of particle have been improved, confirming the LII practicability on the measurement of particle size and its volume fraction[257]. At the year 1995 and 1996, the particle sizing use of time-resolved LII have been demonstrated by two groups[258, 259], and the results in these work have been proved by the TEM observation[260]. In 2002, R. Vander Wal et al. firstly published the LII application on the CNTs flame synthesis[261], which revealed the possibility of using this technique during the CNTs synthesis. Nowadays, the LII has been widely used for the volume fraction and suspended particles size measurement, such as in combustion, vehicular engine and exhaust gas.

2.3.1.2 General laser induced incandescence measurement process

The overall LII system used in this research was shown in Fig.2-7, a general LII measurement process usually includes the following processes:

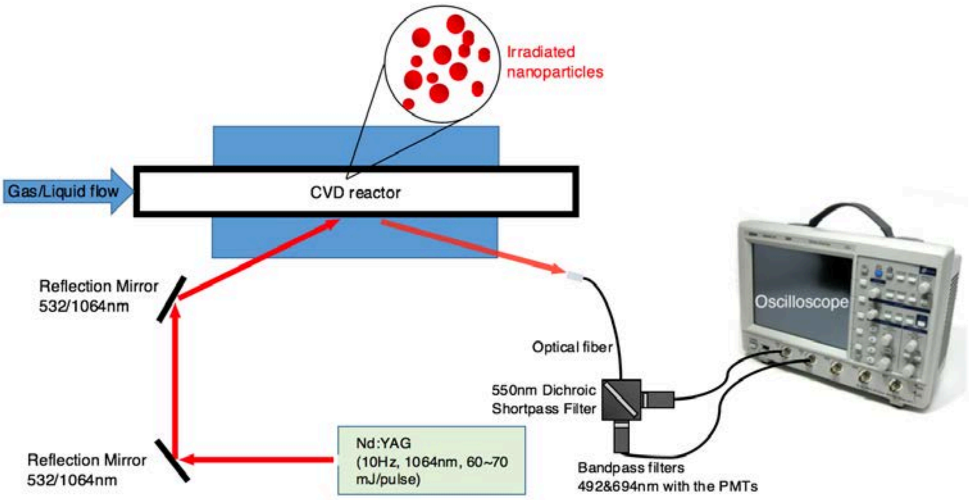

Fig. 2-7 *Schematic of the overall LII system*

1. Firstly a laser pulse is released, this laser pulse will pass through an aperture of ~ 1.5cm and into the reactor, then after its transmission of the quartz tube, it will irradiate the suspended particles and be absorbed. The laser pulse operated is a non-focalized 1064-nm light from a pulsed 2 Hz Nd:YAG laser (Excel, Surelite II-10) with a pulse time of 7 ns and a beam diameter of 7 mm. The laser intensity has been measured by an energy-meter (Gentec-EO SOLO2 with a power detector UP19K-15S-VM-D0) in this stage, its average

value is ~70mJ per pulse, corresponding to ~ $0.2\,\mathrm{J\cdot cm^{-2}}$.

2. Secondly, exposed under the laser pulse, the particles temperature increases sharply due to the energy absorption. In our study, the temperature will increase nearly up to 3000K within several nano seconds (according to a Two-color Pyrometry diagnostic which will be discussed later). At such high temperature, the particles radiation increases, and the LII phenomenon occurs. In this process, the absorption is dominant for the particles heat transfer, and the other heat transfer forms like conduction, radiation, evaporation etc. only have relatively small influences on the internal energy change for the particles. This stage is only several nano seconds.

3. Thirdly, the laser pulse terminates, but the particles temperature are still high, so the cool-down process begins, particles temperature decreases due to the heat transfer such as conduction, radiation, evaporation etc., to achieve the heat exchange with the surrounding gas. The thermal radiation that leads to LII phenomenon recedes. This stage will last ~100 ns.

4. The LII evolution during the 2 and 3 stages is detected and recorded. These results, including the LII intensity and attenuation time are analyzed, which will be compared with the simulation results from the model, to find the particles size and volume fraction information[262, 263]. Sometimes supplementary techniques such as Two-Color Pyrometry and TEM will be used, to calibrate the acquired conclusions. In this research, the LII detector system established including the following components: (a) an optical fiber which can transfer the LII from the local position to the detector system; (b) a filter system which can separate the LII signal in different spectra containing one 550nm Dichroic Shortpass Filter and two Bandpass filters 492&694nm with 10nm FWHM (Edmund optics); (c) Two identical PMTs (Hamamatsu,

H10721-20) equipped with their amplifications (Hamamatsu, C5594-44), and the corresponding power supplies (Hamamatsu, C10709&C7169); (d) a 2 GHz digital storage oscilloscope (Lecroy, Wavejet 354A) by which the LII data were stored. These data will be used to draw the real LII signal curves, which will be compared with the established simulation result, to determine the nanoparticles (NPs) size in the experiment

2.3.1.3 Laser induced incandescence heat transfer model

To analyze the data obtained by the detection system, it is necessary to establish a proper model. For LII signal, its magnitude is correlated with particles volume fraction, and its signal decay time is associated with the primary particle size[264]. The relation between its signal and the time should be constructed. The LII measurement process involves several heat transfer types, according to the previous work reported by other groups[262], the principal energy-balance equation for one particle is like below, based on the fact that in one detection, the particles are heated up by laser pulse only once.

$$\frac{dU_{\text{int}}}{dt} = \dot{Q}_{abs} - \dot{Q}_{rad} - \dot{Q}_{cond} - \dot{Q}_{\text{Sub}} \qquad \text{Equation (1)}$$

where U_{int}, $\dot{Q}_{abs}$, $\dot{Q}_{rad}$, $\dot{Q}_{cond}$, $\dot{Q}_{sub}$ correspond the internal energy for the single tested spherical particle, the rate of energy gained by laser absorption, the rates of energy lost by radiative emission/ conduction/ sublimation and photo desorption respectively.

This energy balance is shown in Fig.2-8, in which there are some heat transfer processes which have been neglected, including heat loss of oxidation, molecular arrangement etc., This is because in our experiment conditions, these kinds of heat loss are relatively too weak[265, 266].

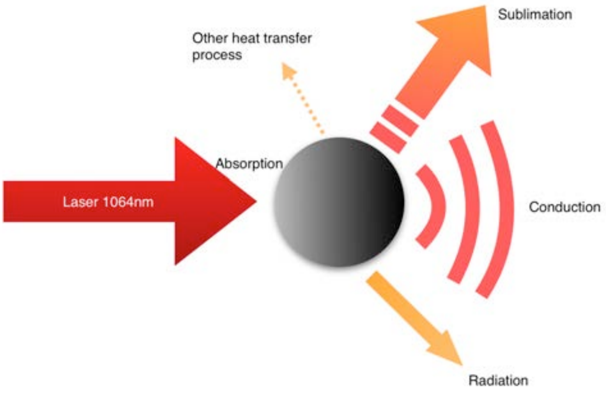

Fig. 2-8 *Energy balance in a single spherical particle during heating by a laser pulse and cooling through different heat transfers*

For the particle internal energy, we have $\frac{dU_{\text{int}}}{dt} = \frac{dMC_{p_p}T_p}{dt}$, where M, C_{p_p}, T_p are the nanoparticle mass, the specific heat of nanoparticle and the particle temperature respectively, they may change during the heat transfer. In this case, we have the equations below,

$$\frac{dU_{\text{int}}}{dt} = MC_{p_p} \cdot \frac{dT_p}{dt} + C_{p_p}T_p\frac{dM}{dt} + MT_p\frac{dC_{p_p}}{dt} \qquad \text{Equation (2)}$$

$$M = \frac{4}{3} \cdot \pi r_p^3 \rho_p \qquad \text{Equation (3)}$$

where r_p is the radius of the nanoparticle, ρ_p is the density of the nanoparticle, which need to be determined according to the NPs properties.

For the absorption part, as the nanoparticles in this study have small sizes compared to laser wavelength, it satisfies the Rayleigh limit, so we have the equations below,

$$\dot{Q}_{abs} = 8 \cdot E(m) \cdot q(t) \cdot \frac{\pi^2 r_p^3}{\lambda} \qquad \text{Equation (4)}$$

$$E(m) = \frac{\lambda_w}{8\pi r_p} \qquad \text{Equation (5)}$$

where $E(m)$, $q(t)$, λ, λ_w are dimensionless refractive index, laser temporal fluence, laser wavelength and effective band for laser.

For the radiation part, it follows the Stefan-Boltzmann law, and the equation is shown below,

$$\dot{Q}_{rad} = \sigma \cdot \varepsilon \cdot \left(T_p^4 - T_g^4\right) \cdot 4 \cdot \pi \cdot r_p^2 \qquad \text{Equation (6)}$$

with σ as Stefan-Boltzmann constant $5.6704 \times 10^{-12} \mathrm{W \cdot cm^{-2} \cdot K^{-4}}$, ε as emission coefficient of nanoparticle and T_g as temperature of the surrounding gas. As the heat loss of radiation is usually relatively low compared with the conduction and sublimation[264, 267], it is assumed $\varepsilon = 1$ in this study to simplify the calculation.

For the conduction part, we have the equation below,

$$\dot{Q}_{cond} = \frac{1}{2} \alpha_T \pi r_p^2 P_g \sqrt{\frac{8 k_B T_g}{\pi m_g}} \frac{\gamma + 1}{\gamma - 1} \left(\frac{T_p}{T_g} - 1 \right) \qquad \text{Equation (7)}$$

where α_T, P_g, k_B, m_g, γ are thermal accommodation coefficient, gas pressure (generally supposed to be 1 atm in this study), Boltzmann constant ($k_B = 1.381 \times 10^{-23} \mathrm{J \cdot K^{-1}}$), average molecular weight of the gas molecules and heat capacity ratio of the gas. As in this study, the gas component is complex due to the decomposition of the reactants, m_g and γ change with the experiment conditions, for a gas mixed with the composition i, we have $m_g = \frac{\sum_i n_i \cdot m_{gi}}{\sum_i n_i}$, $C_{P_g} = \frac{\sum_i n_i \cdot C_{p_g i}}{\sum_i n_i}$ and $\gamma = \frac{C_{P_g}}{C_{P_g} - R}$, where n_i is the amount of substance for the gas component i, C_{P_g} is the molecular heat capacity of gas and R is gas constant ($8.3145 \mathrm{J \cdot mol^{-1} \cdot K^{-1}}$)

For the sublimation part, its heat loss becomes very important at the high temperature[267], as in this study the maximum temperature could arise to ~3500K, it is reasonable to take this part into consideration. And we have the following equations [262, 268],

$$\dot{Q}_{\mathrm{Sub}} = -\frac{\Delta H_V}{W_V}\frac{dM}{dt} = \frac{\Delta H_V}{W_V}\frac{4\pi r_p^2 W_V \alpha_M p_V}{R_p T_p}\left(\frac{R_m T_p}{2W_V}\right)^{0.5}$$

$$p_V = p_{ref}\exp\left[-\frac{\Delta H_V}{R}\left(\frac{1}{T_p}-\frac{1}{T_{ref}}\right)\right].$$

Where ΔH_V is the average enthalpy of formation of sublimed species, W_V is the average molecular weight of sublimed species, α_M is mass accommodation coefficient of vaporized carbon clusters, p_V is average partial pressure of sublimed species, $R_p = 83.145\,\mathrm{bar \cdot cm^3 \cdot mol^{-1} \cdot K^{-1}}$ is gas constant in effective pressure units, $R_m = 8.3145\times10^7\,\mathrm{g \cdot cm^2 \cdot mol^{-1} \cdot K^{-1} s^{-2}}$ is gas constant in effective mass units, and p_{ref} is reference pressure in Antoine and Clausius-Clapeyron equations[262]. Combing the equation mentioned in this sublimation part, we have

$$\dot{Q}_{\mathrm{Sub}} = \frac{\Delta H_V}{W_V}\frac{4\pi r_p^2 W_V \alpha_M p_{ref}\exp\left[-\frac{\Delta H_V}{R}\left(\frac{1}{T_p}-\frac{1}{T_{ref}}\right)\right]}{R_p T_p}\left(\frac{R_m T_p}{2W_V}\right)^{0.5} \qquad \text{Equation (8)}$$

According to the Equation (1) to (8), we have the equation descripting the nanoparticle temperature change with the time

$$\frac{dT_p}{dt} = \frac{6\pi E(m)\cdot q(t)}{\rho_p C_{p_p}\lambda} - \frac{3\cdot\sigma\cdot\varepsilon\cdot\left(T_p^4 - T_g^4\right)}{r_p\rho_p C_{p_p}} - \frac{3\alpha_T P_g\sqrt{\frac{2k_B T_g}{\pi m_g}}\frac{\gamma+1}{\gamma-1}\left(\frac{T_p}{T_g}-1\right)}{4r_p\rho_p C_{p_p}} - \frac{T_p}{C_{p_p}}\cdot\frac{dC_{p_p}}{dt}$$
$$-\frac{3\cdot\left(\frac{\Delta H_V}{W_V} - C_{p_p}T_p\right)\frac{W_V\alpha_M p_{ref}\exp\left[-\frac{\Delta H_V}{R}\left(\frac{1}{T_p}-\frac{1}{T_{ref}}\right)\right]}{R_p T_p}\left(\frac{R_m T_p}{2W_V}\right)^{0.5}}{r_p\rho_p C_{p_p}}$$

However, according to the results tested by the energy-meter, it could be found that the laser intensity isn't stable, it changes with laser incident angle and there is always energy loss during laser transmission, it makes the part absorption not reliable, the heat absorption part must be adjusted or replaced for a more certain data (discussed in the Annexes part). To achieve this goal, Two-color Pyrometry method was applied. It is a well-established method for temperature measurement. In this method, two different spectral bands should be selected, and the particle temperature could be calculated according to the detected signals in two different wavelengths[269, 270], as

$$T_p = \frac{hc}{k_B}\left(\frac{1}{\lambda_2}-\frac{1}{\lambda_1}\right)\left\{\ln\left[\frac{S_p(\lambda_1,T_p)}{S_p(\lambda_2,T_p)}\frac{S_{bb}(\lambda_2,T_{bb})}{S_{bb}(\lambda_1,T_{bb})}\frac{\varepsilon(\lambda_2)}{\varepsilon(\lambda_1)}\right]+\frac{hc}{k_BT_{bb}}\left(\frac{1}{\lambda_2}-\frac{1}{\lambda_1}\right)\right\}^{-1}$$

where $\frac{S_{bb}(\lambda_2,T_{bb})}{S_{bb}(\lambda_1,T_{bb})}=\frac{\lambda_1^5}{\lambda_2^5}\frac{e^{\frac{hc}{\lambda_1 kT_{bb}}}-1}{e^{\frac{hc}{\lambda_2 kT_{bb}}}-1}$. As in this study the nanoparticles are small enough for the Rayleigh limit, $\frac{\varepsilon(\lambda_2)}{\varepsilon(\lambda_1)}\approx\frac{\lambda_1}{\lambda_2}$, so finally we have

$$T_p = \frac{hc}{k}\left(\frac{1}{\lambda_2}-\frac{1}{\lambda_1}\right)\left\{\ln\left[\frac{S_p(\lambda_1,T_p)}{S_p(\lambda_2,T_p)}\frac{\lambda_1^5}{\lambda_2^5}\frac{e^{\frac{hc}{\lambda_1 kT_{bb}}}-1}{e^{\frac{hc}{\lambda_2 kT_{bb}}}-1}\frac{\lambda_1}{\lambda_2}\right]+\frac{hc}{kT_{bb}}\left(\frac{1}{\lambda_2}-\frac{1}{\lambda_1}\right)\right\}^{-1} \quad \text{Equation (9)}$$

where h=6.626×10^{-34} J·s is the Planck constant, c= 2.998×10^{10} cm/s is the speed of light, λ_1 and λ_2 are the two selected detection wavelengths (in this study they are 492nm&694nm). While S_p is the measured LII signal intensity, S_{bb} is the signal from a black body radiator at the temperature T_{bb}.

In this way, the heat-up process of the nanoparticle could be canceled. Instead, the maximum temperature, which is reached at the end of the laser pulse, will be taken as the initial condition. The time zero of LII signal is set at the start moment of this nanoparticle cooling down. All needs to be considered is the particle cooling process. Thus we have

$$\frac{dT_p}{dt} = -\frac{3\cdot\sigma\cdot\varepsilon\cdot\left(T_p^4 - T_g^4\right)}{r_p\rho_p C_{p_p}} - \frac{3\alpha_T P_g\sqrt{\frac{2k_B T_g}{\pi m_g}}\frac{\gamma+1}{\gamma-1}\left(\frac{T_p}{T_g}-1\right)}{4r_p\rho_p C_{p_p}} - \frac{T_p}{C_{p_p}}\cdot\frac{dC_{p_p}}{dt} - \frac{3\cdot\left(\frac{\Delta H_V}{W_V} - C_{p_p}T_p\right)\frac{W_V\alpha_M p_{ref}\exp\left[-\frac{\Delta H_V}{R}\left(\frac{1}{T_p}-\frac{1}{T_{ref}}\right)\right]}{R_p T_p}\left(\frac{R_m T_p}{2W_V}\right)^{0.5}}{r_p\rho_p C_{p_p}}$$

Equation (10)

With the Equation (9) and (10), the nanoparticles temperature-time relation has been established, using a fourth order Runge-Kutta algorithm. The corresponding signal intensity change with the time using this relation could be calculated according to Planck's law[271, 272], as

$$S_{LII} \propto \pi r_p^2 \frac{4\pi r_p E(m)}{\lambda_{\det}} \frac{2\pi hc^2}{\lambda_{\det}^5} \times \left(\frac{1}{e^{hc/\lambda_{\det}k_B T_p} - 1} - \frac{1}{e^{hc/\lambda_{\det}k_B T_g} - 1} \right)$$

where $\lambda_{\det}$ signifies the detection wavelength (492nm&694nm in this study). As $E(m) = \frac{\lambda_{filter}}{8\pi r_p}$, where λ_{flitre} is the effective band for filter (for the filters used in this study, FWHM=10nm), we have the final equation

$$S_{LII} \propto \frac{r_p^2 \lambda_{filter}}{\lambda_{\det}^6} \times \left(\frac{1}{e^{hc/\lambda_{\det}k_B T_p} - 1} - \frac{1}{e^{hc/\lambda_{\det}k_B T_g} - 1} \right)$$

Equation (11)

Based on the Equation (9) (10) and (11), the LII heat transfer model has been established in this study. All the involved symbols and their related unities could be found in the Acronyms and Symbols part at the beginning of this thesis. But there are still factors in Equation (10) like C_{p_p}, ρ_p, α_T, ΔH_V, W_V, α_M, p_{ref}, T_{ref} need to be mentioned, which are related to the nanoparticle nature. To determine proper values of these factors, a TEM grid has been put in a holder and quickly sent to the center of the reactor, then removed after 1min to collect the nanoparticles during the experiments. These samples were used for further HRTEM and EDS (HAADF mode) diagnostic. The examples for their results are shown in Fig.2-9. The experiment conditions used were as follows: 650 °C furnace temperature, 1L/min argon, ferrocene/xylene solution 0.05g/mL with 0.2mL/min solution injection speed. The 0.05g/mL solution concentration was the maximum concentration used in this study.

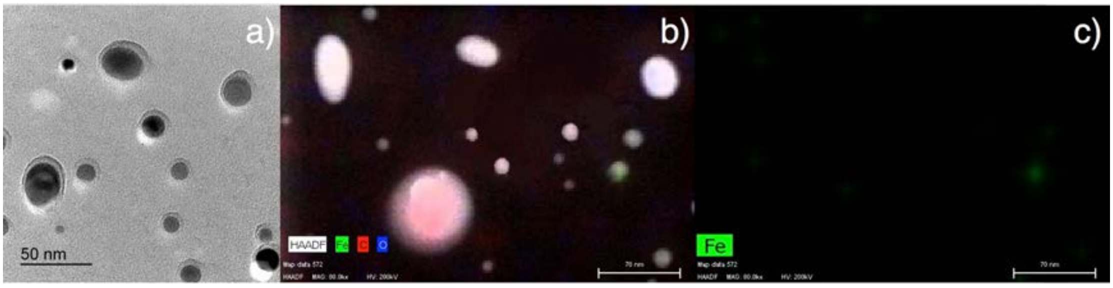

Fig.2-9 *The (a) HRTEM and (b) (c) HAADF images for the nanoparticles*

Comparing the Fig.2-9 (b) and (c), the HAADF results show that in the nanoparticles, the percent of Fe is relatively low, even the concentration of the ferrocene/xylene is already 0.05g/ml, not much iron element could be seen in Fig.2-9 (c) and the most part of the nanoparticles are consisted mainly by carbon. What's more, according to the simulation results based on factors used by other studies[262, 267], the ratio of the maximum signal intensity between the carbon and the iron nanoparticles is approximate to 2 when the NPs size is 10~20nm. As in the 0.05g/ml ferrocene/xylene solution, the ratio between carbon/iron mass is more than 50, thus the ratio between carbon/ iron volume is ~170. This calculation means in this study, the carbon in the nanoparticles has a much more important influence on the LII signal intensity, therefor the related factors that have been mentioned above are firstly determined based on a carbon nanoparticle model, where α_T is supposed to be 1 to simplify the calculation (as this factor is tightly related to the heat capacity and density of NPs during the calculation and not independent, usually it needs to use other known conditions to deduce its exact value). So we have the function and values below based on the previous studies results of others[268, 273]:

$$
\begin{aligned}
C_{p_p}(Unite: J\cdot g^{-1}\cdot K^{-1}) = {} & 2.253740888 + 3.812163736\times10^{-5}T - 377.70014T^{-1} \\
& -181791.8712T^{-2} + 6.66548856\times10^{7}T^{-3} \\
& -6.01190592\times10^{9}T^{-4}
\end{aligned}
$$

$$
\Delta H_V = 7.78\times10^5\,\mathrm{J\cdot mol^{-1}}, W_V = 36\mathrm{g\cdot mol^{-1}}, \alpha_M = 1,
$$

$$
p_{ref} = 1\mathrm{atm}, T_{ref} = 3915\mathrm{K}
$$

According to Fig.2-9 (a), it could be found that it exists difference of brightness for the nanoparticles. Based on this fact, it is assumed that the nanoparticles are formed in a relatively loose way which induces a low density, thus the LII signal and HRTEM results should be compared to determine its density. Three different cases have been conducted, in which the nanoparticle samples have been collected for the TEM diagnostic, in order to make the calibration of the established model. The experiment conditions for these three cases are as follows: Case 1 Reactor temperature 650°C, 1L/min argon, pure xylene with 0.2mL/min solution injection speed, samples collected at the reactor center after 8min of the xylene injection; Case 2 Reactor temperature 650°C, 1L/min argon, ferrocene/xylene solution 0.05g/mL with 0.2mL/min solution injection speed, samples collected at the reactor center after 8min of the solution injection; Case 3 Reactor temperature 650°C, 1L/min argon, ferrocene/xylene solution 0.05g/mL with 0.2mL/min solution injection speed, samples collected at the reactor center after 3min of the solution injection. For case 1, based on the HRTEM results, its Sauter mean diameter has been calculated (discussed in Annexes), using the function $D_{p_{Sauter}} = \frac{\sum D_p^3}{\sum D_p^2}$, and we have $D_{p_{Sauter}}$ =13.3nm. Using this diameter, the nanoparticle density has been found as $\rho_p = 1.23 g\cdot cm^{-3}$. After this calculation, the calculated density has been used to find if it fits the results of the cases 2&3, in which the Sauter mean diameters of the nanoparticles equal to 18.6nm and 14.0nm respectively, the comparison of the real LII curves and model based simulation results are shown in Fig.2-10. It could be found that the hypothetical nanoparticle density has fitted the HRTEM measurement quite well, so its rationality is confirmed and this nanoparticle density value can be used for the following in-situ research. So far, all the necessary factors on the LII simulation model have been well determined except the factors that are related to the gas composition.

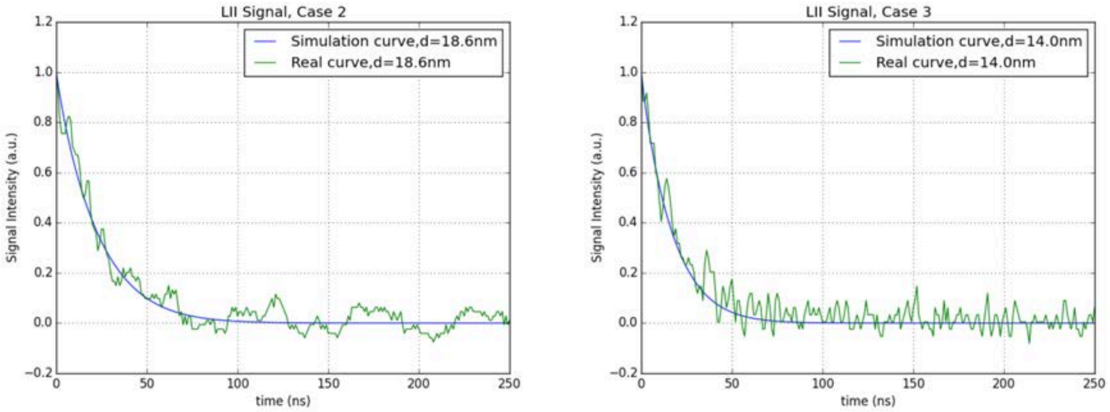

Fig.2-10 *Comparison of the real LII curves and simulation ones*

2.3.2 Mass Spectrometry

As has been just mentioned, the gas composition variation is a very important factor in this study. It not only influences the m_g and γ in the LII model, but also influences the property of synthesis product. To track the gas composition variation during the experiments, a mass spectrometer (Pfeiffer Vacuum Thermostar GSD 301 T3) was applied, which includes a quadrupole analyzer, a Faraday and a channeltron sensor. The exhaust gas of the reactor was captured by a capillary injected in the reactor, then entered the test machine after passing through a heater ~200°C. All the system was well sealed to avoid the possible interference of air. For a typical experiment in this study, the main gas compositions are acetylene, argon, hydrogen, xylene, ferrocene and their related reaction products, which will be discussed in detail in chapter 4. These mentioned components are paid close attention to study the gas composition evolution under different experiment conditions.

2.4 Conclusion

In this chapter, the experimental procedure, including the FCCVD system and in-situ/ex-situ characterization methods used in this study has been presented. It could be found that the LII technique could be very useful to achieve a no interference, real-time diagnostic for the NPs size/quantity evolution determination. The Table 2-4 below presents a summary for the mentioned characterization methods used in this study.

Table 2-3 *Summary of the characterization methods used in this study*

Techniques	**Measured factors**	**Comments**
Optical Microscopy	Size of the droplet after the atomization of injected solution	Ex-situ
SEM	CNTs morphology, including their length and diameter	Ex-situ
TEM	NPs size and component, CNTs inner/outer diameter,	Ex-situ
Raman	CNTs crystallization	Ex-situ
TGA/DTG	CNTs crystallization, Ratio of amorphous in the product	Ex-situ
Thermocouple	Reactor temperature profile	In-situ
LII	Suspended NPs size during the experiment	In-situ
MS	Gas composition during the reaction	In-situ

Chapter Ⅲ Evolution of nanoparticles during the synthesis

The CNTs synthesis process is complex which involves many factors like temperature, time, precursor type/quantity, substrate and etc. To study CNTs growth mechanism, it should examine the whole FCCVD synthesis process from the very beginning. In this chapter, the research about the droplet atomization process has been studied, then following by the research of the nanoparticles spatial-temporal evolution. These two stages are the early stages for the CNTs synthesis, in which the precursors decompose and nanoparticles form. The influences of temperature, solution injection speed/ concentration, gas flow rate/composition, diagnostic position as well as time have been compared separately or by Taguchi method to find their relations with the droplets and NPs size. Based on these results, a possible nanoparticles formation mechanism and the NPs relation with the CNTs are discussed.

3.1 Droplet size research: the atomization of solution

During the CVD process, the solution that contains ferrocene and xylene has been injected the reactor through a spray system. Thanks to this system the atomization of the solution was achieved and small droplets were formed, which acted as the very first CNTs precursors to participate and influence the following reaction[274]. Except the gas flow which was always kept at 1L/min during CNTs synthesis in this study, there are three factors that might have influences on the droplet size: the preheat temperature, solution concentration and liquid injection speed (in this stage it is supposed that no chemical reaction occurs, thus the gas composition will not lead to any difference on the droplet size). To study the influences of these factors, certain experiments have been designed and their related conditions are shown in Table 3-1 below. These experiments have been divided into three groups, which correspond the three factors preheat temperature (Experiment 1, 2, 3 for room temperature, 150°C and 250°C), concentration (Experiment 1, 4, 5 for 0.01, 0.03 and 0.05g/mL) and liquid injection speed (Experiment 6, 1, 7 for 0.1, 0.2 and 0.3 mL/min), to ensure that each factor has three different levels to be compared.

Table 3-1 *Experiment conditions for the droplet size research*

Experiment Number	**Preheat temperature (°C)**	**Concentration (g/mL)**	**Solution Injection Speed (mL/min)**
1	Room temperature	0.01	0.2
2	150	0.01	0.2
3	250	0.01	0.2
4	Room temperature	0.03	0.2
5	Room temperature	0.05	0.2
6	Room temperature	0.01	0.1
7	Room temperature	0.01	0.3

During these experiments, the droplets samples were collected at 10cm after the nozzle of spray by a pre-placed small quartz plate, then sent for further optical microscope observation right after the sample collection, to minimize the possible perturbation caused by solution evaporation. The statistical results for the droplets size distribution are shown in Fig. 3-1. For the preheat temperature, the augmentation of temperature will lead to the decrease of the droplet size, as the average droplets diameter has decreased from 0.48μm (under room temperature) to 0.42 μm (under 250°C). For the liquid injection speed, its decrease results in obvious difference, as the average diameter has decreased from 0.54 μm (0.3 mL/min) to 0.44 μm (0.1 mL/min), and the droplet size distribution becomes narrower with a lower solution injection speed. However, the change in concentration doesn't induce any difference, the droplet size always keeps at 0.47~0.48μm and the corresponding distributions are quite similar.

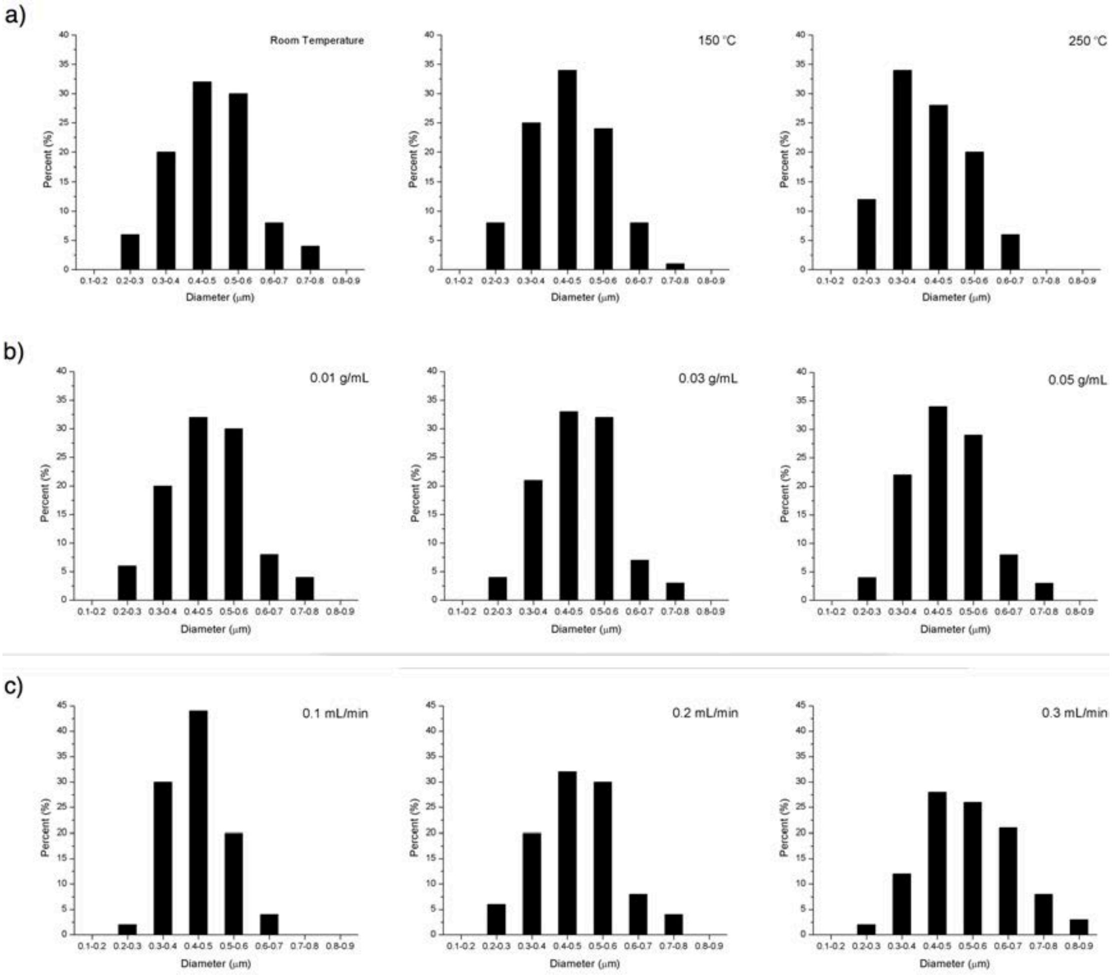

Fig. 3-1 *Droplet size distribution with varied (a) preheat temperatures (b) concentrations and (c) liquid injection speeds*

In fact, for the droplets atomization process, there exist three different forms for their fragmentation[275]: capillary fragmentation, mechanical fragmentation and thermal fragmentation, in which the first one is directly related to the nozzle inner diameter of the spray, while the last two are determined by the energy transfer from the outside to the droplets. The preheat treatment, as well as the liquid decreasing approach (by reducing the liquid injection speed) make the droplets getting more energy from mechanical and thermal way, thus promote the formation of smaller droplets. These droplets will then enter the furnace part of the reactor acting as the precursor for the following CNTs synthesis processes, in which they experience the chemical reactions and release decomposition products for the next step nanoparticle formation.

3.2 Nanoparticles in the gas phase: Size-control approaches

Between the droplets and the final CNTs products, there is a transition period that includes many chemical and physical changes. During this period the nanoparticles are found spreading all over the gas atmosphere, which will deposit later on the substrate, as TEM photos reveal that they are always found at the end of the CNTs or encapsulated in the CNTs (see Fig. 3-9 at the end of this chapter). The EDS results mentioned in chapter 2 reveals that the main composition for these nanoparticles is carbon, while iron is also included in a much lower contents. According to others' study[276, 277], the size-control of nanoparticles is a key parameter to satisfy the demand of specific types CNTs large-scale production. Based on this fact, the study on the NPs formation and their size-control approaches is very important for the CNTs synthesis research.

For the formation of these nanoparticles, it may include various processes from the droplets evaporation at the very beginning to the final coagulation or sintering. In the research of Kikuo Okuyama and I. Wuled Lenggoro, two forms of particles may occur right after the solvent evaporation. These forms vary according to the ratio diversity of solvent evaporation/solute diffusion characteristic time. Hollow porous particles appear if this ratio is approach to 1, while particles with shell occur if this ratio is approach to 0 [278]. In the research of K. Nakaso et al, the clusters are formed by the chemical reaction, condensation and evaporation. Then nanoparticles are formed due to the clusters' agglomeration [279]. For these proposed mechanisms, the main difference is whether the evaporation residue of one droplet forms one nanoparticle (one to one model based on the research of Kikuo Okuyama and I.

Wuled Lenggoro), or the droplets crush to many small pieces and then agglomerate to multi nanoparticles (one to many model based on the research of K. Nakaso et al). In order to find which mechanism is more suitable for the nanoparticles formation in this study, a study on the factors that may influence the nanoparticles is necessary. However, as the number of the possible influence factors is large (as has been mentioned at the beginning of this chapter), the isolation for these factors is preferred to avoid the possible mutual interference between them.

3.2.1 Time influence

After the first droplet entering the reactor, the volume density of carbon/catalyst sources increase till a dynamic balance is set up. Based on this fact, it reasonable to study the nanoparticles evolution with the time primarily, to make sure that the following tests will not be perturbed by the neglect of diagnostic moment. Using the in-situ LII technique, an experiment was designed to achieve this goal with the following conditions: Reactor temperature 650°C, 1L/min argon, ferrocene/xylene solution 0.01g/mL with 0.2mL/min solution injection speed.

Two values were studied in this experiment: the maximum LII signal intensity (when the nanoparticle reaches its maximum temperature due to the laser pulse) and its decay time (the time when the LII signal intensity decrease to 20% of its maximum value). As the general CNTs synthesis duration is 10min in this study, the LII signal evolutions with time during 15 min were recorded and shown in Fig. 3-2. Based on the Fig. 3-2 results, it could be found that for the LII signal, both its maximum value and its decay time have kept increasing during this 15 min process, and no dynamic balance has been set up yet at the end of 15min. As has been mentioned in chapter 2, these two values have their relation with the particle volume fraction and size. The augmentation of these values means that both the nanoparticle volume density and their size have augmented as time goes on. This finding is in accordance with the former experiments results, where the TEM samples are collected at 3min and 8min separately (experiment conditions: reactor temperature 650°C, 1L/min argon, ferrocene/xylene solution 0.05g/mL and 0.2mL/min solution injection speed), as in the former experiments the Sauter mean diameter of the nanoparticles collected at 8min is 18.6nm, which is 4.6nm larger than that collected at 3min, and the augmentation of NPs volume density is also obvious according to the TEM photo (shown in Fig 3-3). Thus in the following research, the LII signal data are only collected between 8~10 min after the launch of the liquid injection, then used for further analysis to avoid the time influence on the results.

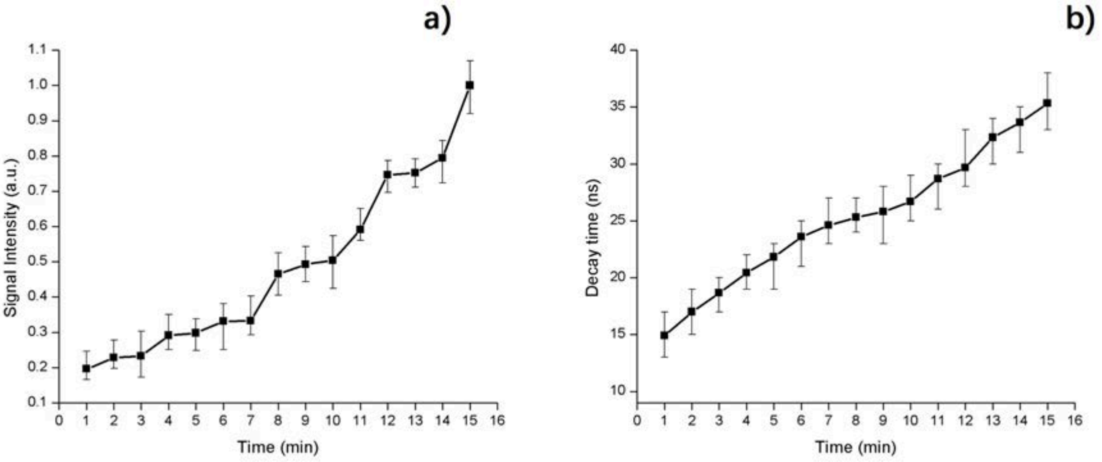

Fig. 3-2 *The LII signal (a) intensity (a.u.) and (b) decay time evolution with time*

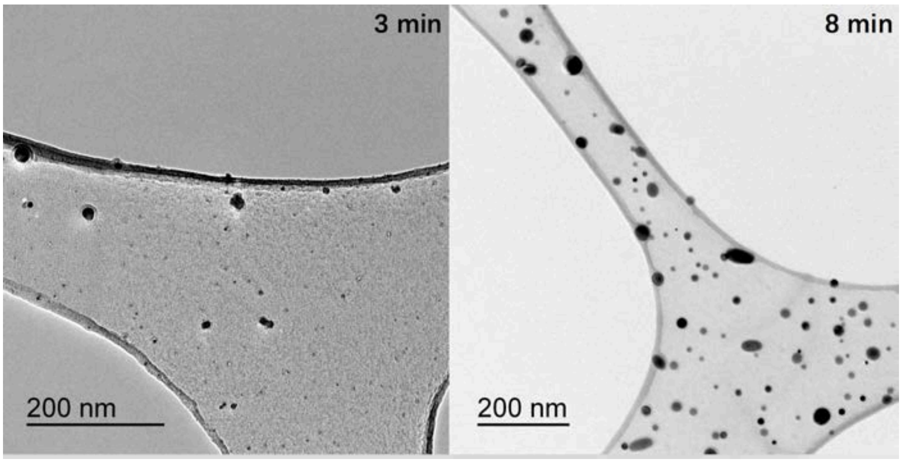

Fig. 3-3 *Example TEM photo for the samples collected at 3min and 8min under the same experiment conditions*

3.2.2 Position influence

In order to get more information about the nanoparticles evolution, NPs size at different positions along the reactor was examined in this study. The experiment was conducted under 650°C, in which 0.01g/mL ferrocene/xylene solution was used with an injection speed 0.2mL/min, and the gas flow for argon, hydrogen and acetylene were 0.78L/min, 0.2L/min and 0.02L/min respectively. 5 positions A, B, C, D and E were chosen for the LII diagnostic, which is shown in the Fig. 3-4 below.

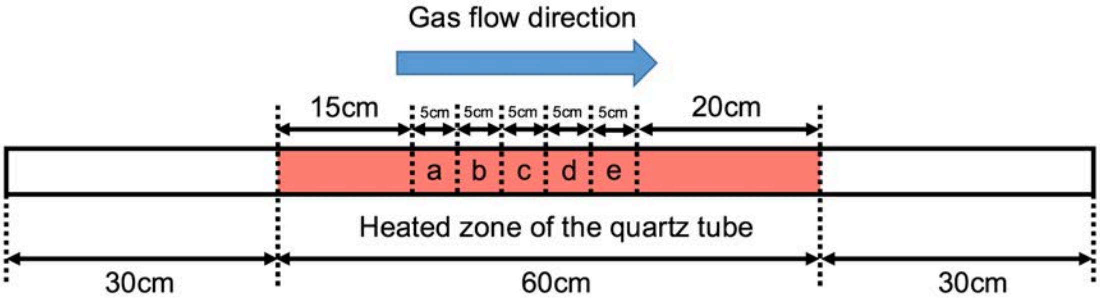

Fig. 3-4 *Schematic of the LII signal diagnostic positions at the reactor*

During the experiment process, both the maximum intensity and decay time of the LII signals were recorded in-situ to analyze the NPs evolution. In order to find the possible relation between these NPs information with the CNTs properties, the CNTs samples on the alumina substrate at the corresponding positions are also collected for their diameter measurement. All experiments results are shown in Table 3-2.

Table 3-2 *Results for the position dependent LII maximum intensity/ NPs size and the corresponding CNTs*

Position	**Decay time (ns)**	**Maximum intensity (a.u.)**	**NPs diameter (nm)**	**CNTs diameter (nm)**	**CNTs length (µm)**

A	44.3	1	24.4	14.0	32.9
B	30.1	0.78313253	16.6	13.5	30.6
C	25.6	0.645783133	14.1	12.8	28.1
D	24.2	0.609638554	13.3	12.3	25.4
E	23.8	0.537349398	13.1	12.1	23.9

Based on Table 3-2 results, it could be found that the nanoparticles volume density decreases along the gas flow direction. This evolution fits the CNTs production distribution along the reactor[58], which suggests that at the front part of the reactor there are more carbon/catalyst sources for the CNTs growth. The CNTs length evolution also supports this point of view, as the short of carbon source supply will certainly induce a relatively low CNTs growth rate. For the NPs size, it decreases along the gas flow direction either. Especially at the position A and B, the NPs diameter has experienced a sudden drop from 24.4nm to 16.6nm. After the position B, the NPs diameter variation becomes relatively gentle, as the NPs diameter difference from B to E is 3.5nm only. However, the CNTs diameter variation between position A (14.0nm) and B (13.5nm) is only 0.5nm, much less than the NPs diameter difference between these two positions. There are two possible reasons for this difference. Firstly, considering the LII signal maximum intensity evolution behavior, it suggests that there are many nanoparticles at the beginning, which have been largely consumed at the front part of the reactor tube, as the maximum density decreases sharply at the A, B and C positions. So for the nanoparticles at the position A, their relatively high volume density enhances the collision opportunity between them, which induces the nanoparticles aggregation and the formation of bigger nanoparticles. Secondly, this difference also suggests that there may exist other following processes on the substrate, the nanoparticles in the gas are not the final form, thus only the NPs size in gas phase can’t determine the final CNTs diameter. The product difference induced by substrate diversity will be discussed later in chapter 5. The evolution for the factors mentioned in this section are shown in Fig. 3-5

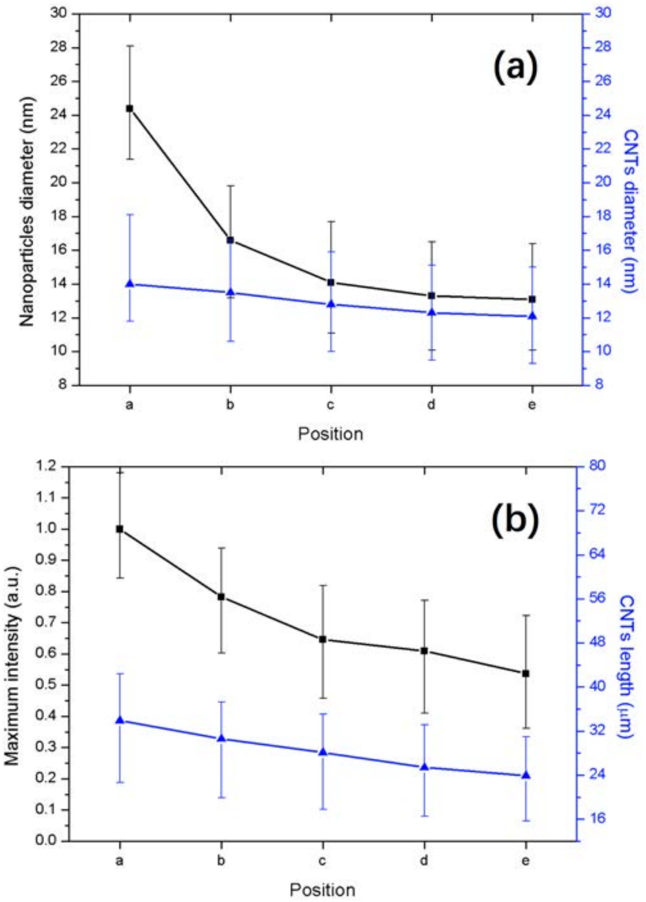

Fig. 3-5 The evolution of (a) NPs/CNTs diameter and (b) LII maximum intensity/CNTs length

3.2.3 Temperature influence

Temperature is a very important factor to the NPs size during the CNTs synthesis process. In this section, the temperature influence must be considered. In this section, three reactor temperatures have been used: 650°C, 750°C and 850°C, with 1L/min argon, ferrocene/xylene solution 0.01g/mL and 0.2mL/min solution injection speed. LII signals were recorded for the decay time calculation, which are 25.3ns, 31.3ns and 43.3ns respectively.

As the chemical reactions change their reaction rates at different temperatures, the gas composition varies according to experiment conditions, as well as their heat capacity (discussed in Annexes A2.2). Before the calculation of the NPs diameter in these experiments, the m_g and γ in the LII model need to be adjusted in different cases first. For this purpose, MS diagnostic was used to determine the gas composition concentration. Based on its results, five main gas compositions were considered in this study: argon (Ar), xylene (C_8H_{10}), toluene (C_7H_8), benzene (C_6H_6) and methane (CH_4). Their relative concentrations and the corresponding m_g and γ are presented in Table 3-3.

Table 3-3 *Gas composition concentration, average gas molecular weight and heat capacity ratio at different temperatures*

Temperature (°C)		**650**	**750**	**850**
Gas composition concentration (normalized by the argon flow rate)	Ar	1.00E+00	1.00E+00	1.00E+00
	C_8H_{10}	3.06E-02	8.14E-03	1.30E-03
	C_7H_8	4.73E-04	7.25E-04	7.25E-04
	C_6H_6	5.06E-04	5.06E-04	2.39E-03
	CH_4	8.94E-04	3.74E-03	1.08E-02
Gas molecular weight m_g (g/mol)		42.28	40.48	40.03
Heat capacity ratio γ		1.27	1.31	1.28

By the data presented in Table 3-3, the NPs average diameters and the corresponding value ranges have been determined, which are 13.6nm (10.5~16.7nm) at 650°C, 14.2nm (11.2~17.6nm) at 750°C and 18.7nm (15.7~22.2nm) at 850°C. The NPs size increases with the reactor temperature augmentation, especially when the temperature increase from 750°C to 850°C. As the MS results of the gas composition show that the precursor decomposition has been highly improved due to the rise of temperature, it suggests that more decomposition products have been generated to participate in the nanoparticles formation (see also chapter 4). What's more, the high temperature favors the molecular movement in the gas, which arise their collision opportunity. Because of the reasons mentioned above, nanoparticles with bigger size are formed with the rise of temperature.

3.2.4 Solution injection speed/ Gas flow rate influences

According to the droplet research in section 3.1, it could be found that the liquid injection speed has an influence on the droplet size, so it's reasonable to study if the injection speed change will also influence the NPs size. Two experiments have been done on this purpose, in which the experiment conditions are as follows: reactor temperature 650°C, 1L/min argon, xylene with 0.1 (Experiment A) or 0.2mL/min (Experiment B) solution injection speed. The LII signals during these experiments are compared, which show that the decay time under the 0.1mL/min & 0.2mL/min injection speed are 22ns and 24.6ns, corresponding to 10.6nm and 13.3 nm NPs diameter. This result and the droplet size study results suggest that the increase of injection speed contributes to both droplet and NPs size augmentation at the same time, so these two sizes may be related. There are two possible reasons for the NPs size increase with the solution injection speed augmentation. Firstly it may be explained by the one to one NPs formation model, bigger droplets produced by higher solution injection speed will form bigger NPs. Secondly, based on the time dependent decay time evolution results, the increase of precursor quantity leads to an augmentation of NPs size, and the augmentation of solution injection speed is just one method to increase the precursor quantity directly.

To avoid the influence caused by precursor quantity change, another experiment (Experiment C) has been designed. This experiment shares all the experiment conditions of Experiment B except that its argon gas flow has been increased from 1L/min to 1.5L/min. In this experiment, NPs size has been found decreased from 13.3nm to 12.4nm. It means that for the same carbon source quantity, the increase of gas flow rate will lead to the size decrease of both droplet and nanoparticle. So the one to one nanoparticle formation model has been confirmed again to some extent, as the sizes of droplet and nanoparticle have same change tendency with the liquid injection speed and gas flow rate variation. But there exists still another possible explanation: the augmentation of gas flow has decreased the nanoparticles residue time in the reactor thus led to a reduction of the NPs volume density, so the collision chance of the precursor decomposition products has been limited, which is not favorable for the large size nanoparticles formation.

Table 3-4 *Experiment conditions and NPs size for the study of injection speed/gas flow rate influences*

Experiment	**Liquid injection speed (mL/min)**	**Gas flow rate (L/min)**	**NPs size (nm)**
A	0.1	1	10.6 (7.9~13.1)
B	0.2	1	13.3 (10.3~16.2)
C	0.2	1.5	12.4 (9.5~15.1)
General conditions:	Reactor temperature 650°C, Argon as carrier gas, Xylene injected into the system		

3.2.5 Concentration influence

According to the TEM results mentioned in chapter 2, it could be figured out that with the variation of ferrocene/xylene solution concentration (from 0g/mL to 0.05g/mL), the nanoparticles Sauter mean diameter changes from 13.3nm to 18.6nm for the samples collected at 8min. This variation confirms the solution concentration influence on the NPs size. In order to evaluate this influence, a series of the experiments have been conducted with the following experiment conditions: reactor temperature 650°C, 1L/min argon, 0.2mL/min solution injection speed, 0.0/0.01/0.03/0.05 g/mL solution concentration.

Based on the LII results, the NPs diameters are 13.3nm, 13.6nm, 16.9nm and 18.6nm respectively, corresponding to the 0.0/0.01/0.03/0.05 g/mL solution concentration. They increase with the augmentation of the solution concentration. Moreover, if the solution concentration- NPs diameter curve is drawn, it appears that there is a linear relation between them, with R^2=0.95371, which is shown in Fig. 3-6. This behavior is quite different with the case for droplets size, as droplets size distribution keeps nearly identical under different solution concentration. The one to one NPs formation model might explain this solution concentration dependence of the NPs size. Supposing that the Fe amount will not change during the NPs formation process, the augmentation of solution concentration will induce the iron quantity rise for each nanoparticle, thus finally increases the NPs volume. But there is still a problem, as the iron quantity is relatively low compared with the carbon (the Fe/C mass ratio is less than 0.02 when the solution concentration is 0.05g/min), how could the iron still play an important role in the determination of the NPs size while the most part of the NPs are composed with carbon (see section 2.3.1)? So further study needs to be done, to find the possible explanation for this phenomenon.

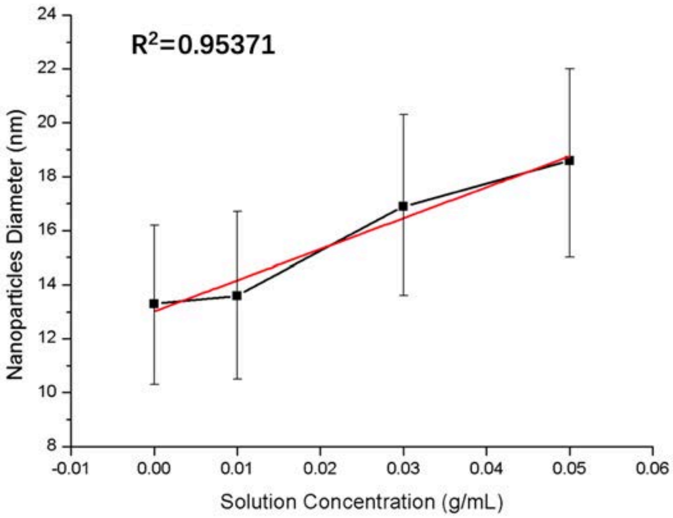

Fig. 3-6 *Relation between solution concentration and NPs diameter*

3.2.6 Taguchi method for the other factors

In the former sections, the nanoparticles evolution with time, temperature, injection speed/gas flow rate, concentration as well as position have been discussed. But there are still three factors which haven't been mentioned in section 3.2, they are preheat, acetylene and hydrogen flow rate. In order to evaluate their influences, a Taguchi robust design method was applied, by which multifactor could be compared in an efficient way[280]. Three factors with two levels were examined in this design, their experiment conditions, as well as the NPs sizes calculated according to the LII signals are presented in Table 3-5.

Table 3-5 *Taguchi parameter design and results of the CVD experiments*

Experiment	**Preheat**	**Hydrogen (L/min)**	**Acetylene (L/min)**	**NPs diameter (nm)**
A	RT*	0.1	0	17.0
B	RT*	0.2	0.01	16.7
C	250°C	0.1	0.01	15.1
D	250°C	0.2	0	14.9
General experiment condition	Reactor temperature 650°C, 0.03g/ml ferrocene/xylene solution with 0.2mL/min injection speed, 1L/min total gas flow (argon+ hydrogen+ acetylene)			

* RT means room temperature

To analyze these results, two values need to be calculate, the larger-is-better response (S/N) $_{\text{larger}}$ and the smaller-is-better response (S/N) $_{\text{smaller}}$, their equations are as follows:

$$S/N_{\text{larger}} = -10\log_{10}\left(\frac{1}{n}\sum\frac{1}{Y_i^2}\right)$$

$$S/N_{\text{smaller}} = -10\log_{10}\left(\frac{1}{n}\sum Y_i^2\right)$$

In these equations, the n is the levels of the factor, and the Y_i is the corresponding result. For example, the preheat temperature is one of the three factors (the other two are hydrogen and acetylene flow rate) in this Taguchi method, which has two levels (Room temperature and 250°C). To calculate the $(S/N)_{larger}$ and $(S/N)_{smaller}$ for preheat room temperature, the Y_i in the equation should be the NPs diameter results in experiments A and B. The results for the $(S/N)_{larger}$ and $(S/N)_{smaller}$ and their graph are shown in Table 3-6 and Fig. 3-7 respectively. According to these results, it could be concluded that all the three factors (preheat temperature, hydrogen and acetylene flow rate) have influences on the NPs size. However, compared with the S/N ratio differences caused by preheat temperature variation, both hydrogen and acetylene flow rate only have second-rate influences on the NPs size. The largest NPs diameter could be achieved under no preheat, no acetylene flow and 0.1L/min hydrogen flow rate conditions, while the smallest NPs diameter could be achieved under 250°C preheat, 0.01L/min acetylene and 0.2L/min hydrogen flow rate respectively.

Table 3-6 *The* $(S/N)_{larger}$ *and* $(S/N)_{Smaller}$ *results of the NPs diameter in the Taguchi method*

	Preheat		**Hydrogen (L/min)**		**Acetylene (L/min)**	
	RT*	**250°C**	**0.1**	**0.2**	**0.00**	**0.01**
$(S/N)_{larger}$	24.531	23.521	24.064	23.931	23.999	23.995
$(S/N)_{smaller}$	-24.532	-23.522	-24.125	-23.987	-24.074	-24.039

* RT means room temperature

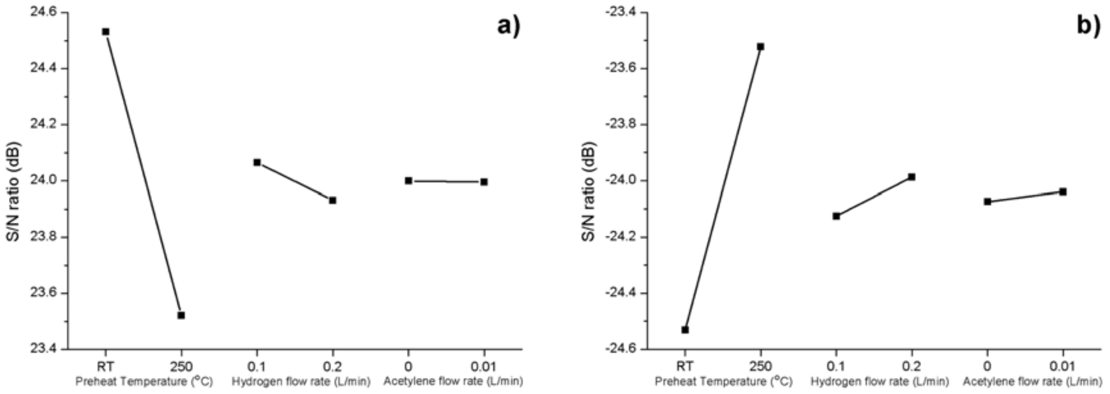

Fig. 3-7 *Response graph of S/N ratio for (a) larger-is-better and (b) smaller-is-better analysis of the NPs diameters*

For the preheat temperature factor, based on the Taguchi method result, it has the same influence tendency on both droplets size and NPs size. When it is augmented, smaller droplet and NPs will be obtained. This behavior strongly supports the one to one model for the NPs formation, as in this model, when smaller droplets form, their relatively less carbon/catalyst contain will limit their final NPs volume. For the factors hydrogen and acetylene, during the NPs formation stage they only have second-rate influences on the NPs size if compared with the preheat factor. The increase of their flow rate will limit the augmentation of NPs size, which is in good accordance with their influence behavior on the final CNTs diameter (see chapter 5). Unlike preheat which mainly causes droplet size variation, the gas composition has continuous influence during the synthesis process, from the NPs formation to the final CNTs growth.

In order to study the relation between NPs size and the CNTs diameter relation, the CNTs samples in experiment A, B, C, D have been collected to measure their diameters. The diagnostic results show that they are 18.9nm, 15.3nm, 17.6nm and 16.4nm respectively. The comparison of the NPs/CNTs diameter in the experiments designed by Taguchi method are shown in Fig. 3-8

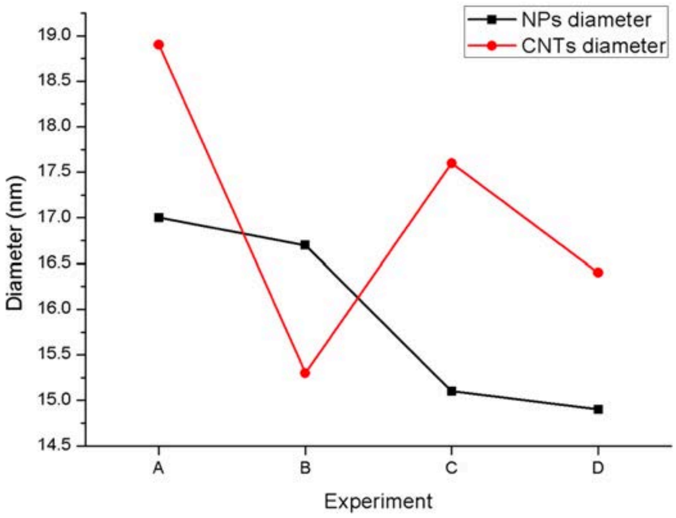

Fig. 3-8 *Comparison of the NPs/CNTs diameter in the experiments designed by Taguchi method*

According to the comparison results shown above, it could be found that the preheat temperature difference has led to a ~ 2nm gap between the NPs diameters of AB and CD. Under the same preheat temperature, the NPs and CNTs diameters have same evolution tendencies, which suggests the possible relation between NPs and CNTs. However, the comparison in Fig. 3-8 also proves that the NPs diameter could be either greater or less that the CNTs diameter. If comparing the CNTs synthesis process, it could be found that the experiment conditions are very close for A and C, B and D respectively, that explains why the CNTs diameter for A and C, B and D are relatively similar. So for CNTs diameter, it’s the gas composition rather than preheat which can influence its value, even the gas composition only has a second-rate influence for the NPs size determination. The phenomenon implies that there must be other changes occurring in the following synthesis process

3.3 Conclusion

In this chapter the studies on the droplets as well as nanoparticles have been discussed. For the droplets size, under a constant gas flow rate 1L/min during the CNTs synthesis, effective adjustment could be achieved by directly changing the preheat temperature and solution injection speed, while the change of solution concentration doesn't show any obvious influence. The essence of the adjustment is an energy transfer process in mechanical and thermal way. Smaller droplets could be obtained by decreasing the solution injection speed or increase the preheat temperature.

For the NPs size control approaches, the NPs volume density and their sizes are firstly dependent on the diagnostic time/position. At the beginning of the CNTs synthesis, both the nanoparticle volume density and their sizes will increase as time goes on, mainly due to the carbon/catalyst source augmentation in the reaction system. These nanoparticles will be consumed for the CNTs growth, so their quantity will decrease along with the gas flow direction. When the time and position are fixed, under a constant 1L/min gas flow, preheat/reactor temperature, solution injection speed, concentration as well as gas composition, all these factors have effects on the NPs size. Compared with the droplets formation process, the NPs formation involves much more factors, and the factor concentration that has no influence on droplets size distribution plays an important role for the NPs size determination. Low preheat temperature, high reactor temperature, high concentration solution with high solution injection speed and low hydrogen/acetylene flow rate will favor the formation of larger NPs, while the smaller NPs will be achieved by the opposite conditions. When comparing the NPs diameter during the experiments studied, the reactor temperature and solution concentration variation have caused the biggest differences for the NPs diameter, which are 5.1nm (when the reactor temperature rise from 650°C to 850°C) and 5.3nm (when the concentration rise from 0g/mL to 0.05g/mL) respectively. For the other factors, the NPs diameter difference is about 2~3nm. The results suggest that the adjustment of reactor temperature and solution concentration is the most effective way for the NPs size control under the experiment conditions used in this study. However, to achieve an accurate control on the NPs size, all the factors need to be considered for the optimum performance.

For the relation between the NPs and CNTs diameters, it has been proved that if under constant preheat temperature, they will have the same evolution tendency. It suggests the NPs have relation with the CNTs. But the CNTs synthesis process after the NPs deposition will keep influencing the CNTs, and the final product properties may differ with the same gas phase NPs size distribution. For example, the substrate has an important influence on the CNTs diameter. According the TEM results, the CNTs samples in section 3.2.2 collected at the B and C positions have an average diameter 13.2 nm on alumina, while the average diameter will be augmented to 19.9 nm when the CNTs grow on quartz (see chapter 5). As the substrate has no influence on the gas phase nanoparticles, these two types CNTs share the same NPs size distribution. The TEM photo for the CNTs grown on quartz and on alumina with the encapsulated nanoparticles are shown in Fig. 3-9, it could be observed that the nanoparticles have been transformed during the CNTs growth.

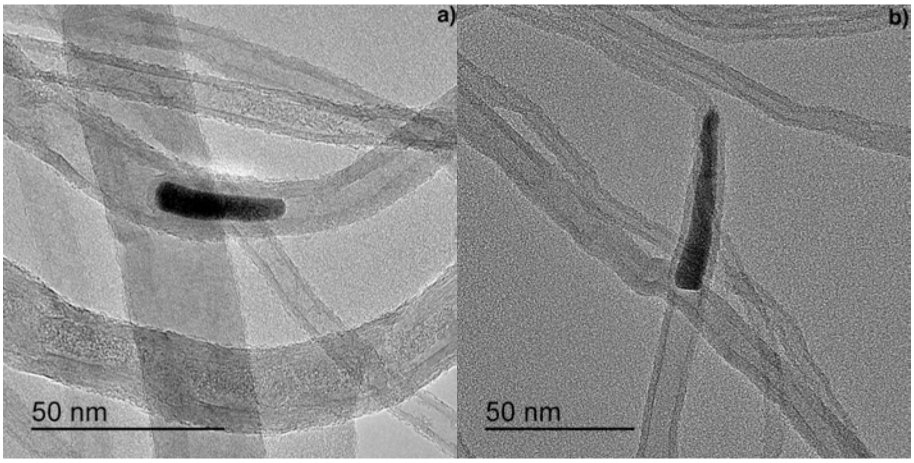

Fig.3-9 *Examples for CNTs grown on (a) quartz and on (b) alumina with the encapsulated NPs*

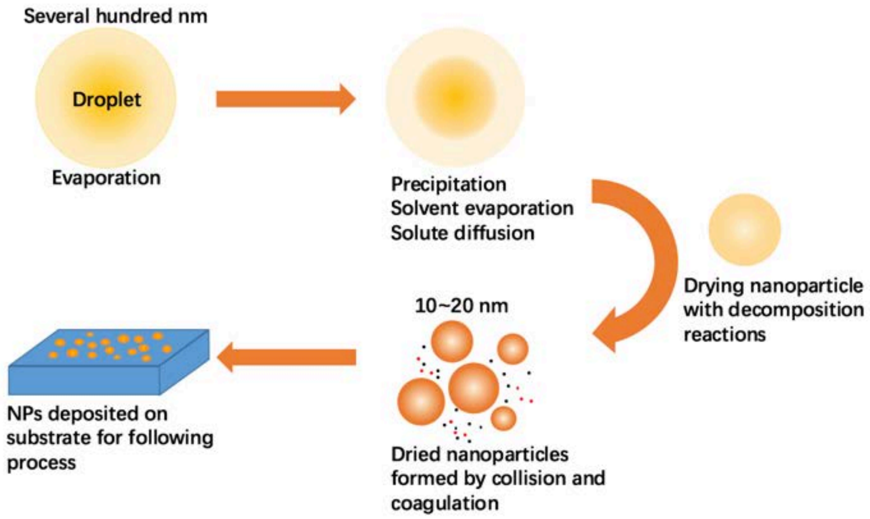

Fig. 3-10 *Nanoparticle formation process in floating CVD, with the red and black points representing the possible iron and carbon atoms around the NPs respectively.*

According to the study results of the preheat/reactor temperature, solution concentration/injection speed as well as gas flow rate influences on the droplets and nanoparticles, it strongly suggests that the droplets and nanoparticles are closely related. Besides the NPs sizes augmentation led by reactor temperature rise, the one to one NPs formation model is able to explain all the NPs size change phenomena. Based on this fact, the NPs evolution process is described as the procedure shown in Fig. 3-10: When the droplets form, their sizes are keeping decreased by the solvent evaporation. The solute diffuses at the same time, and the precipitation process begins. Generally, the carbon and iron elements released by decomposition reactions begin to form the nanoparticles, along with the collision and coagulation. After that the final form nanoparticles are generated, which will be deposited on the substrate for the following process. It should be mentioned that there is no evidence for the existence of iron/carbon atoms in the gas, but they may still exist and contribute to the NPs evolution possibly.

Chapter Ⅳ Gas phase chemical reactions in chemical vapor deposition reactor

As has been mentioned in the previous chapters, to achieve the high quality CNTs synthesis with desired properties, many factors like temperature, solution injection speed/concentration, gas flow rate/composition, position as well as time will be involved and there are strong interactions among them. Therefore, a comprehensive understanding of the interactions between the physical and chemical reactions in the CVD reactor is desired. In this chapter, the gas phase chemical reactions during CVD processes are experimentally analyzed, where xylene, acetylene and hydrogen behaviors and effects under different temperature are paid special attention. This study could guide us to optimize the CNTs synthesis process for the large-scale production in a more controlled way.

4.1 Introduction of the chemical reactions during synthesis

During the experiments of this study, the real CNTs synthesis process begins with the injection of ferrocene/xylene solution, which is atomized by the spray and brought into the high temperature reactor by the carrier gas. Thus the gas fluid in the reactor system is composed of many different chemical compositions, such as catalyst precursor ferrocene, carbon source xylene/acetylene, hydrogen, argon and the reaction products of them. To study the gas composition evolution under different experiment conditions, the first thing needs to be done it’s to study the possible chemical reactions and their products.

4.1.1 Decomposition of ferrocene

For the catalyst precursor ferrocene ($Fe(C_5H_5)_2$) used in this study, it decomposes and releases iron to form catalyst, which contributes to the following CNTs growth. However, according to Lewis and Smith[281] work published in 1984, the unimolecular gas phase decomposition of ferrocene $Fe\left(C_5H_5\right)_2 \rightarrow Fe+2C_5H_5$ has a very high activation energy (~382kJ/mol), and no decomposition could be observed when the temperature is lower than 1120K. As the CNTs growth could be observed even at 550°C in this study, it suggests that there must exist other decomposition forms for ferrocene, for example the consumption of ferrocene through reactions with radicals[282, 283]. The reduction of ferrocene at temperatures between 673 and 1173K in hydrogen atmosphere reported by Dormans[284] confirms this deduction, based on the interaction mechanism proposed by Hirasawa et al[285], Kazunori Kuwana and Kozo Saito[286] obtained a global reaction function as follow:

$$Fe(C_5H_5)_2+H_2 \rightarrow Fe+2C_5H_6$$

4.1.2 Decomposition of xylene

Xylene (C_8H_{10}) is the main carbon source in this study, which also acts as solvent for catalyst precursor ferrocene. When the xylene decomposes independently, the R-CH_3 bond need to be broken, and toluene and benzene form. However, as this R-CH_3 is very strong (434.7kJ/mol), the direct transformations from xylene to toluene and benzene is hard to achieve, which should be changed into a hydrogen atoms involved process as shown below[287]:

$$\begin{aligned}
&H_2 \rightleftarrows 2H \\
&H + C_8H_{10} \rightleftarrows C_7H_8 + CH_3 \\
&H + C_7H_8 \rightleftarrows C_6H_6 + CH_3 \\
&H_2 + CH_3 \rightleftarrows H + CH_4
\end{aligned}$$

By combining the reactions mention above, we have the global reactions as below:

$$C_8H_{10} + H_2 \rightleftarrows C_7H_8 + CH_4$$
$$C_7H_8 + H_2 \rightleftarrows C_6H_6 + CH_4$$

These global reactions have been widely used for the xylene pyrolysis and subsequent toluene pyrolysis simulation in gas phase[288-290], which indicate that C_7H_8, C_6H_6 and CH_4 are the main products for the xylene decomposition.

4.1.3 Pyrolysis of acetylene

For the CNTs synthesis in this study, acetylene (C_2H_2) is usually used as the second carbon source, which provides effective carbon supplement when the xylene decomposition degree is not sufficient. According to the study of Kiefer et al[291], the major pyrolysis products are C_4H_4 (vinylacetylene), C_6H_6 (benzene), C_2H_4, C_4H_2, CH_4 and H_2. Thanks to Koyo Norinaga and Olaf Deutschmann work[292], their simulation results give out the exact transformation percentage of these products at 900°C, which confirms that acetylene is consumed primarily to form vinylacetylene (68%), then secondly to form diacetylene (17%), and thirdly combining the vinylacetylene to form benzene (7%). The related reactions for these mentioned transformations are shown below:

$$2C_2H_2 \rightleftarrows C_4H_4$$
$$2C_2H_2 \rightleftarrows C_4H_2 + H_2$$
$$C_2H_2 + C_4H_4 \rightleftarrows C_6H_6$$

If hydrogen is injected into the reactor during the CNTs synthesis, we will also have $C_2H_2 + H_2 \rightleftarrows C_2H_4$, in which acetylene is hydrogenated to form ethylene.

In summary, the global gas-phase reactions of ferrocene, xylene and acetylene that may be involved in this study are shown in Table 4-1 below.

Table 4-1 *Global gas-phase reactions of ferrocene, xylene and acetylene involved* *during CNTs synthesis*

Index	Reaction	Reference
1	$Fe(C_5H_5)_2+H_2 \rightarrow Fe+2C_5H_6$	Kuwana, K. and K. Saito [286]
2	$C_8H_{10} + H_2 \rightleftarrows C_7H_8 + CH_4$	Benson, S. and R. Shaw[287]
3	$C_7H_8 + H_2 \rightleftarrows C_6H_6 + CH_4$	Benson, S. and R. Shaw[287]
4	$2C_2H_2 \rightleftarrows C_4H_4$	Norinaga, K. and O. Deutschmann[292]
5	$2C_2H_2 \rightleftarrows C_4H_2 + H_2$	Norinaga, K. and O. Deutschmann[292]
6	$C_2H_2 + C_4H_4 \rightleftarrows C_6H_6$	Norinaga, K. and O. Deutschmann[292]
7	$C_2H_2 + H_2 \rightleftarrows C_2H_4$	Norinaga, K. and O. Deutschmann[292]

4.2 Acetylene/hydrogen influences on gas composition

Since all the possible reactions have been listed in Table 4-1, to study the temperature influence and gas composition interaction information, MS was used to trace the quantity variation of each component. Fig. 4-1 shows an example of the MS results which were collected during the experiment, where xylene was injected into the 650°C reactor under 0.2mL/min solution injection speed, along with a 1L/min mix gas flow (0.88L/min argon, 0.1L/min H_2, 0.02L/min C_2H_2). The ion current peaks at m/z (mass to charge ratio) 2 and 40(20) correspond to the carrier gases H_2 and Ar, while the ones at 28(14), 32 and 44 are related to the residual air components N_2, O_2 and CO_2. The peaks at m/z 26 and 106 are for the injected carbon sources acetylene and xylene. C_4H_x, C_5H_x, C_6H_x, C_7H_x marked in the figure are attributed to xylene pyrolysis products.

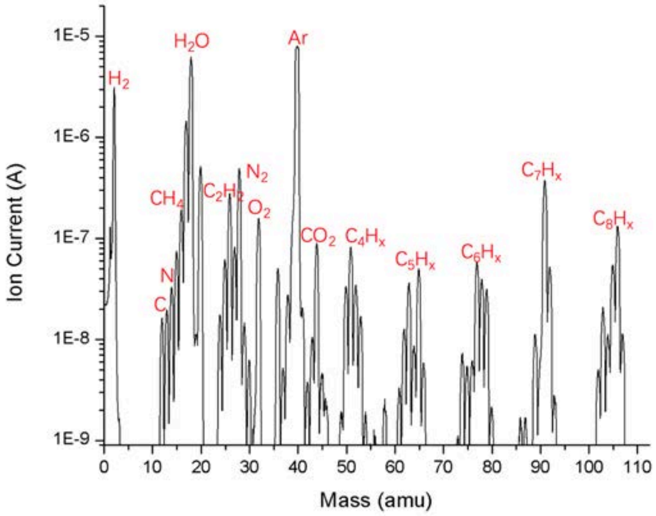

Fig. 4-1 *Example for the MS results of the gas composition.*

4.2.1 Xylene decomposition at different temperatures

The reactor temperature change always leads to gas composition variation. As xylene is the main carbon source, its decomposition information under different temperature is firstly studied. Xylene was injected at a constant injection speed 0.2mL/min, and sent into the 550°C/ 700°C/ 850°C reactor by a 1L/min argon flow respectively. The decomposed exhaust gases were collected and diagnosed by MS after 10min xylene injection (for the stabilization of the gas composition).

Fig. 4-2 shows the evolution of the ion currents at the masses corresponding to $C_8H_{10}^+$ (m/z 106), $C_7H_7^+$ (m/z 91), $C_6H_6^+$ (m/z 78), $C_5H_5^+$ (m/z 65), $C_4H_3^+$ (m/z 51), $C_2H_2^+$ (m/z 26) and CH_4^+ (m/z 16) with the increase of temperature from 550 to 850°C. According to the MS result, for the xylene, when the temperature is between 550 and 700°C, its decomposition degree only has a relatively weak increase with the temperature increase. However, if the temperature keeps rising after 700°C, the decomposition of xylene will be highly promoted, as its ion intensity has a remarkable decrease from 700 to 850°C (the order of magnitude for the corresponding ion intensity has dropped from 10^{-7} to 10^{-9}). The intensity at m/z 92 shares same variation tendency as the intensity at m/z 106, this indicates that with the augmentation temperature, the xylene decomposition product toluene is consumed rather that accumulates in the gas, compared with its creation rate, the toluene decomposition rate is more important, especially when the temperature is higher than 700°C. From the decomposition of xylene and toluene, large amount of benzene and methane have been generated, as in Fig. 4-2 the ion intensities at m/z 78 and 16 increase with the temperature augmentation. Relating these MS results with the reaction 2 and 3 listed in Table 4-1, it has been proved that the xylene decomposition will be promoted by the temperature increase, especially when the temperature is more than 700°C.

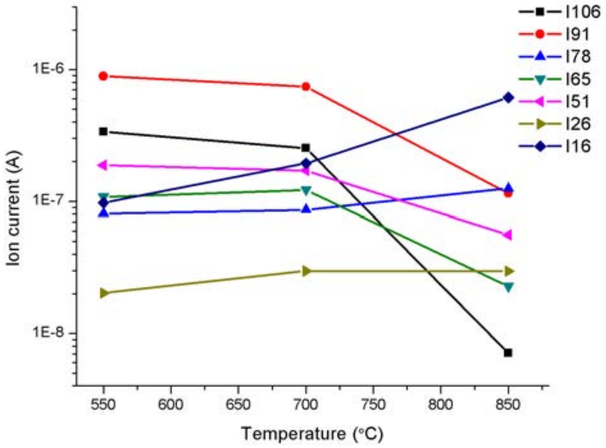

***Fig. 4-2** Evolution of the ion currents at masses (m/z) corresponding to the predominant fragments formed during the xylene decomposition at different temperatures*

4.2.2 Acetylene influence on xylene decomposition

As acetylene is usually used as a second carbon source during the CNTs synthesis, it is reasonable to study its impact on the xylene decomposition. Experiments were designed to evaluate the xylene decomposition with varying acetylene flow rate at different temperatures. The detailed experiment conditions and MS results are listed in Table 4-2 below. Based on the data presented in Table 4-2, Fig. 4-3 was drawn.

Table 4-2 *Experiment conditions and MS results in the study of acetylene influence on xylene decomposition*

Exp.	**Temperature (°C)**	**Acetylene (mL/min)**	**Ion intensity (A)**			
			m/z 106	**m/z 91**	**m/z 78**	**m/z 26**
1	550	0	3.38E-07	8.90E-07	8.08E-08	2.03E-08
2	550	10	2.39E-07	6.28E-07	5.83E-08	3.53E-07
3	550	20	2.06E-07	5.44E-07	5.09E-08	6.34E-07
4	700	0	2.53E-07	7.40E-07	8.63E-08	2.99E-08
5	700	10	1.31E-07	4.11E-07	4.92E-08	4.42E-08
6	700	20	1.19E-07	3.78E-07	4.55E-08	1.16E-07
7	850	0	7.10E-09	1.15E-07	1.25E-07	2.97E-08
8	850	10	3.35E-09	6.88E-08	9.73E-08	2.06E-08
9	850	20	2.33E-09	5.94E-08	1.02E-07	2.17E-08
General experiment conditions: Xylene injected at 0.2 mL/min injection speed and sent into the reactor by 1L/min gas flow rate (argon + acetylene)						

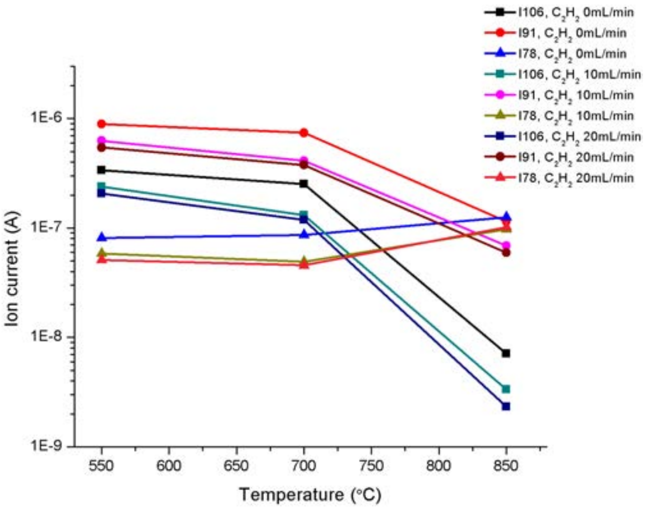

Fig. 4-3 *Comparison of the acetylene influence on xylene decomposition at different temperatures, with square, circle and triangle representing the ion current at m/z 106 ($C_8H_{10}^+$), m/z 91 ($C_7H_7^+$) and m/z 78 ($C_6H_6^+$) respectively*

According to the results presented in Fig. 4-3, it could be observed that acetylene has promoted the decomposition of xylene and toluene. Especially when the acetylene flow rate increase from 0 mL/min to 10mL/min, the ion current at m/z 106 has dropped 26% (550°C), 45% (700°C) and 50% (850°C), while the ion current at m/z 91 has dropped 26% (550°C), 41% (700°C) and 36% (850°C). This fact suggests that for xylene, with the temperature augmentation, acetylene influence on decomposition promotion has been enhanced; for toluene, when the temperature is high enough (850°C), acetylene influence on decomposition promotion is restrained to some extent, rather than enhanced like in the xylene case. When the acetylene flow rate keeps increasing from 10mL/min to 20mL/min, its decomposition promotion influence becomes more important, however, the ion current differences at m/z 106 and m/z 91 between 10 mL/min and 20 mL/min acetylene gas flow cases are not as much as before, which means that when acetylene reaches certain gas flow rate, its following augmentation has been less effective for the xylene/toluene decomposition promotion.

Acetylene decomposition promotion influence on benzene is not quite similar as its influence on xylene and toluene. When the temperature is relatively low, the addition of acetylene promotes the benzene decomposition. However, if the temperature keeps rising, it could be found that at 850°C, there are more benzene when acetylene increases from 10 mL/min to 20 mL/min. Considering the reactions related to acetylene pyrolysis listed in Table 4-2, it suggests that at high temperatures, more acetylene is transformed into benzene than at low ones. Relating the acetylene influence change on toluene at high temperature that has been just discussed, it is reasonable to believe that the acetylene decomposition promotion influence on xylene will be less effective at high temperatures. This suspect could be supported by the reaction equilibrium, as both temperature augmentation and acetylene flow rate rise will promote acetylene transformation in benzene, thus push the equilibrium of reaction 2&3 (see Table 4-2) to the xylene formation direction.

4.2.3 Hydrogen influence on xylene decomposition

As has been discussed at the beginning of this chapter, hydrogen plays a very important role for the carbon/catalyst decomposition in this study. In order to analyze the CNTs growth mechanism and achieve better control of the CNTs production, the study of hydrogen influence is indispensable. Experiments were designed to evaluate the xylene decomposition with varying hydrogen flow rate at different temperatures. The detailed experiment conditions and MS results are listed in Table 4-3 below. Based on the data presented in Table 4-3, Fig. 4-4 was drawn.

Table 4-3 *Experiment conditions and MS results in the study of hydrogen influence on xylene decomposition*

Exp.	**Temperature (°C)**	**Hydrogen (L/min)**	**Ion intensity (A)**		
			m/z 106	**m/z 91**	**m/z 78**
1	550	0	3.38E-07	8.90E-07	8.08E-08
2	550	0.1	2.48E-07	6.59E-07	6.02E-08
3	550	0.3	3.07E-07	8.01E-07	7.14E-08
4	700	0	2.53E-07	7.40E-07	8.63E-08
5	700	0.1	1.48E-07	5.87E-07	9.75E-08
6	700	0.3	1.54E-07	6.66E-07	1.33E-07
7	850	0	7.10E-09	1.15E-07	1.25E-07
8	850	0.1	2.58E-09	1.16E-07	3.51E-07
9	850	0.3	2.89E-09	1.52E-07	7.15E-07
General experiment conditions: Xylene injected at 0.2 mL/min injection speed and sent into the reactor by 1L/min gas flow rate (argon + hydrogen)					

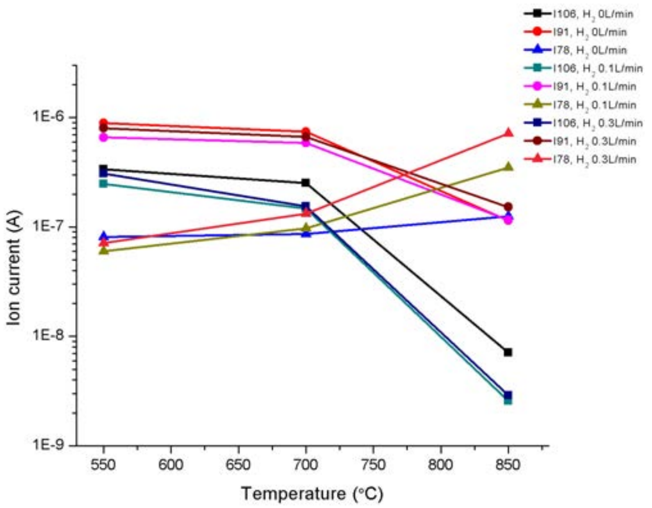

Fig. 4-4 *Comparison of the hydrogen influence on xylene decomposition at different temperatures, with square, circle and triangle representing the ion current at m/z 106 ($C_8H_{10}^+$), m/z 91 ($C_7H_7^+$) and m/z 78 ($C_6H_6^+$) respectively*

Based on the MS results shown above, it could be observed that at 550°C, the addition of hydrogen from 0L/min to 0.1L/min has promoted the decomposition of xylene, toluene as well as benzene. However, not like acetylene, hydrogen decomposition promotion influence will not be enhanced with following hydrogen flow rate augmentation. On the contrary, when the hydrogen flow increases from 0.1L/min to 0.3L/min, the ion currents at m/z 106, m/z 91 and m/z 78 has augmented, suggesting that xylene, toluene and benzene have increased with the hydrogen flow rise (see also section 4.2.4).

When the reactor temperature rises to 700°C, for xylene and its decomposition products, their decomposition change tendencies with hydrogen have been more complex. For xylene, the ion intensities at m/z 106 are 2.53E-07A (H_2 0L/min), 1.48E-07A(H_2 0.1L/min) and 1.54E-07A(H_2 0.3L/min) respectively. It suggests that at this temperature, when the hydrogen flow is above certain value, the rise of hydrogen flow will no more induce considerable variation for the xylene decomposition as much as before. For toluene, the hydrogen influence is similar as its influence at 550°C. For benzene, the corresponding ion intensities are 8.63E-08A (H_2

0L/min), 9.75E-08A (H_2 0.1L/min) and 1.33E-07A (H_2 0.3L/min), suggesting that hydrogen increase has promoted the benzene formation effectively.

When the reactor temperature is up to 850°C, due to the high temperature, large amount of xylene and toluene has been decomposed. For xylene, the hydrogen influence is similar as its influence at 700°C. For toluene, it could be found the largest ion intensity is achieved under 0.3L/min hydrogen flow. For benzene, there exist big differences among its corresponding ion intensities, whose values are 1.25E-07A(H_2 0L/min), 3.51E-07A(H_2 0.1L/min) and 7.15E-07A(H_2 0.3L/min) respectively. Hydrogen augmentation has induced more obvious benzene quantity rise than at 700°C.

Generally speaking, the addition of hydrogen will effectively promote the xylene decomposition, but its influence changes at different temperatures. When the temperature is relatively low, there is an optimum hydrogen flow rate, by which the maximum decomposition for xylene, toluene and acetylene will be achieved. When the temperature is relatively high, the optimum point fades away, and the maximum toluene decomposition/benzene formation are obtained by simply increasing the hydrogen flow rate.

4.2.4 Hydrogen influence at relatively low temperature

As has been discussed in section 4.2.3, when the reactor temperature is relatively low, there may exist an optimum hydrogen flow rate, by which the maximum decomposition of carbon sources could be achieved. In order to make further study on this phenomenon and analyze the hydrogen influence evolution on carbon/catalyst decomposition during the CNTs synthesis, experiments have been designed as follows to study the gas phase reactions: Reactor temperature 650°C, alumina substrate, 0.01g/mL ferrocene/xylene solution with 0.2 mL/min injection speed, acetylene

0.02L/min, total gas flow 1L/min (argon+ hydrogen+ acetylene), and hydrogen flow rate 0/0.05/0.1/0.2/0.3/0.4/0.5L/min respectively. It should be mentioned that the corresponding CNTs results would be discussed also in the next chapter.

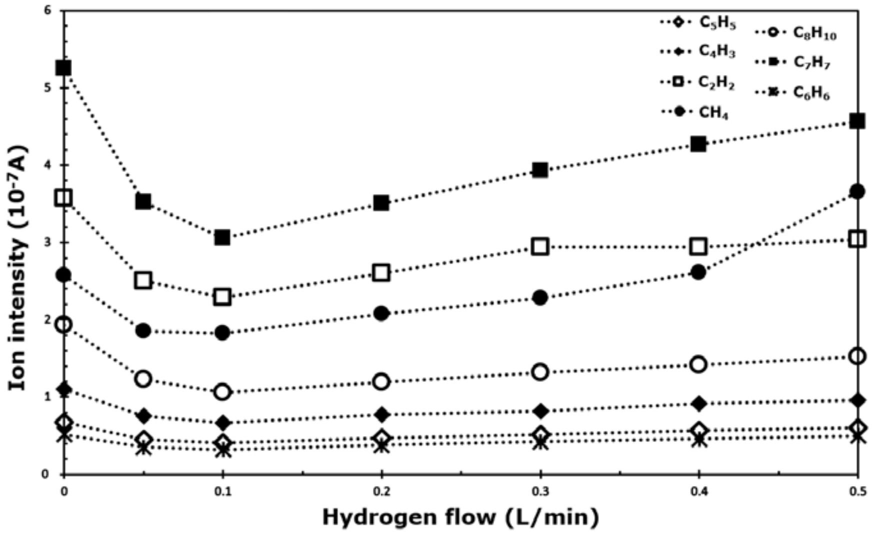

Fig. 4-5 *Evolution of the ion intensity of the main hydrocarbons present in the gas phase measured by in situ mass spectrometry as a function of hydrogen flow rate.*

MS was used to record the gas composition evolution for different hydrogen flow rates. Its results for main hydrocarbons present in the gas phase are shown in Fig. 4-5. According to Fig. 4-5, a fast decline in total hydrocarbon concentration with increasing hydrogen flow is firstly observed. When compared to the hydrogen-free synthesis data, the ion intensities representing the amounts of xylene and acetylene decrease respectively by 45% and 36% at 0.1 L/min hydrogen flow. The reduction of hydrocarbon quantities in the gas phase can be attributed to the conversion of hydrocarbon vapors into solid carbon structures. From the point of view of reaction kinetics, high hydrogen flow facilitates hydrocarbon decomposition and increases the carbon deposition rate [293], leading to increased solid carbon yield.

However, our observations at higher hydrogen flows contradict this principle. Above 0.1 L/min hydrogen, the quantities of all species in the gas phase increased, with 44% and 33% ion intensity augmentation for xylene and acetylene when hydrogen flow rise from 0.1 to 0.5 L/min. This indicates that within this hydrogen flow range, the hydrocarbon decomposition rate exceeds the rate of carbon deposition. Under these conditions, hydrocarbon pyrolysis is promoted which leads to copious amorphous carbon (see inset in Fig. 4-6), consisting predominantly of polycyclic aromatic hydrocarbons [294]. As depicted in Fig. 4-6, the mass of amorphous carbon normalized to the total mass of carbon nearly doubled when the hydrogen flow increases from 0.1 to 0.2 L/min. However, when the hydrogen was increased further, the quantity of amorphous carbon was drastically reduced. Noteworthy, for hydrogen flow ranging between 0.3 and 0.5 L/min, the amount of acetylene reaches a quasi-steady state and the quantity of methane even exceeds that of acetylene. The abrupt drop of amorphous carbon is correlated with the large amount of methane in the reactor atmosphere, as shown in Fig. 4-5. Previous studies have found that methane is the dominant product from the etching process of carbons when hydrogen is involved [295], thus indicating that high hydrogen content can induce the gasification of carbon. This peculiar behavior of hydrogen at different flow rates exemplifies the complex role hydrogen plays during CVD process.

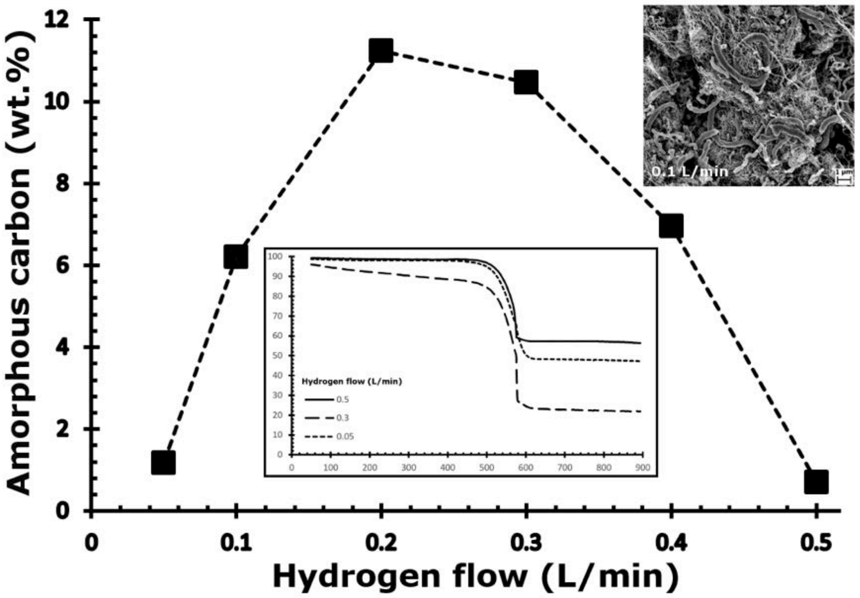

Fig. 4-6 *Mass of amorphous carbon normalized to the total mass of carbon as a function of hydrogen flow rate. The inset represents the TGA profiles of CNTs synthesized on μAl_2O_3 at 0.05 (dotted line), 0.3 (dashed line), and 0.5 (straight line)*

L/min hydrogen.

4.3 Conclusion

In this chapter, the CVD gas phase chemical reactions were experimentally investigated. It has been found that the reactor temperature has played an important role during the CNTs synthesis process, not only xylene decomposition but also acetylene/xylene influences on gas composition are impacted by the temperature variation. For acetylene, it promotes the decomposition of xylene and toluene when its flow rate is not too high. High temperature and its augmented flow rate will favor its transformation in benzene, which in turn decrease its decomposition promotion influence on xylene. For hydrogen, the addition of this component will generally promote the xylene decomposition, however, there exists an optimum hydrogen flow rate to achieve its maximum decomposition promotion at low temperatures, and this optimum point fades out at high temperature. In fact, the hydrogen influence is not only limited on the injected carbon source, the catalyst as well as the synthesis CNTs will also be impacted will hydrogen, which will be discussed in chapter 5. These results also prove that the gas composition evolution should not be ignored for the LII model calculation, for further study, more quantitative research need to be done, like making more experiments under different conditions and using the method of simulation[296-298], to establish the mathematical models for all the chemical reactions evolution.

Chapter Ⅴ Carbon nanotubes growth stage

After the process of nanoparticles formation and gas phase reactions, the carbon/catalyst deposit on the substrate and the CNTs growth begins. Influenced by the factors like temperature, solution concentration/injection speed, gas flow composition, substrate as well as growth position, various kinds of CNTs are synthesized for serving different purposes. In this chapter, all the possible influence factors were examined systematically, to study their impact on the CNTs properties. The relations between the final CNTs with the former stages were also discussed, in order to explain the CNTs growth mechanism.

5.1 Preheat influence

Among all the factors which may influence the final CNTs properties, preheat and injection speed are the factors that are involved at the earliest stage of the CNTs synthesis process. As have been discussed in chapter 2, preheat temperature change leads to droplet size and gas phased NPs size variation, there is a high possibility that the CNTs diameter will also be influenced. To verify this assumption, experiments were designed with the following conditions: reactor temperature 650°C, 0.03g/mL ferrocene/xylene solution with 0.1mL/min injection speed, acetylene 10mL/min, hydrogen 0.1L/min, argon 0.89L/min, alumina substrate, and three different preheat temperature room temperature/150°C/250°C. CNTs samples were collected after 10 min synthesis process at the position 20~30cm (See also Fig. 3-4 in section 3.2.2, in which the position influence on NPs as well as CNTs have been discussed. If not mentioned, the CNTs synthesis duration and samples collected position will be always

10min and 20~30cm for the following experiments), their diameter distributions are shown in Fig. 5-1 below, with the average diameters 15.7nm (room temperature preheat), 15.6nm (150°C) and 15.6nm(250°C) respectively. By comparing the CNTs distribution and the corresponding average diameters, it could be found that there is no obvious difference between them, even the NPs size varies with different preheat temperature. This result supports the assumption proposed at the end of chapter 3, that the CNTs synthesis process after the NPs deposition will keep influencing the CNTs. For this reason, the influence caused by NPs difference is probably reduced. As preheat temperature has no obvious influence on the CNTs diameter distribution, in the following experiments, if not mentioned, the preheat temperature was kept at room temperature.

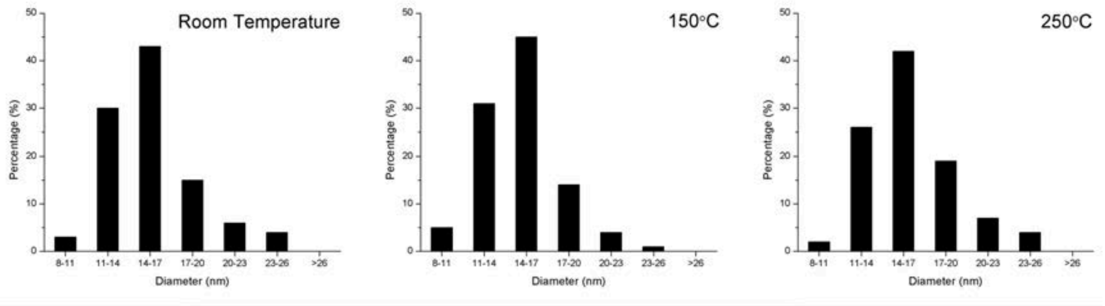

Fig. 5-1 *CNTs diameter distributions for different preheat temperature*

5.2 Solution concentration influence

During CNTs synthesis process, the adjustment of solution concentration is a convenient way to achieve accurate catalyst quantity control. As has been proved in section 3.2.5, the augmentation of solution concentration has an obvious influence for the NPs size increase, the solution concentration influence was studied in this section to verify if its change would bring other variations for the CNTs production. Experiments were designed with the following conditions: reactor temperature 650°C, 0.2mL/min solution injection speed, acetylene 20mL/min, hydrogen 0.1L/min, argon 0.88L/min, alumina substrate, and three different solution concentrations

0.01/0.03/0.05 g/mL. CNTs samples diameter distributions are shown in Fig. 5-2 below, with the average diameters 14.3nm (0.01g/mL), 16.2nm (0.03g/mL) and 17.3nm(0.05g/mL), respectively. By comparing the results for different concentrations, it could be found that the augmentation of the solution concentration favors the increase of CNTs diameter. As the NPs sizes increase also with the solution concentration rise, it supports that the NPs size will contribute to the CNTs diameter determination. However, even in the section 3.2.5 a nearly linear relation was found between the solution concentration and NPs diameter with R^2=0.95371, it appears for CNTs diameter this linear relation no more exists, which supports again the assumption that the CNTs synthesis process after the NPs deposition will keep influencing the CNTs and reduce the effect caused by gas phase NPs difference.

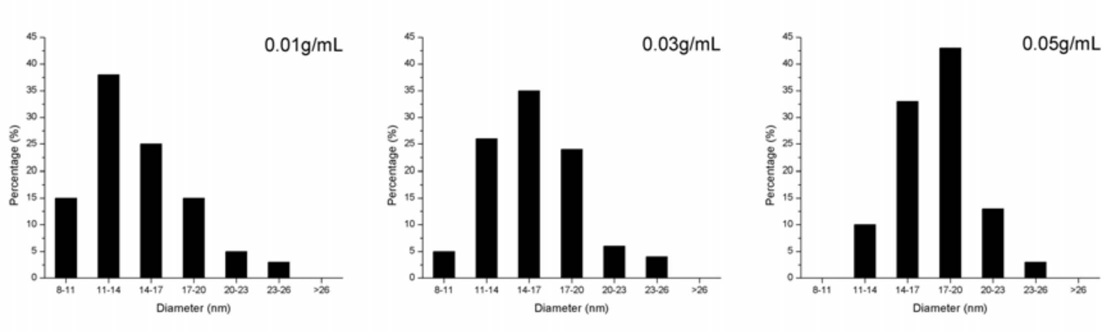

***Fig. 5-2** CNTs diameter distributions for different solution concentration*

5.3 Solution injection speed influence

Comparing with the solution concentration variation, the solution injection speed change induces not only catalyst source but carbon source quantity modification at the same time. In the previous study, it has been proved that the increase of injection speed contributes to both droplet and NPs size augmentation at the same time, mainly due to the rise of catalyst/carbon source quantity, so it’s reasonable to conclude that the final CNTs production will also be influenced. To study this influence, experiments were designed with the following conditions: reactor temperature 650°C, 0.03g/mL ferrocene/xylene solution, acetylene 10mL/min, hydrogen 0.1L/min, argon 0.89L/min, alumina substrate, and different solution injection speed 0.1mL/min, 0.2mL/min and 0.3mL/min. CNTs diameter distributions are shown in Fig. 5-3 below, with the average diameters 15.7nm (0.1mL/min), 17.6nm (0.2mL/min) and 18.5nm(0.3mL/min) respectively. As an obvious CNTs diameter augmentation could be seen, the solution injection speed increase favors the rise of droplets/NPs size and CNTs diameter simultaneously. This fact confirms the relation between the NPs and CNTs. However, the average length nearly doesn't differ, which are 16.4μm (0.1mL/min), 16.1μm(0.2mL/min) and 16.3μm (0.3mL/min) respectively. The length independence with solution injection speed was reported before[58], suggesting that the catalyst/carbon source quantities are sufficient under the applied experiment conditions. Thus their variation will not limit the CNTs growth. The SEM photos for the CNTs samples are shown in Fig. 5-4.

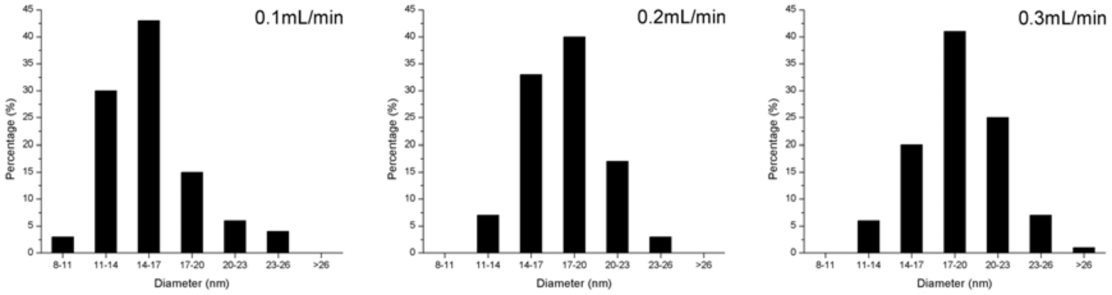

Fig. 5-3 CNTs diameter distributions for different solution injection speed

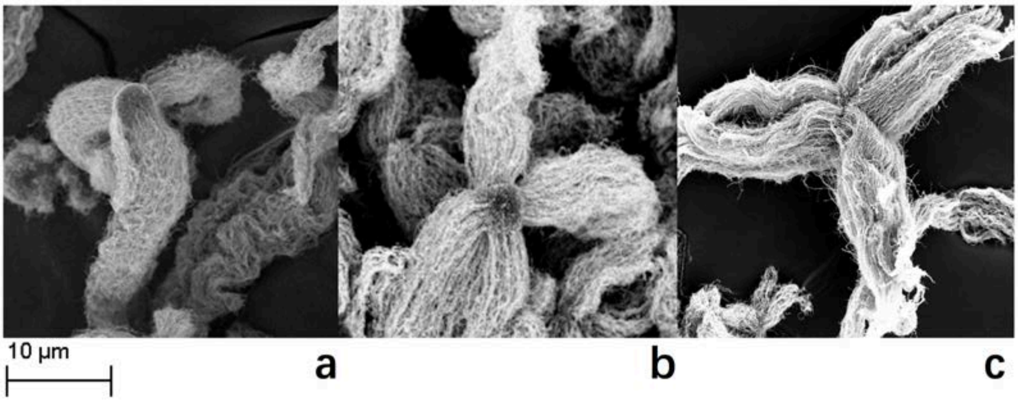

Fig. 5-4 *CNTs samples with (a) 0.1mL/min (b) 0.2mL/min (c) 0.3mL/min solution*

injection speed

5.4 Reactor temperature influence

As has been discussed, temperature is one of the most important factors during the CNTs synthesis, which will influence the NPs as well as chemical reactions. To analyze its influences on the final CNTs, three series of experiments were conducted, in which the reactor temperature was varied for different ferrocene/xylene solution concentrations. The detailed experiment conditions and the corresponding average diameter for the CNTs samples are listed in the Table 5-1 below. The CNTs diameter distributions were shown in Fig. 5-5.

Table 5-1 *Summary of the different synthesis conditions and corresponding CNTs average diameter. For each experiment, the argon flow rate, hydrogen flow rate, acetylene flow rate and solution injection speed were set constant at 0.88L/min, 0.1L/min, 0.02L/min and 0.2mL/min respectively, alumina was used as the substrate*

Experiment	Reactor temperature (°C)	Solution concentration (g/mL)	CNTs diameter (nm)
1	550	0.01	12.8
2	650	0.01	14.3
3	750	0.01	16.6
4	550	0.03	14.8
5	650	0.03	16.2
6	750	0.03	18.6
7	550	0.05	16.4
8	650	0.05	17.3
9	750	0.05	19.5

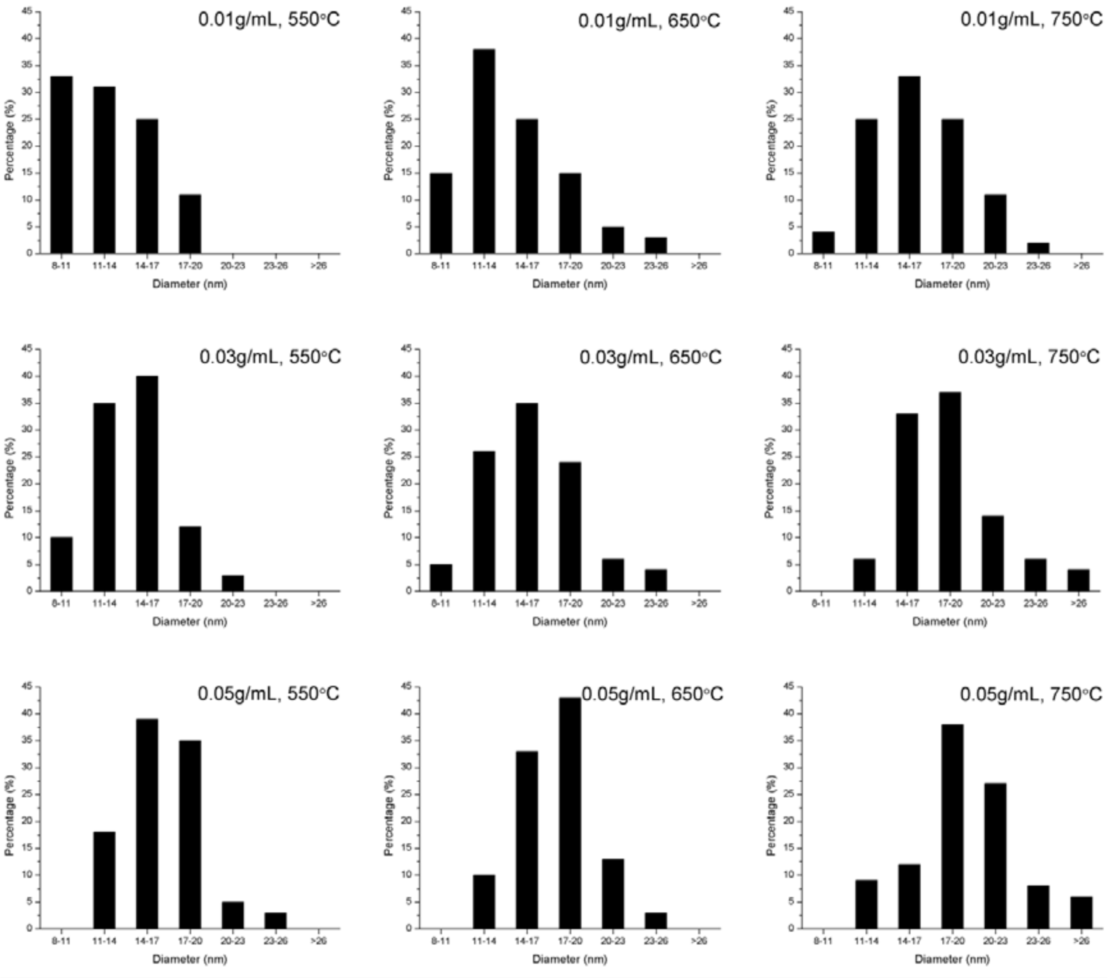

Fig. 5-5 *CNTs diameter distribution change with different temperature*

According to the results presented above, firstly the solution concentration influence on CNTs diameter was further confirmed, as the experiments in section 5.2 have been repeated at two additional temperature 550°C and 750°C; secondly it could be concluded that the temperature augmentation favors larger CNTs diameter. Noticing that the NPs size also increases with temperature (see section 3.2.3), the CNTs diameter and NPs size share same change tendency with the temperature variation, it suggest the larger NPs size contributes to the CNTs diameter augmentation. However, the CNTs differences brought by temperature change are far more than the diameter variation only, the CNTs length as well as production yield change also. Fig. 5-6 shows the CNTs products of experiment 7, 8 and 9. From this figure, it could be observed that when the temperature increases from 550°C to 650°C, the CNTs length has a significant rise, however, if the temperature keeps increasing to

750°C, only a few CNTs could be observed on the alumina substrate. This temperature-dependent behavior has its roots in the xylene decomposition evolution (see Fig. 4-2). When the temperature is under 700°C, the xylene decomposition rate increases with the temperature rise in a relatively gentle way, thus from Fig. 5-6a to Fig. 5-6b the CNTs length augments due to the addition of carbon source supply. When the temperature is more than 700°C, however, the xylene decomposition rate is highly promoted, large amount of pyrolytic carbon will cover the catalyst surface, therefore limit the catalyst activity and block the CNTs growth. Raman diagnostic was used for these samples, the I_G/I_D decrease with the temperature augmentation could be observed in Fig. 5-7. When the temperature increases from 650 to 750°C, copious amorphous carbon occurs (shown in Fig. 5-6d), while sharp decrease of I_G/I_D could be observed, both SEM and Raman results support the catalyst inactivation explanation.

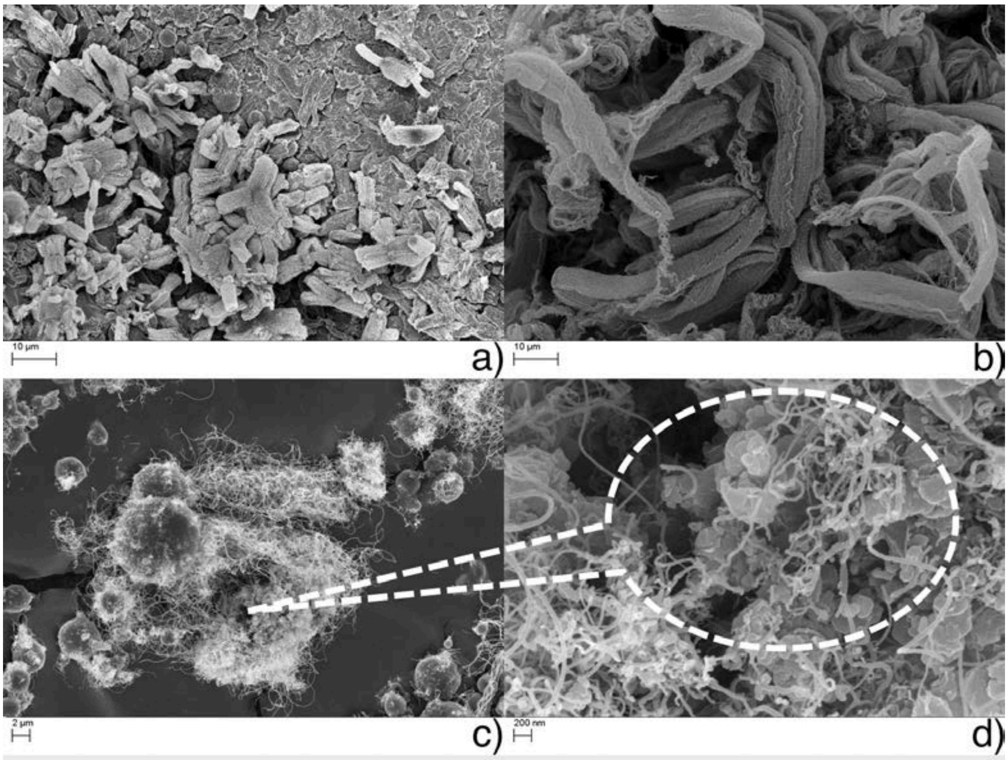

Fig. 5-6 *CNTs synthesized at different temperatures (a) 550°C (b) 650°C (c) 750°C and (d) partial enlarged view for Fig. 5-6c*

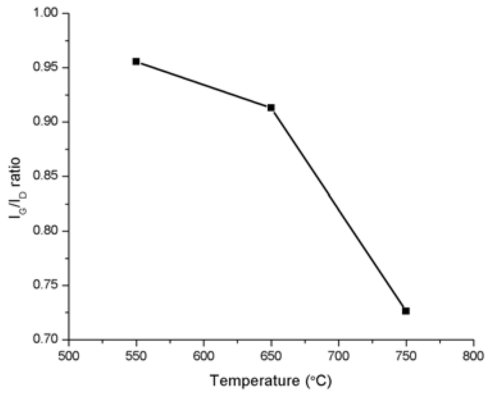

Fig. 5-7 *Raman results for the CNTs samples synthesis under different temperatures.*

5.5 Carbon sources influences

Acetylene and xylene were used as carbon sources during the CNTs synthesis. Their interactions and evolution under different temperatures have been discussed in the previous chapter. In order to find the relations between their gas phase reactions with the CNTs, Two series of experiments were designed, with the varying synthesis condition shown in Table 5-2. The diameters distributions are shown in Fig 5-8.

Table 5-2 *Summary of the different synthesis conditions and corresponding CNTs average diameters. For each experiment, the total gas flow rate, hydrogen flow rate, and solution injection speed were set constant at 1L/min, 0.1L/min, and 0.2mL/min respectively. Alumina was used as the substrate.*

Exp.	**Temperature (°C)**	**Acetylene flow (L/min)**	**Solution concentration (g/mL)**	**CNTs diameter (nm)**
1	650	0	0.05	19.9
2	650	0.01	0.05	18.5
3	650	0.02	0.05	15.6
4	750	0	0.03	20.2
5	750	0.01	0.03	19.2

6	750	0.02	0.03	18.6

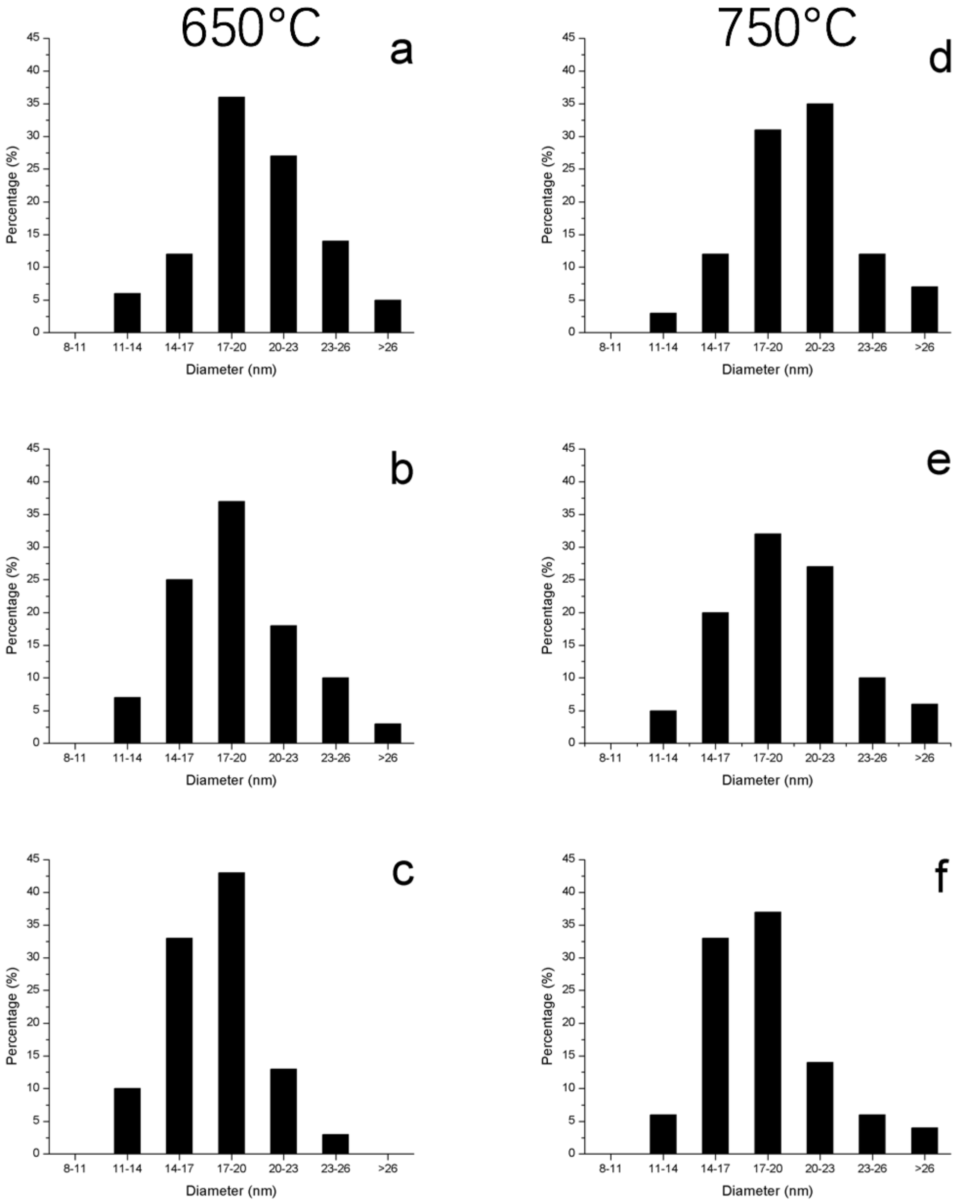

Fig. 5-8 *CNTs diameters distributions under different experiment conditions, a, b, c, d, e, f are indicated to experiment 1, 2, 3, 4, 5, 6 in Table 5-2 respectively.*

According to the results shown above, it could be found that with the augmentation of acetylene, the CNTs diameter will decrease and have a more homogenous distribution. This phenomenon is attributed to the rise of carbon source feed rate, as its augmentation will consume more nanoparticles by the CNTs formation, thus the collision and the aggregation of them will be limited and resulting in NPs volume density and the average diameter decrease, which influence consequently the CNTs diameter. Contrary to the CNTs diameter evolution, the CNTs length increases with the acetylene flow augmentation, mainly due to the acetylene decomposition promotion effects on xylene that has been discussed in section 4.2.2. The augmentation carbon source has an obvious impact on the rise of CNTs lengths, which could be observed in Fig. 5-9, in which the SEM photos for experiment 1, 2 and 3 in table 5-2 are compared.

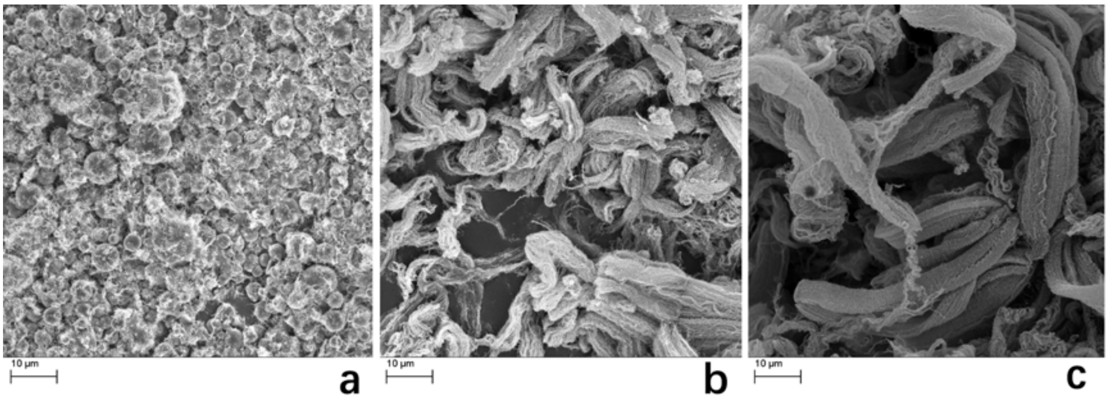

Fig. 5-9 *CNTs evolution under (a) 0L/min (b) 0.01L/min and (c) 0.02L/min acetylene flow rate*

By comparing the CNTs results shown in Fig. 5-9, it also suggests that the acetylene could be used to achieve relatively low temperature CNTs synthesis. In order to explore this issue, a series of experiments has been designed, where the two carbon sources acetylene and xylene influence as well as their interaction for CNTs growth were studied. The experiment conditions were shown in Table 5-3 below, the main difference between 3 series of the experiments is the type of carbon sources. For series 1, acetylene was the only carbon source during the synthesis, while for series 2 the carbon source was xylene. Only in series 3 the two carbon sources acetylene and xylene were simultaneously used. The SEM images for the synthesis results are shown in Fig. 5-10, in which the Fig. 5-10a, Fig. 5-10b and Fig. 5-10 represent the results for series 1, 2 and 3 respectively.

Table 5-3 *Experiment conditions for the low temperature CNTs synthesis using different carbon sources*

Series 1
Temperature increased from 400°C to 600°C, argon 0.88L/min, hydrogen 0.1L/min, acetylene 0.02L/min, 0.02g ferrocene evaporated at 190°C and sent into the system by gas flow, synthesis duration 10min
Series 2
Temperature increased from 400°C to 600°C, argon 0.9L/min, hydrogen 0.1L/min, 0.01g/mL ferrocene/xylene solution injected at 0.2mL/min injection speed, synthesis duration 10min
Series 3
Temperature increased from 400°C to 600°C, argon 0.88L/min, hydrogen 0.1L/min, acetylene 0.02L/min, 0.01g/mL ferrocene/xylene solution injected at 0.2mL/min injection speed, synthesis duration 10min

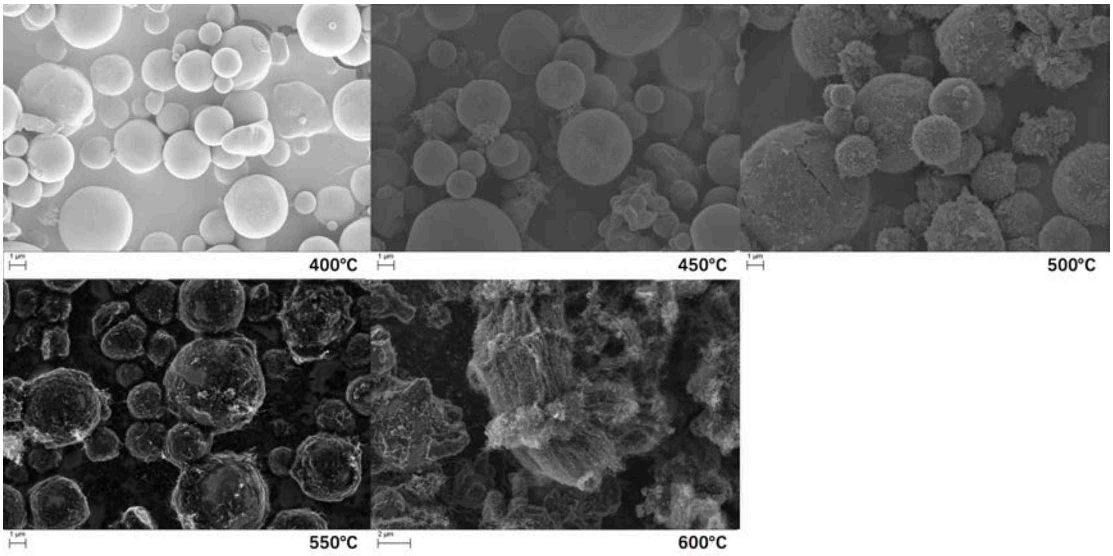

Fig. 5-10a SEM images of the synthesis products using acetylene as carbon source

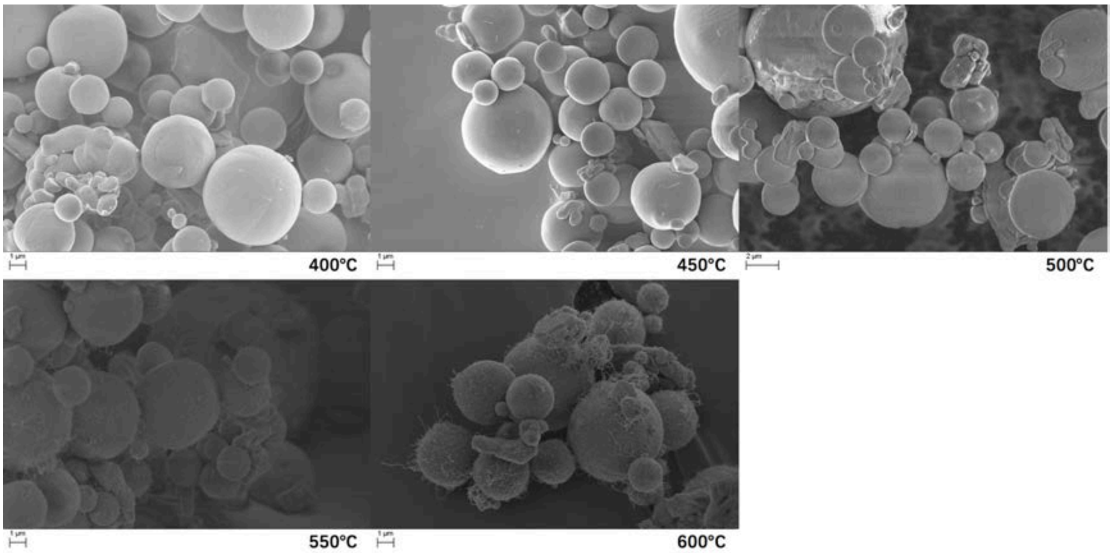

Fig. 5-10b SEM images of the synthesis products using xylene as carbon source

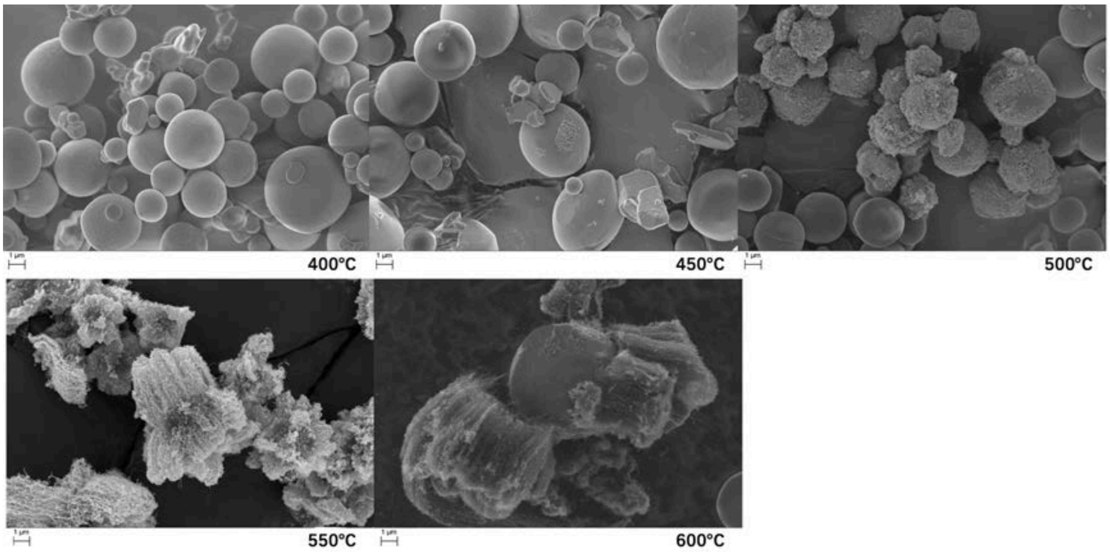

Fig. 5-10c SEM images of the synthesis products using acetylene and xylene as carbon sources

According to the figures shown above, it could be observed that with the carbon sources change, the lowest CNTs growth temperature changes also. For experiments of series 1, there was no CNTs growth on the substrate until the temperature arrived at 450°C. After this temperature, the CNTs length increased, and finally at 600°C obvious growth of CNTs was obtained. For experiments of series 2, the beginning of CNTs growth appeared at 550°C, but even at 600°C the synthesized CNTs were still very short and sparse. For experiments of series 3, the beginning point of CNTs growth was at 450°C, and dense CNTs of several micron meters were produced at 550°C. Comparing the experiment results for these 3 series, it suggests that acetylene could effectively promote the xylene decomposition, thus decrease the temperature demand for CNTs synthesis. This conclusion is consistent with the MS results that have been discussed in section 4.2.2, thus acetylene is highly recommended for the CNTs synthesis process.

5.6 Hydrogen and substrate influences

As has been discussed in former chapters, hydrogen and substrate play very important roles in CNTs synthesis. In this section, the CNTs growth was carried on quartz and alumina micro-particles (μAl_2O_3) substrates at 650 °C, with the ratio of hydrogen to total gas ranging from 0 to 50 vol.%. Relating the gas phase composition evolutions results presented in 4.2.4 with the CNT yield, length, diameter, wall number, and crystallinity, the influences of hydrogen and substrate on the properties of CNTs synthesized by FCCVD were investigated. The experiment conditions were shown in Table 5-4 below.

Table 5-4 *Summary of the different synthesis conditions. For each experiment, the reaction temperature, ferrocene concentration and liquid flow were set constant at 650°C, 0.01 g/mL and 0.2 mL/min, respectively. *No CNTs were observed under the corresponding conditions.*

Exp.	**Substrate**	**Ar flow (L/min)**	**H_2 flow (L/min)**	**C_2H_2 flow (L/min)**	**CNTs length (μm)**	**CNTs diameter (nm)**
1	Quartz	0.98	0	0.02	0.0*	0.0*
2	Quartz	0.93	0.05	0.02	6.4	24.0
3	Quartz	0.88	0.1	0.02	20.3	20.7
4	Quartz	0.78	0.2	0.02	18.6	19.9

5	Quartz	0.68	0.3	0.02	14.7	18.5
6	Quartz	0.58	0.4	0.02	13.6	17.1
7	Quartz	0.48	0.5	0.02	14.0	16.6
8	μAl_2O_3	0.98	0	0.02	0.0*	0.0*
9	μAl_2O_3	0.93	0.05	0.02	17.8	14.3
10	μAl_2O_3	0.88	0.1	0.02	33.4	14.4
11	μAl_2O_3	0.78	0.2	0.02	29.1	13.2
12	μAl_2O_3	0.68	0.3	0.02	26.5	12.1
13	μAl_2O_3	0.58	0.4	0.02	26.0	11.5
14	μAl_2O_3	0.48	0.5	0.02	24.4	11.4

5.6.1 Influence of hydrogen on the product nature

CNTs have been successfully synthesized in all cases when hydrogen was introduced in the reactor. Only pyrolytic carbon was found when hydrogen was not provided in the gas mixture, which is consistent with other reports [299, 300]. When no hydrogen is provided in the system, higher temperatures are required to achieve sufficient hydrocarbon decomposition and catalytic activity for CNTs synthesis [301]. In such case, hydrocarbon with high number of hydrogen atoms per carbon atom are critical to promote the growth of CNTs [299]. Without the presence of hydrogen in the reacting atmosphere, hydrocarbons have to chemisorb on the catalyst surface, since the formation of CHx in the gas phase is thermodynamically not favorable under the considered synthesis conditions. As the hydrocarbon molecules decompose and leave the catalyst surface covered with partially dehydrogenated fragments, polymeric carbon chains are formed, ultimately resulting in graphitic structures. However, it has been demonstrated that there exists a certain barrier during the dissociative chemisorption of hydrocarbon on catalyst surface. For example, the first step of acetylene catalytic decomposition on iron particles with formation of chemisorbed (CHx)s radicals should overcome a 1.25 eV (~16 kT at 650 °C) activation barrier

[302]. Since CNTs growth was only observed when hydrogen was introduced in the reactor, it seems reasonable to assume that hydrogen helps overcome this barrier and thus acts as a catalyst for the production of CNTs. It has been proposed that molecular hydrogen dissociates on catalyst surface and forms active hydrogen atoms [300]. These hydrogen atoms may promote the activation of physisorbed hydrocarbons, resulting in the formation of surface bound (CHx)s radical, which eventually leads to the growth of graphitic structures through the agglomeration of (CHx)s into multimeric (CnHy). This is consistent with previous research reporting that the formation of a graphitic network at the early stage of the CNTs growth occurs through the intermediate formation of partially dehydrogenated graphitic islands [303].

5.6.2 Influence of substrate on the carbon nanotubes morphology

Vertically aligned CNTs were successfully grown on both quartz and μAl_2O_3 substrates. SEM observations revealed that CNTs are aligned perpendicularly to the substrates forming carpets on quartz and multi-branched structures on μAl_2O_3, which is consistent with CNTs arrangements commonly obtained through FCCVD on similar substrates [293]. Fig. 5-11 shows that CNTs synthesized on μAl_2O_3 exhibit smaller mean diameters and are nearly twice as long as their counterparts grown on quartz. Since no differences in the gas phase composition were observed when either quartz or μAl_2O_3 were used as substrate according to MS results, it is reasonable to assume identical carbon supply rates in each case under similar conditions. The difference in CNTs morphology between quartz and μAl_2O_3 may thus be attributed to variations in the catalyst particle size between each substrate. Catalyst-support interfacial reactions play critical role on the formation of catalyst particles and their ability to dissolve carbon in seeding the nucleation and growth of CNTs. It was found that Al_2O_3 restricts Fe surface mobility, resulting in a narrow catalyst particle size distribution as compared to quartz [235]. This is illustrated by the larger distributions of CNTs wall number and inner diameter on quartz than on μAl_2O_3 in Fig. 5-12 and

Fig. 5-13. Large particle size distribution induces coarsening through Otswald ripening, which can reduce the catalytic activity, hence leading to larger CNT diameters and lower growth rates [304].

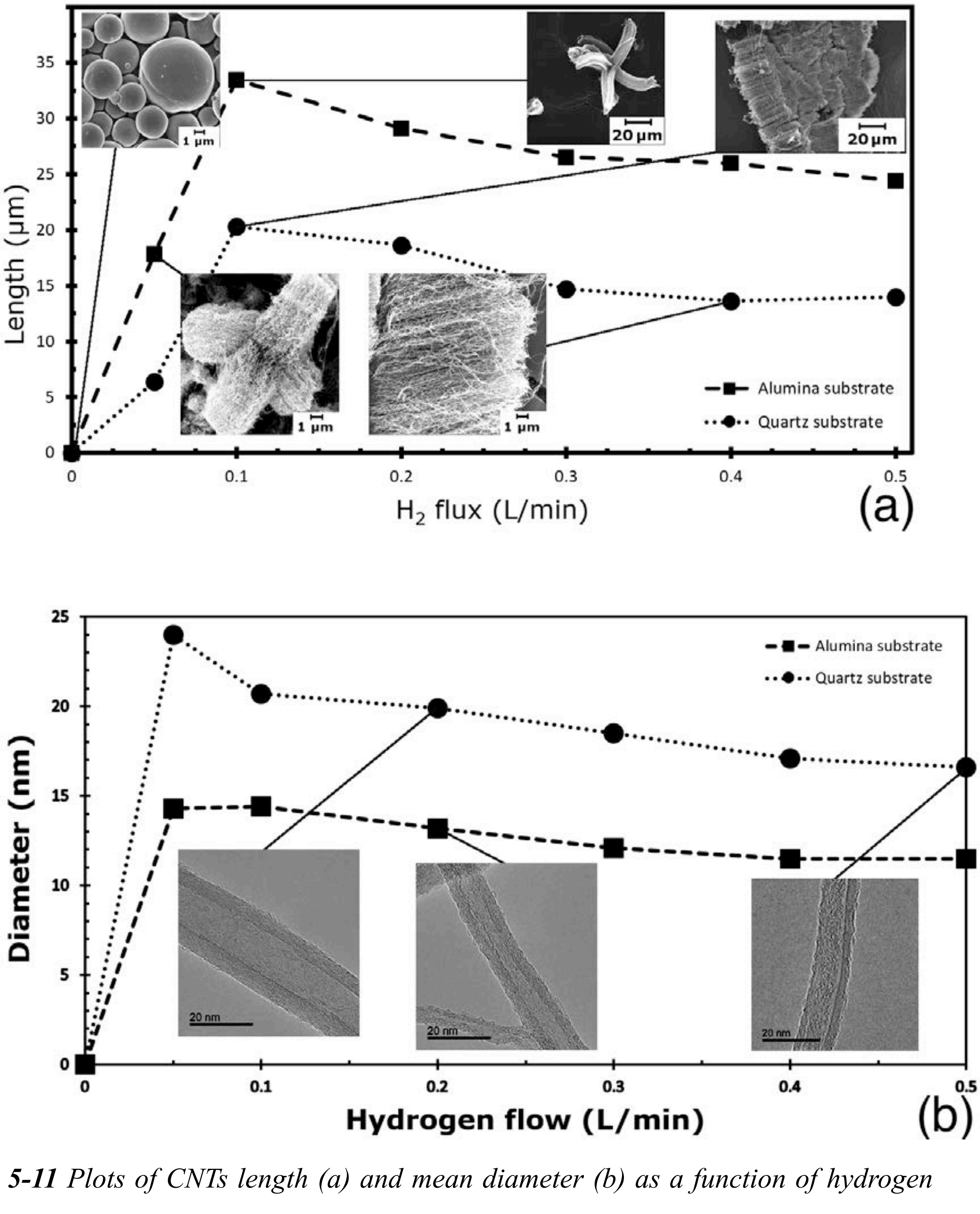

Fig. 5-11 *Plots of CNTs length (a) and mean diameter (b) as a function of hydrogen flow*

5.6.3 Influence of hydrogen on the carbon nanotubes morphology

As observed in Fig. 5-11, the evolution of CNT morphology as a function of hydrogen flow is similar on both substrates. In each case, the CNT length (Fig. 5-11a) and diameter (Fig. 5-11b) increase rapidly with the hydrogen flow and reach their maximum at 0.1 and 0.05 L/min, respectively, before decreasing as the hydrogen flow increases further. Below 0.1 L/min, increase in hydrogen flow directly translates to higher CNT growth rate, suggesting that carbon supply might be the rate-limiting step of the reaction. CNTs growth proceeds through several elementary processes, including decomposition of carbonaceous gases on the catalyst particles (carbon supply), diffusion of carbon atoms through/over the catalyst particles (carbon diffusion), and precipitation of carbon atoms as CNTs from the catalyst particles (CNT growth) [251]. The role played by hydrogen in the augmentation of carbon supply is twofold. On one hand, hydrogen promotes the decomposition of hydrocarbon vapors into more reactive byproducts [293]. On the other hand, hydrogen may also serve as an activation agent for the dissociation of physisorbed hydrocarbons on the surface of catalyst particles, as described above.

At higher hydrogen flows (*i.e.* above 0.1 L/min), carbon supply will occur more quickly than the subsequent processes (*i.e.* carbon diffusion and CNT growth), and carbon atoms will accumulate on the catalyst surface forming carbon byproducts, as described by the rapid augmentation of amorphous carbon with the hydrogen content (see Fig. 4-6 in section 4.2.4). Although the presence of these carbon byproducts does not prevent catalytic hydrocarbon decomposition and graphitization processes, it reduces the CNTs growth rate, as previously reported[294]. Furthermore, the decrease in CNTs length and diameter within this hydrogen flow range may also be attributed to catalytic hydrogenation, a process in which carbon in contact with the catalyst surface reacts with H_2 to form CH_4 [294]. The catalytic hydrogenation process was recently found to be dependent on the nature of the catalyst [299]. Hydrogen etched CNTs catalyzed by nickel, while it had no impact on the CNTs grown from cobalt. It is suggested that the activation energy for the sequential formation of multiple C−H bonds at the metal−CNT interface is lower for Ni and Fe than for Co. Consequently, there is a competition between the precipitation of carbon from catalyst particles forming CNTs and the catalytic hydrogenation process at high hydrogen contents.

To provide greater insight about the influence of hydrogen flow on the CNT diameter, the distribution of CNT wall number and core tube diameter was examined at different hydrogen flows, as depicted in Fig. 5-12 and Fig. 5-13 below.

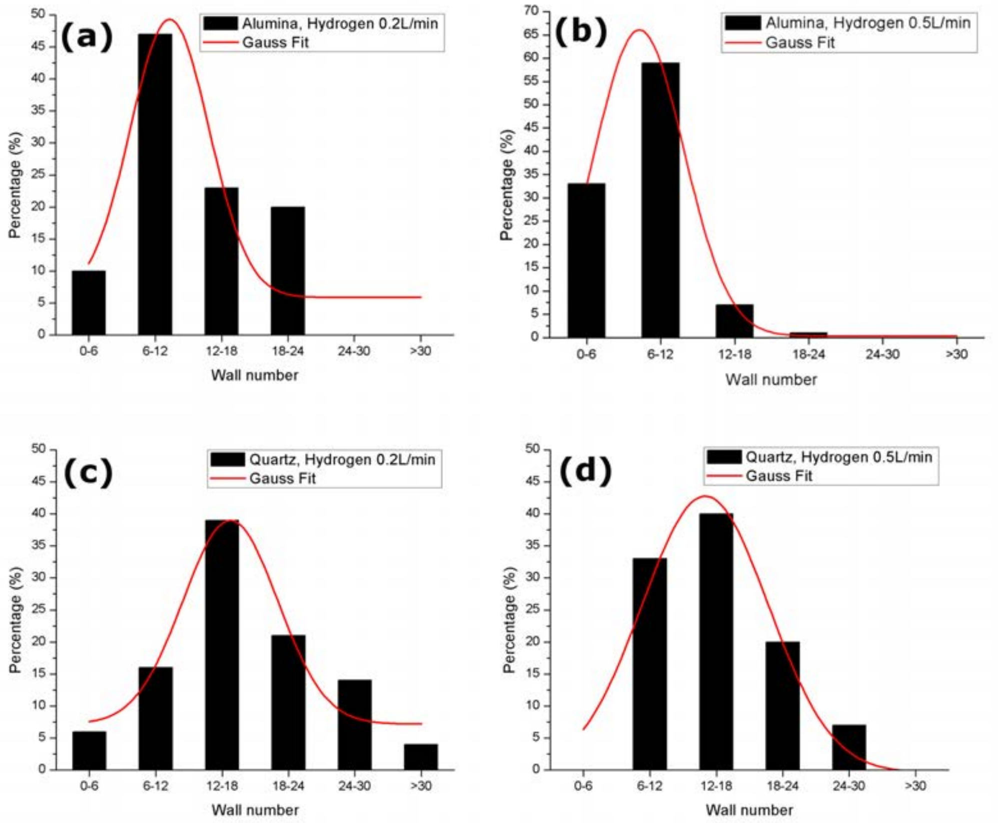

Fig. 5-12 Wall number distribution histograms of CNTs synthesized by (a,c) 0.2 L/min and (b,d) 0.5 L/min hydrogen on (a,b) μAl_2O_3 and (c,d) quartz.

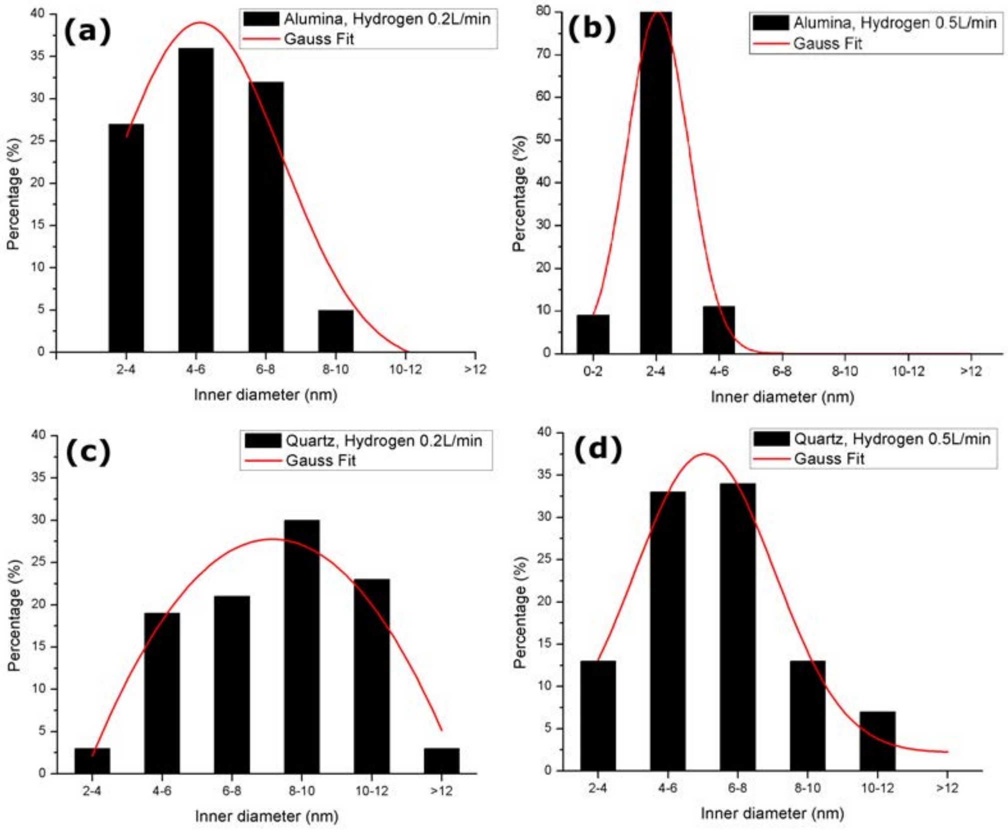

Fig. 5-13 Core diameter distribution histograms of CNTs synthesized by (a,c) 0.2 L/min and (b,d) 0.5 L/min hydrogen on (a,b) μAl_2O_3 and (c,d) quartz.

Based on Fig.5-12 and Fig. 5-13 results, it could be found that for quartz and μAl_2O_3, all changes in the CNTs wall number distributions as a function of hydrogen flow are rather small compared to those in the CNTs inner diameter distribution. There is no or little variation in the wall numbers of CNTs prepared on both substrates as a function of hydrogen flow (*i.e.* 6-30 walls on quartz, and 6-24 walls on μAl_2O_3), and the Gaussian bell-shaped curves used to fit the data remain nearly identical when the hydrogen flow increases from 0.2 to 0.5 L/min (Fig. 5-12). However, the Gaussian fits of the core tube distribution grown on both substrates are shifted toward lower diameters when the hydrogen flow rate is more than doubled (Fig. 5-13). Moreover, the CNTs inner diameter distributions are narrower at high hydrogen flow rate. The Full Width at Half Maximum (FWHM) of the Gaussian fits of the core tube distributions for CNTs prepared on quartz by 0.2 and 0.5 L/min are 7 and 4, respectively. Similarly, the FWHM of the corresponding Gaussian bell-shaped curves of the inner diameter distributions for CNTs prepared on μAl_2O_3 by 0.2 and 0.5 L/min are 5 and 2, respectively. These observations are in contradiction with previous results where hydrogen was found to have a pronounced effect on the wall number of CNTs [305]. In this report, a pre-deposited catalyst CVD process was used and yielded CNTs with smaller diameter, including single-wall and double-wall CNTs. According to the statistical analysis of Chiodarelli et al. [306], when the average outer diameter increases, the inner diameter is no longer solely related to the outer diameter, but is also influenced by CVD parameters. In particular, it was found that the inner diameter is modified by the instantaneous carbon concentration of the catalyst particle, which depends on both carbon supply and consumption [307]. As abovementioned, hydrogen likely influences the carbon supply in both deposited and floating CCVD systems. Hence, the variations between these two researches may arise from different mechanism involved in the formation of catalyst particles. In the present work, the decomposition of ferrocene leads to the *in situ* nucleation of catalyst particles. Since ferrocene decomposition is significantly influenced by the presence of hydrogen in the reacting atmosphere [293, 308], it is reasonable to assume that hydrogen plays a role in the formation of catalyst particles, thus indirectly influencing the carbon consumption. While ferrocene spontaneously decomposes at temperature higher than 500 °C [309], the rate of decomposition is reduced in a hydrogen environment. Since the first step in ferrocene decomposition is the breaking of a C-H bond with the production of hydrogen [286, 310], the presence of high hydrogen content in the reactor would suppress the rate of ferrocene decomposition, hence resulting in lower catalyst particle size and availability. To validate this claim, further work is required to investigate the effect of hydrogen on the catalyst nanoparticle growth dynamics.

5.6.4 Influence of hydrogen on the carbon nanotubes crystallinity

Representative Raman profiles of the as-grown CNTs are presented in insets of Fig. 5-14, which is a plot of the I_G/I_D ratio of the CNTs as a function of hydrogen flow rate. All specimens display strong peaks near 1336 and 1590 cm^{-1}, assigned to the D- and G-bands, respectively. The G band is the characteristic peak for the stretching vibration of carbon sp^2 bonds in a hexagonal lattice, and the D band corresponds to the disordered sp^2 phase plus possible contributions of the scattering of sp3-bonded carbon [311]. The integrated intensity ratio of the G band to the D band (I_G/I_D) is commonly invoked as a benchmark of the CNT crystallinity. Based on the Raman results, it could be found that in all cases, the I_G/I_D ratio is smaller than 1 and the relatively low-quality nature of CNTs can be identified from the zoomed-in TEM images (insets Fig. 5-11b) as their rough surfaces. The presence of defects along the walls and at the ends of the nanotubes is also consistent with the relatively low thermal stability of CNTs (*i.e.* ~550 °C) observed by TGA, which has been shown in Fig. 2-6b in chapter 2.

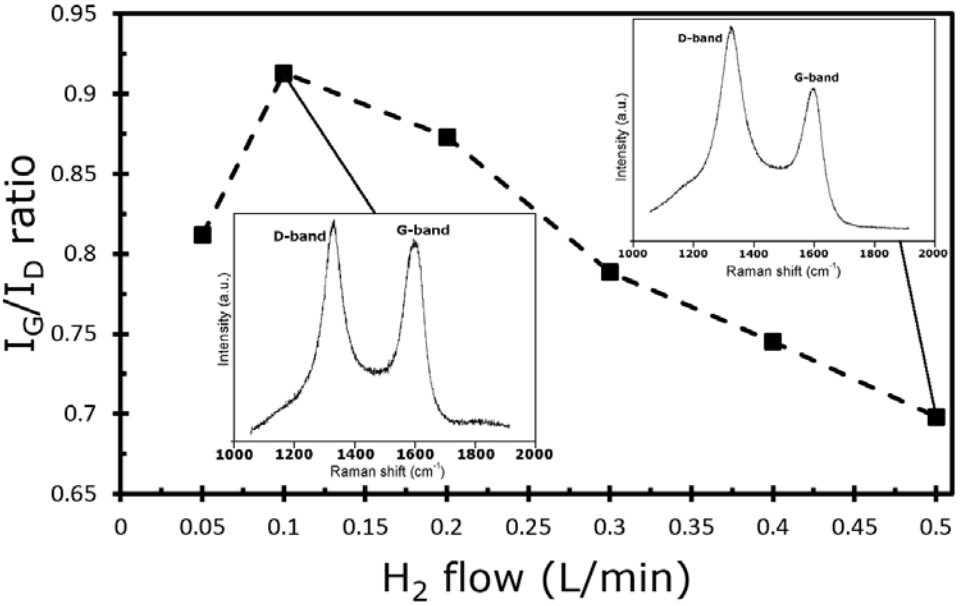

Fig.5-14 *Plot of the I_G/I_D ratio of CNTs grown on μAl_2O_3 as a function of hydrogen flow. Representative Raman spectra are shown in insets*

The hydrogen flow exhibits a pronounced effect on the CNT crystallinity. The I_G/I_D ratio first increases with higher hydrogen flow rates up to 0.1 L/min, where CNTs with the best structural integrity are observed. Comparing Fig. 5-11a with Fig 5-14, it can be found that longer CNTs tend to present higher crystalline quality, which is consistent with other studies [305]. For hydrogen flow rates ranging from 0.1 to 0.5 L/min, the defect site surface density of CNTs increases with the hydrogen content, with the I_G/I_D passing from 0.91 to 0.70. In particular, the I_G/I_D ratio remains close to 1 until the hydrogen flow rate reaches values equal or above 0.2 L/min where the CNT crystalline quality drastically diminishes.

During the FCCVD process, many unreacted compounds remain and attach to the CNTs surface. It is known that H atoms can etch carbonaceous materials [312, 313], and it seems reasonable to assume that hydrogen serves a similar role for the desorption of carbon species during the CNT growth process. At relatively low flow rates (below 0.1L/min), hydrogen can help etching these materials, hence increasing the I_G/I_D ratio. However, these impurities deposited on the CNTs surface along with defects on CNT walls may also act as the activation centers for the hydrogen etching effect, as observed in the formation of holes in graphene [300]. At higher flow rates, hydrogen can adsorb on these activated sites, non-uniformly distributed across the CNT length, in a similar way as reported in hydrogen storage studies [314]. The adsorption of hydrogen results in the occurrence of structural transformations in the continuous cylindrical graphene walls of nanotubes, as shown by the augmentation of the D-band in the Raman spectra at high hydrogen content (insets Fig. 5-14). These observations are consistent with recent reports about the surface modification of graphene and CNTs by annealing in hydrogen atmosphere [315].

In summary, we have demonstrated the efficiency of the sole regulation of hydrogen flow for controlling the products nature and morphology during the FCCVD synthesis of CNTs. Vertically-aligned CNTs were successfully grown on different substrates and the CNTs aspect ratio and crystallinity were adjusted through variations in hydrogen flow. The relative hydrogen content plays an important role in both gas chemistry and CNT growth mechanism. Hydrogen was found to promote hydrocarbon dissociation and supposed to decrease the decomposition rate of ferrocene, while leading to carbon gasification with formation of methane at high flow rates. Hydrogen may also act as catalyst in the dissociative sorption of hydrocarbons onto the surface of metal nanoparticles, thus facilitating the production of CNTs at lower temperatures. High hydrogen contents also induced the catalytic hydrogenation of carbon and resulted in surface modification in the continuous cylindrical graphene walls of nanotubes. Therefore, to achieve selective CNT synthesis at low temperatures, the right amount of hydrogen is required to balance these different effects.

5.7 Conclusion

In this chapter various factors like preheat/ reactor temperature, solution concentration/injection speed, carbon sources, hydrogen as well as substrate have been investigated to analyze their influence on the CNTs product. The preheat was firstly proved to have no obvious influence on the CNTs products, even the droplet/NPs were quite susceptible by it, which suggests an influence reduction of the NPs by the following CNTs synthesis process. For solution concentration, the change of its feeding rate generates the variation of Fe/C ratios in CVD reactor, which in turn leads to the variation of CNTs diameter distribution. The changing of solution injection speed affects on both carbon and catalyst source quantity, however no remarkable difference were found for the CNTs length under the experiment conditions, suggesting that under certain cases the injected carbon source quantity is not the definitive factor for the CNTs growth. On the contrast, temperature always influences the carbon/catalyst decomposition rate, and determines the real carbon supply rate for CNTs growth. For a given temperature, the choice of carbon source is very important, acetylene has been found having an effective promotion effect on the xylene decomposition, thus decrease the temperature demand for CNTs synthesis. The relative hydrogen content plays an important role in both gas chemistry and CNT growth mechanism, its influence behavior change under different temperature. Even all the factors mentioned above are identical, the synthesized CNTs properties still change according to the substrate choice. Based on these facts, the interactions among involved factors have made the CNTs synthesis a very complex system to control. To achieve a CNTs synthesis with desirable properties, a systematic study on these factors is always highly required.

General conclusions

This thesis focuses on the NPs evolution process and their relation with the CNTs, as well as CVD parameters influences on their properties. The main results are concluded as follows:

1. Evolution of nanoparticles during the synthesis

During the CVD synthesis, the ferrocene/xylene solution was injected into the furnace by a spray, resulting in droplets that could be regarded as the carbon/catalyst precursors at the very early stage. The droplet size could be influenced by the preheat temperature, solution injection speed as well as gas flow rate, while the solution concentration variation doesn't show any obvious influence. The essence of the droplet size determination is an energy transfer process in mechanical and thermal way. The droplets were sent into the reaction zone by the gas flow, during this process the NPs were formed. The TEM results suggest that carbon NPs are in the majority, while the iron NPs are in the minority. Using LII technique, the evolution of the NPs was studied. It was found that the NPs volume density and their sizes are firstly dependent on the diagnostic time and position. If the time and position factors are fixed, the CVD parameters like preheat/reactor temperature, solution injection speed/concentration, as well as gas flow rate/composition could influence the NPs quantity and size. To achieve accurate control of the NPs size, all the factors need to be considered for the optimum performance.

Experiments results revealed that the droplets and nanoparticles are closely related. The NPs evolution process could be described as the procedure below: When the droplets form, their sizes are keeping decreased by the solvent evaporation. The solute diffuses at the same time, and the precipitation process begins. Generally the carbon and iron elements released by decomposition reactions begin to form the nanoparticles, along with the collision and coagulation. After that the final form nanoparticles are generated, which will be deposited on the substrate for the following process. (see chapter 3)

2. Gas phase chemical reactions

Besides the influences caused by the carbon/catalyst quantity variation, the reactor temperature has played the most important role in the determination of gas composition, as high temperature would promote the decomposition of ferrocene/xylene. For acetylene, it could promote the decomposition of xylene and toluene when its flow rate is not too high. In contrary, high acetylene flow rate will favor its transformation in benzene, which in turn impedes xylene decomposition. For hydrogen, the addition of this component would generally promote the xylene decomposition. When the reactor temperature is relatively low (less than 700°C), there exists an optimum hydrogen flow rate, by which the maximum consumption of the carbon sources could be achieved, but this optimum point fades out at high temperature. (see chapter 4)

3. Carbon nanotubes influenced by CVD parameters

The CVD parameters like preheat/reactor temperature, solution concentration/injection speed, carbon sources, hydrogen as well as substrate were investigated to analyze their influences on the CNTs product. It was found that the preheat temperature has no obvious influence on the CNTs products, suggesting an influence reduction of the NPs in the following CNTs synthesis process. Substrate type was proved to be a critical parameter for the CNTs synthesis, as obvious variations on the CNTs properties have been observed between the quartz and alumina substrate. Besides the preheat temperature and substrate, all the parameters which can induce NPs size variation have the same influence tendencies on the CNTs diameter, indicating that there is a tight relation between the NPs and the CNTs.

In summary, the CNTs synthesis is a successive process, usually the influences of the CVD parameters like temperature, gas composition, carbon/catalyst source quantity etc. on the very early stages could result in the final product properties variation. Moreover, there exist interactions between the CVD parameters. Therefore, in order to achieve large scale CNTs production of the desired structures, a systematic study of these factors is always highly required

Perspectives

As we have mentioned in the thesis, LII technique was used to trace the NPs evolution during the CNTs synthesis. It is a very convenient method, which can provide in-situ diagnostic without the need for sample preparation. However, there still exist some shortcomings that require to be improved, which are listed below:

(a) LII technique can't be used to identifier the NPs nature. In this study, our LII model was established by the comparison between the HRTEM images and the LII data. The LII technique alone can't supply the information like NPs nature, chemical composition as well as physical state. Therefore, other diagnostic methods are required to obtain more information about the NPs.

(b) LII results can only reflect the communal information. The NP sizes determined by LII in this study correspond to an average value over the volume exposed to the laser beam. Moreover, the bigger NPs have a much more contribution over the smaller ones to the LII signal intensity (see also Annexes A2.3).

(c) LII can't give a quantitative analysis for the NPs volume density. In this study, the LII maximum intensity has been used for a qualitative analysis of the NPs volume density, however, there are many other factors that may influence the LII signal intensity, such as detection position, cleanness of the quartz tube, as well as laser pulse intensity. To achieve an accurate quantitative analysis, the experiment process needs to be improved to limit the possible perturbation.

For the study of CVD parameters influences, there are also many points need to be improved, which are listed below:

(d) The production yield study should be accomplished. As in this study, the CNTs synthesis duration was limited to 10min, thus the production yield is relatively low, which is not enough to be balanced. In order to evaluate quantitatively the CNTs production yield, the experiments should be repeated to collect more CNTs products.

(e) In this study the analyses of the chemical reaction are relatively qualitative, so for the further study, more experiments and simulations about the chemical reactions are highly required for establishing a quantitative mathematical model, which will contribute to a better understanding on the evolution of the chemical reactions process under different experiment conditions.

(f) Even the experiments have been carried out on the influences of different factors on the droplet/NPs/CNTs, there still exist unknown parts especially about the transition between them. More researches are needed for building a global theory to explain all phenomena which occur during the synthesis.

(g) In the study of substrate influence, only hydrogen flow was varied. As it has been proved that temperature plays an important role during the whole process, substrates influences should be compared at different temperatures, and with more substrate types.

Annexes

A1 Unreliability of laser intensity

The laser intensity isn't stable in this study, it changes with laser incident angle and there is always energy loss during laser transmission, which makes the calculation of the absorption part of the LII model not reliable. The discussion about this uncertainty will be shown in 2 aspects. In the flowing tests, the laser tension will be kept at 1.3kV with 0.35μs Q-switch.

A1.1 Instability of laser

In order to evaluate the laser intensity change, the laser pulse was activated more that 100 times with its fluence recorded each time, the record frequency is 0.1 Hz. The related energy distribution (Fig. A1-1a) and the fluence evolution with time (Fig. A1-1b) were shown below:

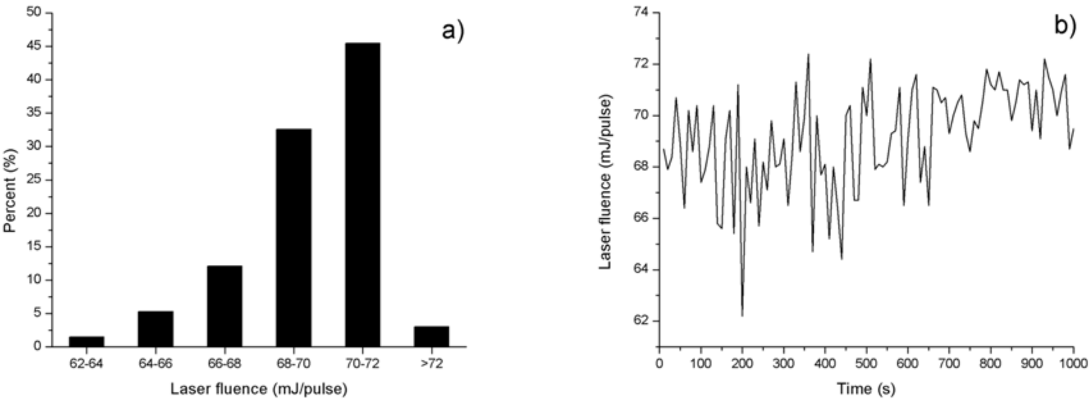

Fig. A1-1 *Laser pulse related energy distribution (a) and fluence evolution with time (b)*

Based on results shown in Fig. A1-1, it could be found that difference the between the maximum/minimum fluence is as much as ~10 mJ/pulse in the first 500s, then with the increase of time, its stability has been improved. However, this improvement is still not good enough, as there still exists a ~ 5 mJ/pulse difference. Comparing to the average laser intensity 69.4 mJ/pulse, the difference in laser intensity is too important to be ignored.

A1.2 Energy loss caused by transmission

Besides its own instability, the laser intensity is also susceptible to the thickness and cleanness of the quartz wall. Experiments have been made to evaluate the laser energy loss due to the transmission with the very clean quartz plates, which have the same thickness (5mm) as the quartz tube wall, the testing results for the fluence energy distribution are shown in Fig. A1-2 below.

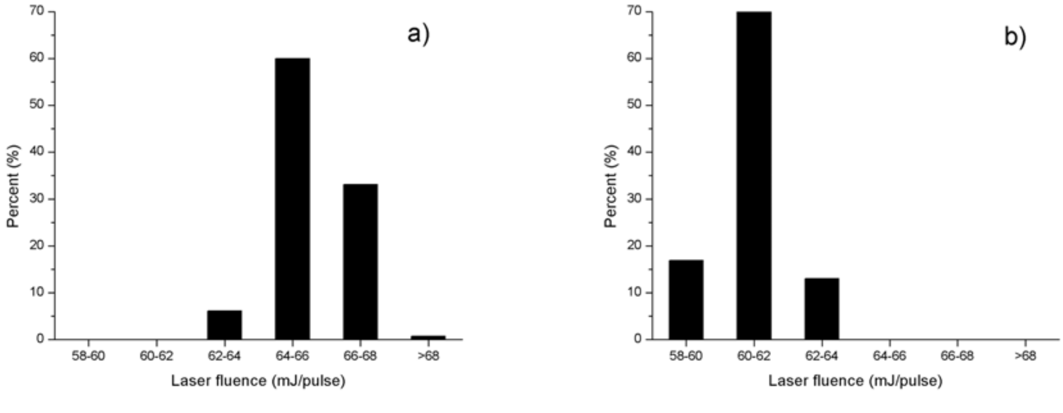

***Fig. A1-2** Laser intensity distribution after the energy loss due to transmission with 5mm thick quartz (a) 10mm thick quartz (b)*

Based on the testing results, it could be found that it exists the energy loss during the laser transmission. The average value of laser intensity is 65.6 mJ/pulse and 60.9 mJ/pulse after the transmission of 5mm and 10mm thick quartz respectively. As the average value of the original laser intensity is 69.4 mJ/pulse, this energy loss due to transmission should be taken into consideration.

Besides the tests that have been made using the clean quartz plate, the influence of quartz tube cleanness degree has also been researched. A very clean 5mm thick quartz plate has been put into the middle of the reactor to experience a CNTs synthesis process, and then cleaned by a heating process (from room temperature to 800°C) in air to remove the CNTs. This process was repeated ten times for this quartz plate to simulate a used quartz tube wall. The energy distribution of the laser intensity after its transmission of the mentioned quartz plate is shown in Fig. A1-3 below, the corresponding average value for laser intensity is 49.6 mJ/pulse in this case, which is 19.8 mJ/pulse less that its original average value.

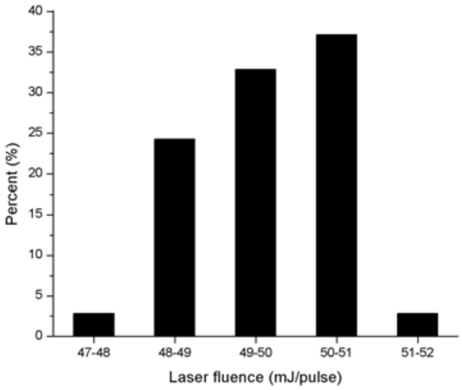

Fig.A1-3 *The energy distribution of laser intensity after its transmission of a not clean quartz plate*

A1.3 Conclusion

According to the presented results in this part, it could be concluded that the laser intensity is easy to be influenced and decreased, so it is not advisable to be used for the heat absorption of the nanoparticle, for every test, the Two-color Pyrometry is a better method to find the exact temperature during the heat transfer process, by which the LII signal curves could be well determined to find the NPs size without the perturbation of the laser intensity uncertainty.

A2 Discussion about the LII model

A2.1 Comparison of the heat loss by different processes

As has been talked about in chapter 2, for different heat loss processes, their influences change with the temperature. For a typical case where the NPs size is 15nm and the maximum temperature is 4000K with a 923.15K gas environment temperature (supposing the nanoparticles are formed by a xylene precursor, with solution injection speed 0.2mL/min and argon flow 1L/min), a comparison of the temperature change ratio (with unity K/s before the normalization) due to radiation, conduction and sublimation was made. The result was shown in Fig. A2-1.

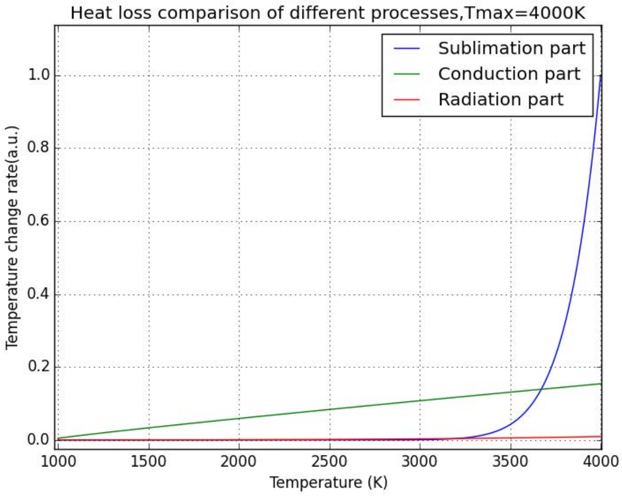

Fig.A2-1 *Comparison of the temperature change ratio caused by radiation, conduction and sublimation (with change ratio normalized)*

By the results shown in Fig.A2-1, it could be seen that the heat loss caused by sublimation increases in an exponential form when the temperature is more than 3000K. It confirms the necessity to add the sublimation part in the LII model, especially as in the first dozens of nano seconds the nanoparticle temperature is relatively high. Besides the sublimation part, the conduction part has a dominant influence on the heat loss, as the heat loss by the radiation part is relatively weak during the whole particle cooling process, which also explains why it has been said that the choice for the emission coefficient of nanoparticle ε value in the radiation part doesn't matter for a certain extent.

A2.2 Influence of the gas composition on the LII signal

As has been discussed, except the sublimation part, the conduction part has a dominant influence on the heat loss. Since for this part we have $\dot{Q}_{cond} = \frac{1}{2}\alpha_T \pi r_p^2 P_g \sqrt{\frac{8k_B T_g}{\pi m_g}} \frac{\gamma+1}{\gamma-1}\left(\frac{T_p}{T_g}-1\right)$, it is important to determine the factors m_g and γ, which can be varied according to the gas composition and temperature. In this study, the gas contains Ar, H_2, xylene (C_8H_{10}), toluene (C_7H_8), benzene (C_6H_6), acetylene (C_2H_2) and methane (CH_4) etc. They are the main gas components[297]. Their molar mass and specific heat capacities are listed in the following Table A2-1

***Table A2-1** Summary of the molar mass and specific heat capacity of the main gas compositions[316-319]*

Components	**Molar mass** $\mathrm{g \cdot mol^{-1}}$	**Specific heat capacity** $(\mathrm{J \cdot mol^{-1} \cdot K^{-1}})$
Ar	39.95	$20.786 + 2.825911\times10^{-7} * T - 1.464191\times10^{-7} * T^2 + 1.092131\times10^{-8} * T^3 - 3.661371\times10^{-8} * T^{-2}$
H_2	2.02	30.0 (650°C)
C_8H_{10}	106.16	298.4 (650°C)/ 313.1(750°C)/325.6(850°C)
C_7H_8	92.14	251.4(650°C)/ 263.3(750°C)/ 273.6(850°C)
C_6H_6	78.11	203.7(650°C)/ 213.0(750°C)/ 221.0(850°C)

C_2H_2	26.04	66.3(650℃)/ 68.4(750ɔ˚)/ 70.3(850℃)
CH_4	16.04	70.1(650℃)/ 74.6(750℃)/ 78.7(850℃)

Combining the data in the table with the gas composition info (tested by MS), it could be found out that the molar mass of the mixed gas could vary from 32.5 g/mol to 42.3 g/mol in this study, and the difference for γ can be as much as 0.13 (from 1.27 to 1.40). In this case, for the $\frac{\gamma+1}{\gamma-1}$ in $\dot{Q}_{cond}$, it changes from 8.4 to 6.0, so the heat loss efficiency in conduction part has been decreased ~29%. These differences are so considerable that can't be ignored in the LII model.

A2.3 Influence of the NPs size distribution

During the experiment process, the nanoparticles are formed after the precursors' decomposition. They don't have a uniform size so their size distribution needs to be considered. Fig. A2-2 shows a typical NPs size distribution, the experiment conditions for this nanoparticles formation are as follows: Reactor temperature 650℃, 1L/min argon, pure xylene with 0.2mL/min solution injection speed, samples collected at the reactor center after 8min of the xylene injection. In this distribution, its average value is 9.54nm, with the maximum/minimum diameters equal to 27.8nm and 2.5nm, which means that the former's diameter is 11.12 times larger than the latter one. However, in the LII model, if both charged by 0.2J/cm^2 laser intensity, the corresponding signal intensity ratio for these two nanoparticles is much more than that, which reaches 236.8 when the nanoparticle arrives at its maximum temperature. By this calculation, it could be noticed that in the LII model, the nanoparticles with larger sizes have a much more contribution over the smaller ones to the LII signal intensity. Based on this fact, a simple average value can't serve for the LII technique, so in chapter 2 the Sauter diameter was used, in which the bigger nanoparticles have more weight for the equivalent diameter calculation.

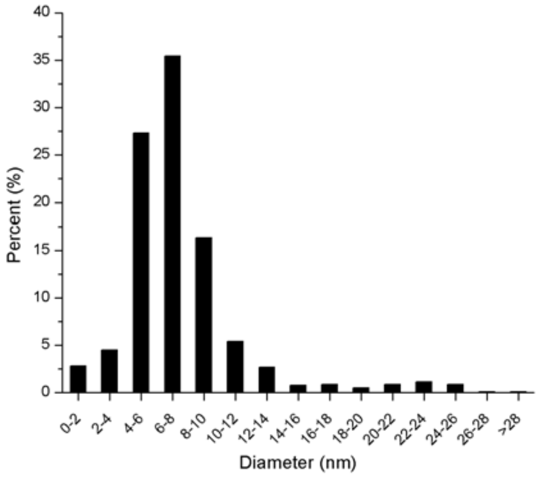

Fig. A2-2 *Example for the NPs size distribution*

A2.4 Influence of the NPs composition

Even in this research the same NPs density and heat capacity has been used for the LII model, in fact the composition change of NPs can influence the LII signal as well. Fig. A2-3 shows a comparison of the LII signal (694nm) decay time emitted by the pure carbon or iron solid particle with the same temperature 3500K at the beginning of the cool down process, where the reactor temperature is 650°C and the xylene solution is injected at 0.2 mL/min with a 1L/min argon gas flow, using the data in the article of Kock, B.F., et al. [267] and Michelsen, H., et al. [262]. And Fig. A2-4 shows the relation between the decay time and the NPs diameter under the presented experiment conditions. It could be seen that the iron solid particles have a relatively long decay time, thus for further research of the LII diagnostic on the NPs during CVD process, the influence of the NPs composition should also be considered, especially when the iron quantity is relatively high (in this study the ratio between iron/carbon mass is less than 0.02 in the ferrocene/xylene solution, as has been presented in chapter 2).

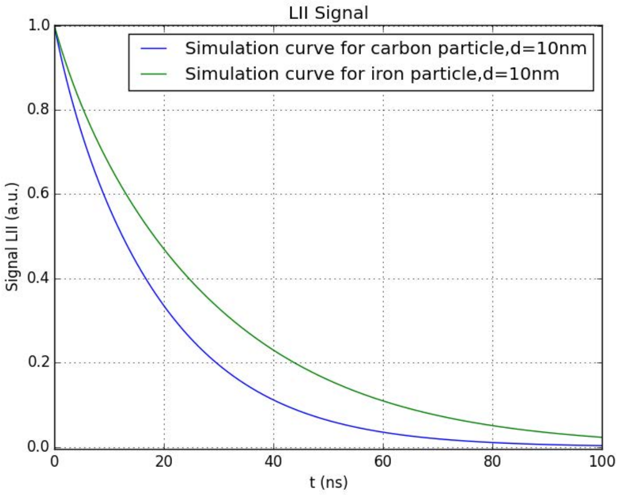

Fig. A2-3 *Comparison of the LII signal decay time for pure carbon and pure iron solid nanoparticles.*

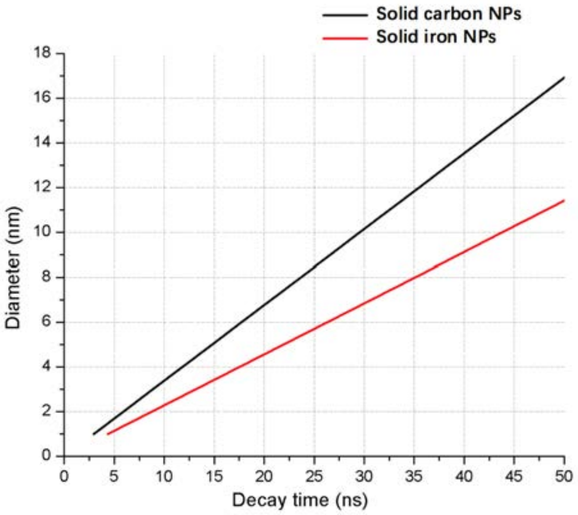

Fig. A2-4 *Relation between the decay time and the NPs diameter of pure solid carbon/iron nanoparticles*

References

1. Emsley, J., *Book Review: Nature's building blocks: an AZ guide to the elements/Oxford University Press, New York, 538 pp., 2002, ISBN 0-198-50341-5.* Astronomy, 2003. **31**(2): p. 87-88.
2. Patrick, J.W., *Porosity in carbons: characterization and applications*. 1995: Wiley.
3. Collin, G. *On the history of technical carbon*. in *CFI. Ceramic forum international*. 2000. Göller.
4. Harris, P., *On charcoal.* Interdisciplinary Science Reviews, 1999. **24**(4): p. 301-306.
5. O'connell, M.J., *Carbon nanotubes: properties and applications*. 2006: CRC press.
6. Bundy, F., et al., *The pressure-temperature phase and transformation diagram for carbon; updated through 1994.* Carbon, 1996. **34**(2): p. 141-153.
7. Harris, P.J.F., *Carbon nanotube science: synthesis, properties and applications*. 2009: Cambridge University Press.
8. Curl, R., *Health JR O'Brien SC C60: Buckminsterfullerene.* Nature, 1985. **318**: p. 162.
9. Kratschmer, W., et al., *Solid C60: a new form of carbon.* Nature, 1990. **347**: p. 27.
10. Iijima, S., *Helical microtubules of graphitic carbon.* nature, 1991. **354**(6348): p. 56-58.
11. Radushkevich, L. and V. Lukyanovich, *O strukture ugleroda, obrazujucegosja pri termiceskom razlozenii okisi ugleroda na zeleznom kontakte.* Zurn Fisic Chim, 1952. **26**(1): p. 88-95.
12. Monthioux, M. and V.L. Kuznetsov, *Who should be given the credit for the discovery of carbon nanotubes?* Carbon, 2006. **44**(9): p. 1621-1623.
13. Oberlin, A., M. Endo, and T. Koyama, *Filamentous growth of carbon through benzene decomposition.* Journal of crystal growth, 1976. **32**(3): p. 335-349.
14. Iijima, S. and T. Ichihashi, *Single-shell carbon nanotubes of 1-nm diameter.* 1993.
15. Bethune, D., et al., *Cobalt-catalysed growth of carbon nanotubes with single-atomic-layer walls.* 1993.
16. Zheng, L., et al., *Ultralong single-wall carbon nanotubes.* Nature materials, 2004. **3**(10): p. 673-676.
17. Wilder, J.W., et al., *Electronic structure of atomically resolved carbon nanotubes.* Nature, 1998. **391**(6662): p. 59-62.
18. Dichiara, A., *In situ diagnostics for the study of carbon nanotube growth mechanism by floating catalyst chemical vapor deposition for advanced composite applications.* 2012.

19. Saito, Y., et al., *Carbon nanocapsules and single‐layered nanotubes produced with platinum‐group metals (Ru, Rh, Pd, Os, Ir, Pt) by arc discharge.* Journal of applied physics, 1996. **80**(5): p. 3062-3067.
20. Ebbesen, T. and P. Ajayan, *Large-scale synthesis of carbon nanotubes.* Nature, 1992. **358**(6383): p. 220-222.
21. Ebbesen, T., et al., *Patterns in the bulk growth of carbon nanotubes.* Chemical Physics Letters, 1993. **209**(1): p. 83-90.
22. Taylor, G., et al., *Cathode deposits in fullerene formation—microstructural evidence for independent pathways of pyrolytic carbon and nanobody formation.* Journal of crystal growth, 1994. **135**(1-2): p. 157-164.
23. Zhao, X., et al., *Preparation of high-grade carbon nanotubes by hydrogen arc discharge.* Carbon, 1997. **35**(6): p. 775-781.
24. Wang, X., et al., *Carbon nanotubes synthesized in a hydrogen arc discharge.* Applied Physics Letters, 1995. **66**(18): p. 2430-2432.
25. Cui, S., et al., *Investigation on preparation of multiwalled carbon nanotubes by DC arc discharge under N 2 atmosphere.* Carbon, 2004. **42**(5): p. 931-939.
26. Yokomichi, H., et al., *Synthesis of carbon nanotubes by arc discharge in CF4 gas atmosphere.* Japanese journal of applied physics, 1998. **37**(12R): p. 6492.
27. Shimotani, K., et al., *New synthesis of multi-walled carbon nanotubes using an arc discharge technique under organic molecular atmospheres.* Applied Physics A, 2001. **73**(4): p. 451-454.
28. Zhu, H., et al., *Formation of carbon nanotubes in water by the electric-arc technique.* Chemical Physics Letters, 2002. **366**(5): p. 664-669.
29. Li, X., et al., *High-yield synthesis of multi-walled carbon nanotubes by water-protected arc discharge method.* Carbon, 2003. **41**(8): p. 1664-1666.
30. Sano, N., et al., *Pressure effects on nanotubes formation using the submerged arc in water method.* Chemical Physics Letters, 2003. **378**(1): p. 29-34.
31. Alexandrou, I., et al., *Structure of carbon onions and nanotubes formed by arc in liquids.* The Journal of chemical physics, 2004. **120**(2): p. 1055-1058.
32. Bera, D., et al., *Optoelectronically automated system for carbon nanotubes synthesis via arc-discharge in solution.* Review of scientific instruments, 2005. **76**(3): p. 033903.
33. Qiu, J., et al., *Formation of carbon nanotubes and encapsulated nanoparticles from coals with moderate ash contents.* Carbon, 1998. **36**(4): p. 465-467.
34. Qiu, J., et al., *Production of carbon nanotubes from coal.* Fuel processing technology, 2004. **85**(15): p. 1663-1670.
35. Guo, T., et al., *Catalytic growth of single-walled manotubes by laser vaporization.* Chemical physics letters, 1995. **243**(1): p. 49-54.
36. Yakobson, B.I. and R.E. Smalley, *Fullerene nanotubes: C 1,000,000 and beyond: Some unusual new molecules—long, hollow fibers with tantalizing electronic and mechanical properties—have joined diamonds and graphite in the carbon family.* American Scientist, 1997. **85**(4): p. 324-337.
37. Thess, A., et al., *Crystalline ropes of metallic carbon nanotubes.* Science, 1996. **273**(5274): p. 483.

38. Kokai, F., et al., *Growth dynamics of single-wall carbon nanotubes synthesized by CO2 laser vaporization.* The Journal of Physical Chemistry B, 1999. **103**(21): p. 4346-4351.
39. Li, W., et al., *Large-scale synthesis of aligned carbon nanotubes.* Science, 1996. **274**(5293): p. 1701-1703.
40. Lee, C.J., et al., *Temperature effect on the growth of carbon nanotubes using thermal chemical vapor deposition.* Chemical Physics Letters, 2001. **343**(1): p. 33-38.
41. Andrews, R., et al., *Continuous production of aligned carbon nanotubes: a step closer to commercial realization.* Chemical physics letters, 1999. **303**(5): p. 467-474.
42. Tessonnier, J.P. and D.S. Su, *Recent progress on the growth mechanism of carbon nanotubes: a review.* ChemSusChem, 2011. **4**(7): p. 824-847.
43. Prasek, J., et al., *Methods for carbon nanotubes synthesis—review.* Journal of Materials Chemistry, 2011. **21**(40): p. 15872-15884.
44. Meyyappan, M., *Carbon nanotubes: science and applications*. 2004: CRC press.
45. Teo, K.B., et al., *Catalytic synthesis of carbon nanotubes and nanofibers.* Encyclopedia of nanoscience and nanotechnology, 2003. **10**(1).
46. Merchan-Merchan, W., et al., *Combustion synthesis of carbon nanotubes and related nanostructures.* Progress in Energy and Combustion Science, 2010. **36**(6): p. 696-727.
47. Bower, C., et al., *Nucleation and growth of carbon nanotubes by microwave plasma chemical vapor deposition.* Applied Physics Letters, 2000. **77**(17): p. 2767-2769.
48. Flahaut, E., et al., *Synthesis of single-walled carbon nanotubes using binary (Fe, Co, Ni) alloy nanoparticles prepared in situ by the reduction of oxide solid solutions.* Chemical Physics Letters, 1999. **300**(1): p. 236-242.
49. Kong, J., A.M. Cassell, and H. Dai, *Chemical vapor deposition of methane for single-walled carbon nanotubes.* Chemical Physics Letters, 1998. **292**(4): p. 567-574.
50. Cassell, A.M., et al., *Large scale CVD synthesis of single-walled carbon nanotubes.* The Journal of Physical Chemistry B, 1999. **103**(31): p. 6484-6492.
51. Colomer, J.-F., et al., *Large-scale synthesis of single-wall carbon nanotubes by catalytic chemical vapor deposition (CCVD) method.* Chemical Physics Letters, 2000. **317**(1): p. 83-89.
52. Hafner, J.H., et al., *Catalytic growth of single-wall carbon nanotubes from metal particles.* Chemical Physics Letters, 1998. **296**(1): p. 195-202.
53. Che, G., et al., *Chemical vapor deposition based synthesis of carbon nanotubes and nanofibers using a template method.* Chemistry of Materials, 1998. **10**(1): p. 260-267.
54. Cheng, H., et al., *Large-scale and low-cost synthesis of single-walled carbon nanotubes by the catalytic pyrolysis of hydrocarbons.* Applied Physics Letters,

1998. **72**(25): p. 3282-3284.

55. Smith, D.K., D.C. Lee, and B.A. Korgel, *High yield multiwall carbon nanotube synthesis in supercritical fluids.* Chemistry of materials, 2006. **18**(14): p. 3356-3364.
56. Kumar, M. and Y. Ando, *Chemical Vapor Deposition of Carbon Nanotubes: A Review on Growth Mechanism and Mass Production.* Journal of Nanoscience and Nanotechnology, 2010. **10**(6): p. 3739-3758.
57. Nessim, G.D., et al., *Tuning of vertically-aligned carbon nanotube diameter and areal density through catalyst pre-treatment.* Nano letters, 2008. **8**(11): p. 3587-3593.
58. He, D. and J. Bai, *Acetylene‐Enhanced Growth of Carbon Nanotubes on Ceramic Microparticles for Multi‐Scale Hybrid Structures.* Chemical Vapor Deposition, 2011. **17**(4‐6): p. 98-106.
59. Mosquera, E., et al., *Characterization and hydrogen storage in multi-walled carbon nanotubes grown by aerosol-assisted CVD method.* Diamond and Related Materials, 2014. **43**: p. 66-71.
60. Wasel, W., et al., *Experimental characterization of the role of hydrogen in CVD synthesis of MWCNTs.* Carbon, 2007. **45**(4): p. 833-838.
61. Lebedeva, I.V., et al., *First-principles based kinetic modeling of effect of hydrogen on growth of carbon nanotubes.* Carbon, 2011. **49**(7): p. 2508-2521.
62. Castro, C., et al., *The role of hydrogen in the aerosol-assisted chemical vapor deposition process in producing thin and densely packed vertically aligned carbon nanotubes.* Carbon, 2013. **61**: p. 585-594.
63. Raney, J.R., A. Misra, and C. Daraio, *Tailoring the microstructure and mechanical properties of arrays of aligned multiwall carbon nanotubes by utilizing different hydrogen concentrations during synthesis.* Carbon, 2011. **49**(11): p. 3631-3638.
64. Zhang, G., et al., *Ultra-high-yield growth of vertical single-walled carbon nanotubes: Hidden roles of hydrogen and oxygen.* Proceedings of the National Academy of Sciences of the United States of America, 2005. **102**(45): p. 16141-16145.
65. In, J.B., et al., *Hidden role of trace gas impurities in chemical vapor deposition growth of vertically-aligned carbon nanotube arrays.* Applied Physics Letters, 2011. **98**(15): p. 153102.
66. de Heer, W.A. and D. Ugarte, *Carbon onions produced by heat treatment of carbon soot and their relation to the 217.5 nm interstellar absorption feature.* Chemical physics letters, 1993. **207**(4): p. 480-486.
67. Setlur, A., et al., *A promising pathway to make multiwalled carbon nanotubes.* Applied Physics Letters, 2000. **76**(21): p. 3008-3010.
68. Doherty, S. and R. Chang, *Synthesis of multiwalled carbon nanotubes from carbon black.* Applied physics letters, 2002. **81**(13): p. 2466-2468.
69. Buchholz, D., S. Doherty, and R. Chang, *Mechanism for the growth of multiwalled carbon-nanotubes from carbon black.* Carbon, 2003. **41**(8): p. 1625-1634.

70. Doherty, S., D. Buchholz, and R. Chang, *Semi-continuous production of multiwalled carbon nanotubes using magnetic field assisted arc furnace.* Carbon, 2006. **44**(8): p. 1511-1517.
71. Harris, P.J., *Ultrathin graphitic structures and carbon nanotubes in a purified synthetic graphite.* Journal of Physics: Condensed Matter, 2009. **21**(35): p. 355009.
72. Gore, J.P. and A. Sane, *Flame synthesis of carbon nanotubes.* Carbon Nanotubes: Synthesis, Characterization, Applications, InTech, 2011.
73. Liu, Y.C., B.M. Sun, and Z.Y. Ding. *Influence analysis of sampling time for synthesis of carbon nanotubes in the V-type pyrolysis flame*. in *Advanced Materials Research*. 2011. Trans Tech Publ.
74. Vander Wal, R.L. and L.J. Hall, *Flame synthesis of Fe catalyzed single-walled carbon nanotubes and Ni catalyzed nanofibers: growth mechanisms and consequences.* Chemical physics letters, 2001. **349**(3): p. 178-184.
75. Hu, W.-C. and T.-H. Lin, *Ethanol flame synthesis of carbon nanotubes in deficient oxygen environments.* Nanotechnology, 2016. **27**(16): p. 165602.
76. Tse, S.D., *Novel Flame-Based Synthesis of Nanowires for Multifunctional Application*. 2015, DTIC Document.
77. Hsu, W., et al., *Electrolytic formation of carbon nanostructures.* Chemical Physics Letters, 1996. **262**(1): p. 161-166.
78. Hsu, W., et al., *Condensed-phase nanotubes.* Nature, 1995. **377**(6551): p. 687-687.
79. Laplaze, D., et al., *Carbon nanotubes: dynamics of synthesis processes.* Carbon, 2002. **40**(10): p. 1621-1634.
80. Saito, R., et al., *Electronic structure of chiral graphene tubules.* Applied physics letters, 1992. **60**(18): p. 2204-2206.
81. Dresselhaus, M., G. Dresselhaus, and R. Saito, *Physics of carbon nanotubes.* Carbon, 1995. **33**(7): p. 883-891.
82. Dresselhaus, M.S., G. Dresselhaus, and P.C. Eklund, *Science of fullerenes and carbon nanotubes: their properties and applications*. 1996: Academic press.
83. Blase, X., et al., *Hybridization effects and metallicity in small radius carbon nanotubes.* Physical review letters, 1994. **72**(12): p. 1878.
84. Kane, C.L. and E. Mele, *Size, shape, and low energy electronic structure of carbon nanotubes.* Physical Review Letters, 1997. **78**(10): p. 1932.
85. Datta, S., *Electronic transport in mesoscopic systems*. 1997: Cambridge university press.
86. Martel, R., et al., *Single-and multi-wall carbon nanotube field-effect transistors.* Applied Physics Letters, 1998. **73**(17): p. 2447-2449.
87. Langer, L., et al., *Quantum transport in a multiwalled carbon nanotube.* Physical review letters, 1996. **76**(3): p. 479.
88. Ebbesen, T., et al., *Electrical-conductivity of individual carbon nanotubes.* Nature, 1996. **382**(6586): p. 54-56.
89. Collins, P.G., et al., *Current saturation and electrical breakdown in multiwalled carbon nanotubes.* Physical review letters, 2001. **86**(14): p. 3128.

90. Wang, N., et al., *Materials science: Single-walled 4 Å carbon nanotube arrays.* Nature, 2000. **408**(6808): p. 50-51.
91. Tang, Z., et al., *Superconductivity in 4 angstrom single-walled carbon nanotubes.* Science, 2001. **292**(5526): p. 2462-2465.
92. Kociak, M., et al., *Superconductivity in ropes of single-walled carbon nanotubes.* Physical Review Letters, 2001. **86**(11): p. 2416.
93. Takesue, I., et al., *Superconductivity in entirely end-bonded multiwalled carbon nanotubes.* Physical review letters, 2006. **96**(5): p. 057001.
94. Lu, J.P., *Elastic properties of carbon nanotubes and nanoropes.* Physical Review Letters, 1997. **79**(7): p. 1297.
95. Hernandez, E., et al., *Elastic properties of C and B x C y N z composite nanotubes.* Physical Review Letters, 1998. **80**(20): p. 4502.
96. Yao, N. and V. Lordi, *Young's modulus of single-walled carbon nanotubes.* Journal of Applied Physics, 1998. **84**(4): p. 1939-1943.
97. Govindjee, S. and J.L. Sackman, *On the use of continuum mechanics to estimate the properties of nanotubes.* Solid State Communications, 1999. **110**(4): p. 227-230.
98. Ozaki, T., Y. Iwasa, and T. Mitani, *Stiffness of single-walled carbon nanotubes under large strain.* Physical Review Letters, 2000. **84**(8): p. 1712.
99. Van Lier, G., et al., *Ab initio study of the elastic properties of single-walled carbon nanotubes and graphene.* Chemical Physics Letters, 2000. **326**(1): p. 181-185.
100. Xin, Z., Z. Jianjun, and O.-Y. Zhong-Can, *Strain energy and Young's modulus of single-wall carbon nanotubes calculated from electronic energy-band theory.* Physical Review B, 2000. **62**(20): p. 13692.
101. Nardelli, M.B., B.I. Yakobson, and J. Bernholc, *Mechanism of strain release in carbon nanotubes.* Physical review B, 1998. **57**(8): p. R4277.
102. Zhao, Q., M.B. Nardelli, and J. Bernholc, *Ultimate strength of carbon nanotubes: a theoretical study.* Physical Review B, 2002. **65**(14): p. 144105.
103. Liew, K., X. He, and C. Wong, *On the study of elastic and plastic properties of multi-walled carbon nanotubes under axial tension using molecular dynamics simulation.* Acta Materialia, 2004. **52**(9): p. 2521-2527.
104. Poncharal, P., et al., *Electrostatic deflections and electromechanical resonances of carbon nanotubes.* Science, 1999. **283**(5407): p. 1513-1516.
105. Yakobson, B.I. and P. Avouris, *Mechanical properties of carbon nanotubes*, in *Carbon nanotubes*. 2001, Springer. p. 287-327.
106. Cao, A., et al., *Super-compressible foamlike carbon nanotube films.* Science, 2005. **310**(5752): p. 1307-1310.
107. Iijima, S., et al., *Structural flexibility of carbon nanotubes.* The Journal of chemical physics, 1996. **104**(5): p. 2089-2092.
108. Treacy, M.J., T. Ebbesen, and J. Gibson, *Exceptionally high Young's modulus observed for individual carbon nanotubes.* 1996.
109. Hertel, T., R. Martel, and P. Avouris, *Manipulation of individual carbon nanotubes and their interaction with surfaces.* The Journal of Physical

Chemistry B, 1998. **102**(6): p. 910-915.

110. Salvetat, J.-P., et al., *Elastic modulus of ordered and disordered multiwalled carbon nanotubes.* Advanced Materials, 1999. **11**(2): p. 161-165.
111. Guhados, G., et al., *Simultaneous measurement of Young's and shear moduli of multiwalled carbon nanotubes using atomic force microscopy.* Journal of applied physics, 2007. **101**(3): p. 033514.
112. Cumings, J. and A. Zettl, *Low-friction nanoscale linear bearing realized from multiwall carbon nanotubes.* Science, 2000. **289**(5479): p. 602-604.
113. Yu, M.-F., et al., *Strength and breaking mechanism of multiwalled carbon nanotubes under tensile load.* Science, 2000. **287**(5453): p. 637-640.
114. Ruoff, R.S., *Time, temperature, and load: The flaws of carbon nanotubes.* Proceedings of the National Academy of Sciences, 2006. **103**(18): p. 6779-6780.
115. Demczyk, B., et al., *Direct mechanical measurement of the tensile strength and elastic modulus of multiwalled carbon nanotubes.* Materials Science and Engineering: A, 2002. **334**(1): p. 173-178.
116. Salvetat, J.-P., et al., *Elastic and shear moduli of single-walled carbon nanotube ropes.* Physical review letters, 1999. **82**(5): p. 944.
117. Tombler, T.W., et al., *Reversible electromechanical characteristics of carbon nanotubes under local-probe manipulation.* Nature, 2000. **405**(6788): p. 769-772.
118. Yu, M.-F., et al., *Tensile loading of ropes of single wall carbon nanotubes and their mechanical properties.* Physical review letters, 2000. **84**(24): p. 5552.
119. Laby, T., *Tables of Physical and Chemical Constants*. 1995, Longman, Essex.
120. Popov, V.N., *Carbon nanotubes: properties and application.* Materials Science and Engineering: R: Reports, 2004. **43**(3): p. 61-102.
121. Pop, E., et al., *Thermal conductance of an individual single-wall carbon nanotube above room temperature.* Nano letters, 2006. **6**(1): p. 96-100.
122. Kim, P., et al., *Thermal transport measurements of individual multiwalled nanotubes.* Physical review letters, 2001. **87**(21): p. 215502.
123. Zhang, Q., et al., *Thermal conductivity of multiwalled carbon nanotubes.* Physical Review B, 2002. **66**(16): p. 165440.
124. Lambin, P., et al., *Structural and electronic properties of bent carbon nanotubes.* Chemical Physics Letters, 1995. **245**(1): p. 85-89.
125. Chico, L., et al., *Pure carbon nanoscale devices: nanotube heterojunctions.* Physical Review Letters, 1996. **76**(6): p. 971.
126. Yao, Z., et al., *Carbon nanotube intramolecular junctions.* Nature, 1999. **402**(6759): p. 273-276.
127. Zhou, C., et al., *Modulated chemical doping of individual carbon nanotubes.* Science, 2000. **290**(5496): p. 1552-1555.
128. Lee, J.U., P. Gipp, and C. Heller, *Carbon nanotube pn junction diodes.* Applied Physics Letters, 2004. **85**: p. 145.
129. Tans, S.J., A.R. Verschueren, and C. Dekker, *Room-temperature transistor based on a single carbon nanotube.* Nature, 1998. **393**(6680): p. 49-52.

130. Martel, R., et al., *Carbon nanotube field effect transistors for logic applications.* Interface, 2001. **2500**: p. 730.

131. Seidel, R., et al., *High-current nanotube transistors.* Nano Letters, 2004. **4**(5): p. 831-834.

132. Keren, K., et al., *DNA-templated carbon nanotube field-effect transistor.* Science, 2003. **302**(5649): p. 1380-1382.

133. Collins, P.G., et al., *Extreme oxygen sensitivity of electronic properties of carbon nanotubes.* science, 2000. **287**(5459): p. 1801-1804.

134. De Heer, W.A., A. Chatelain, and D. Ugarte, *A carbon nanotube field-emission electron source.* Science, 1995. **270**(5239): p. 1179-1180.

135. Rinzler, A., et al., *Unraveling nanotubes: field emission from an atomic wire.* Science, 1995. **269**(5230): p. 1550.

136. Saito, Y. and S. Uemura, *Field emission from carbon nanotubes and its application to electron sources.* Carbon, 2000. **38**(2): p. 169-182.

137. Choi, W., et al., *Fully sealed, high-brightness carbon-nanotube field-emission display.* Applied physics letters, 1999. **75**(20): p. 3129-3131.

138. Coll, B., et al., *Nano‐emissive display technology for large‐area HDTV.* Journal of the Society for Information Display, 2006. **14**(5): p. 477-485.

139. Endo, M., M.S. Strano, and P.M. Ajayan, *Potential applications of carbon nanotubes*, in *Carbon nanotubes*. 2007, Springer. p. 13-62.

140. Zhang, Q., et al., *The road for nanomaterials industry: a review of carbon nanotube production, post-treatment, and bulk applications for composites and energy storage.* Small, 2013. **9**(8): p. 1237-65.

141. Endo, M., et al., *Recent development of carbon materials for Li ion batteries.* Carbon, 2000. **38**(2): p. 183-197.

142. Eom, J., et al., *Electrochemical insertion of lithium into multiwalled carbon nanotube/silicon composites produced by ballmilling.* Journal of The Electrochemical Society, 2006. **153**(9): p. A1678-A1684.

143. Baughman, R.H., A.A. Zakhidov, and W.A. de Heer, *Carbon nanotubes--the route toward applications.* science, 2002. **297**(5582): p. 787-792.

144. Niu, C., et al., *High power electrochemical capacitors based on carbon nanotube electrodes.* Applied Physics Letters, 1997. **70**(11): p. 1480-1482.

145. Zheng, Y., M. Zhang, and P. Gao, *Preparation and electrochemical properties of multiwalled carbon nanotubes–nickel oxide porous composite for supercapacitors.* Materials research bulletin, 2007. **42**(9): p. 1740-1747.

146. De Volder, M.F., et al., *Carbon nanotubes: present and future commercial applications.* Science, 2013. **339**(6119): p. 535-539.

147. Landi, B., et al., *CdSe quantum dot-single wall carbon nanotube complexes for polymeric solar cells.* Solar Energy Materials and Solar Cells, 2005. **87**(1): p. 733-746.

148. Baughman, R.H., et al., *Carbon nanotube actuators.* Science, 1999. **284**(5418): p. 1340-1344.

149. Hughes, M. and G.M. Spinks, *Multiwalled carbon nanotube actuators.* Advanced Materials, 2005. **17**(4): p. 443-446.

150. Hill, F., T. Havel, and C. Livermore, *Modeling mechanical energy storage in springs based on carbon nanotubes.* Nanotechnology, 2009. **20**(25): p. 255704.
151. Strus, M.C., et al., *Imaging artefacts in atomic force microscopy with carbon nanotube tips.* Nanotechnology, 2005. **16**(11): p. 2482.
152. Romero, H.E., et al., *Atom collision-induced resistivity of carbon nanotubes.* Science, 2005. **307**(5706): p. 89-93.
153. Star, A., et al., *Gas sensor array based on metal-decorated carbon nanotubes.* The Journal of Physical Chemistry B, 2006. **110**(42): p. 21014-21020.
154. Lu, Y., et al., *Room temperature methane detection using palladium loaded single-walled carbon nanotube sensors.* Chemical Physics Letters, 2004. **391**(4): p. 344-348.
155. Kong, J., M.G. Chapline, and H. Dai, *Functionalized carbon nanotubes for molecular hydrogen sensors.* Advanced Materials, 2001. **13**(18): p. 1384.
156. Kuzmych, O., B.L. Allen, and A. Star, *Carbon nanotube sensors for exhaled breath components.* Nanotechnology, 2007. **18**(37): p. 375502.
157. Qi, P., et al., *Toward large arrays of multiplex functionalized carbon nanotube sensors for highly sensitive and selective molecular detection.* Nano letters, 2003. **3**(3): p. 347-351.
158. Bekyarova, E., et al., *Chemically functionalized single-walled carbon nanotubes as ammonia sensors.* The Journal of Physical Chemistry B, 2004. **108**(51): p. 19717-19720.
159. Feng, X., et al., *Sensitivity of ammonia interaction with single-walled carbon nanotube bundles to the presence of defect sites and functionalities.* Journal of the American Chemical Society, 2005. **127**(30): p. 10533-10538.
160. Kong, J., et al., *Nanotube molecular wires as chemical sensors.* Science, 2000. **287**(5453): p. 622-625.
161. Balasubramanian, K. and M. Burghard, *Biosensors based on carbon nanotubes.* Analytical and bioanalytical chemistry, 2006. **385**(3): p. 452-468.
162. Wood, J.R. and H.D. Wagner, *Single-wall carbon nanotubes as molecular pressure sensors.* Applied Physics Letters, 2000. **76**(20): p. 2883-2885.
163. Zhao, Q., M.D. Frogley, and H.D. Wagner, *Direction-sensitive strain-mapping with carbon nanotube sensors.* Composites Science and Technology, 2002. **62**(1): p. 147-150.
164. Ghosh, S., A. Sood, and N. Kumar, *Carbon nanotube flow sensors.* Science, 2003. **299**(5609): p. 1042-1044.
165. Vigolo, B., et al., *Macroscopic fibers and ribbons of oriented carbon nanotubes.* Science, 2000. **290**(5495): p. 1331-1334.
166. Dalton, A.B., et al., *Super-tough carbon-nanotube fibres.* Nature, 2003. **423**(6941): p. 703-703.
167. Zhang, M., K.R. Atkinson, and R.H. Baughman, *Multifunctional carbon nanotube yarns by downsizing an ancient technology.* Science, 2004. **306**(5700): p. 1358-1361.
168. Ramakrishna, S., et al., *An introduction to electrospinning and nanofibers*. Vol.

90. 2005: World Scientific.
169. Andrews, R., et al., *Multiwall carbon nanotubes: synthesis and application.* Accounts of Chemical Research, 2002. **35**(12): p. 1008-1017.
170. Haggenmueller, R., et al., *Production and characterization of polymer nanocomposites with highly aligned single-walled carbon nanotubes.* Journal of nanoscience and nanotechnology, 2003. **3**(1-2): p. 105-110.
171. Kashiwagi, T., et al., *Relationship between dispersion metric and properties of PMMA/SWNT nanocomposites.* Polymer, 2007. **48**(16): p. 4855-4866.
172. McNally, T., et al., *Polyethylene multiwalled carbon nanotube composites.* Polymer, 2005. **46**(19): p. 8222-8232.
173. Zhang, Q., et al., *Low percolation threshold in single-walled carbon nanotube/high density polyethylene composites prepared by melt processing technique.* Carbon, 2006. **44**(4): p. 778-785.
174. Pötschke, P., A.R. Bhattacharyya, and A. Janke, *Melt mixing of polycarbonate with multiwalled carbon nanotubes: microscopic studies on the state of dispersion.* European Polymer Journal, 2004. **40**(1): p. 137-148.
175. Lin, B., U. Sundararaj, and P. Pötschke, *Melt Mixing of Polycarbonate with Multi‐Walled Carbon Nanotubes in Miniature Mixers.* Macromolecular Materials and Engineering, 2006. **291**(3): p. 227-238.
176. Handge, U. and P. Pötschke, *Deformation and orientation during shear and elongation of a polycarbonate/carbon nanotubes composite in the melt.* Rheologica Acta, 2007. **46**(6): p. 889-898.
177. Satapathy, B.K., et al., *Tough-to-brittle transition in multiwalled carbon nanotube (MWNT)/polycarbonate nanocomposites.* Composites science and technology, 2007. **67**(5): p. 867-879.
178. Ma, P.-C., et al., *Dispersion and functionalization of carbon nanotubes for polymer-based nanocomposites: a review.* Composites Part A: Applied Science and Manufacturing, 2010. **41**(10): p. 1345-1367.
179. Cochet, M., et al., *Synthesis of a new polyaniline/nanotube composite: "in-situ" polymerisation and charge transfer through site-selective interaction.* Chemical Communications, 2001(16): p. 1450-1451.
180. Kim, S.T., H.J. Choi, and S.M. Hong, *Bulk polymerized polystyrene in the presence of multiwalled carbon nanotubes.* Colloid and polymer science, 2007. **285**(5): p. 593-598.
181. Jin Yoo, H., et al., *Polyurethane‐Carbon Nanotube Nanocomposites Prepared by In‐Situ Polymerization with Electroactive Shape Memory.* Journal of Macromolecular Science, Part B, 2006. **45**(4): p. 441-451.
182. Wu, T.M. and S.H. Lin, *Synthesis, characterization, and electrical properties of polypyrrole/multiwalled carbon nanotube composites.* Journal of Polymer Science Part A: Polymer Chemistry, 2006. **44**(21): p. 6449-6457.
183. Kang, M., S.J. Myung, and H.-J. Jin, *Nylon 610 and carbon nanotube composite by in situ interfacial polymerization.* Polymer, 2006. **47**(11): p. 3961-3966.
184. Saeed, K., et al., *In situ polymerization of multi-walled carbon*

nanotube/nylon-6 nanocomposites and their electrospun nanofibers. Nanoscale research letters, 2009. **4**(1): p. 39-46.

185. Moniruzzaman, M. and K.I. Winey, *Polymer nanocomposites containing carbon nanotubes.* Macromolecules, 2006. **39**(16): p. 5194-5205.
186. Grossiord, N., et al., *Toolbox for dispersing carbon nanotubes into polymers to get conductive nanocomposites.* Chemistry of materials, 2006. **18**(5): p. 1089-1099.
187. Du, J., J. Bai, and H. Cheng, *The present status and key problems of carbon nanotube based polymer composites.* Express Polymer Letters, 2007. **1**(5): p. 253-273.
188. Li, F., et al., *Tensile strength of single-walled carbon nanotubes directly measured from their macroscopic ropes.* Applied physics letters, 2000. **77**(20): p. 3161-3163.
189. Pichot, V., et al., *Structural and mechanical properties of single-wall carbon nanotube fibers.* Physical Review B, 2006. **74**(24): p. 245416.
190. Moniruzzaman, M., et al., *Tuning the mechanical properties of SWNT/Nylon 6, 10 composites with flexible spacers at the interface.* Nano letters, 2007. **7**(5): p. 1178-1185.
191. Aneli, J., L. Khananasvili, and G.E. Zaikov, *Structuring and conductivity of polymer composites*. 1998: Nova Science Publishers.
192. Sham, M.L., et al., *Cleaning and functionalization of polymer surfaces and nanoscale carbon fillers by UV/ozone treatment: a review.* Journal of composite materials, 2009. **43**(14): p. 1537-1564.
193. Choi, E., et al., *Enhancement of thermal and electrical properties of carbon nanotube polymer composites by magnetic field processing.* Journal of Applied physics, 2003. **94**(9): p. 6034-6039.
194. Sandler, J., et al., *Ultra-low electrical percolation threshold in carbon-nanotube-epoxy composites.* Polymer, 2003. **44**(19): p. 5893-5899.
195. Li, J., et al., *Correlations between percolation threshold, dispersion state, and aspect ratio of carbon nanotubes.* Advanced Functional Materials, 2007. **17**(16): p. 3207-3215.
196. Bryning, M.B., et al., *Very Low Conductivity Threshold in Bulk Isotropic Single‐Walled Carbon Nanotube–Epoxy Composites.* Advanced materials, 2005. **17**(9): p. 1186-1191.
197. Ping, Z. and C. Wang, *Polymer world*. 2001, Shanghai: Fudan University Press.
198. Zhang, W., A.A. Dehghani-Sanij, and R.S. Blackburn, *Carbon based conductive polymer composites.* Journal of materials science, 2007. **42**(10): p. 3408-3418.
199. Mo, C.B., et al., *Fabrication of carbon nanotube reinforced alumina matrix nanocomposite by sol–gel process.* Materials Science and Engineering: A, 2005. **395**(1): p. 124-128.
200. Seeger, T., et al., *Evolution of multiwalled carbon-nanotube/SiO2 composites via laser treatment.* Nanotechnology, 2003. **14**(2): p. 184.

201. Vincent, P., et al., *Inclusion of carbon nanotubes in a TiO 2 sol–gel matrix.* Journal of non-crystalline solids, 2002. **311**(2): p. 130-137.
202. Sakamoto, J.S. and B. Dunn, *Vanadium oxide-carbon nanotube composite electrodes for use in secondary lithium batteries.* Journal of the Electrochemical Society, 2002. **149**(1): p. A26-A30.
203. White, A.A., S.M. Best, and I.A. Kinloch, *Hydroxyapatite–carbon nanotube composites for biomedical applications: a review.* International Journal of Applied Ceramic Technology, 2007. **4**(1): p. 1-13.
204. Ma, R., et al., *Processing and properties of carbon nanotubes–nano-SiC ceramic.* Journal of Materials Science, 1998. **33**(21): p. 5243-5246.
205. Andrews, R., et al., *Nanotube composite carbon fibers.* Applied Physics Letters, 1999. **75**(9): p. 1329-1331.
206. Boskovic, B., et al., *Low temperature synthesis of carbon nanofibres on carbon fibre matrices.* Carbon, 2005. **43**(13): p. 2643-2648.
207. Endo, M., et al., *Vapor-grown carbon fibers (VGCFs): basic properties and their battery applications.* Carbon, 2001. **39**(9): p. 1287-1297.
208. Endo, M., T. Hayashi, and Y.-A. Kim, *Large-scale production of carbon nanotubes and their applications.* Pure and applied chemistry, 2006. **78**(9): p. 1703-1713.
209. Kuzumaki, T., et al., *Processing of carbon nanotube reinforced aluminum composite.* Journal of Materials Research, 1998. **13**(09): p. 2445-2449.
210. Kuzumaki, T., et al., *Mechanical characteristics and preparation of carbon nanotube fiber‐reinforced Ti composite.* Advanced Engineering Materials, 2000. **2**(7): p. 416-418.
211. Goh, C., et al. *Effect of fabrication techniques on the properties of carbon nanotubes reinforced magnesium.* in *Solid State Phenomena*. 2006. Trans Tech Publ.
212. Baker, R., et al., *Formation of filamentous carbon from iron, cobalt and chromium catalyzed decomposition of acetylene.* Journal of catalysis, 1973. **30**(1): p. 86-95.
213. Dai, H., *Nanotube growth and characterization*, in *Carbon Nanotubes*. 2001, Springer. p. 29-53.
214. Chhowalla, M., et al., *Growth process conditions of vertically aligned carbon nanotubes using plasma enhanced chemical vapor deposition.* Journal of Applied Physics, 2001. **90**(10): p. 5308-5317.
215. Li, J., et al., *Highly-ordered carbon nanotube arrays for electronics applications.* Applied physics letters, 1999. **75**(3): p. 367-369.
216. Sinnott, S., et al., *Model of carbon nanotube growth through chemical vapor deposition.* Chemical Physics Letters, 1999. **315**(1): p. 25-30.
217. Tibbetts, G.G., *Why are carbon filaments tubular?* Journal of crystal growth, 1984. **66**(3): p. 632-638.
218. Mei, Q. and K. Lu, *Melting and superheating of crystalline solids: From bulk to nanocrystals.* Progress in Materials Science, 2007. **52**(8): p. 1175-1262.
219. Moisala, A., A.G. Nasibulin, and E.I. Kauppinen, *The role of metal*

nanoparticles in the catalytic production of single-walled carbon nanotubes—a review. Journal of Physics: condensed matter, 2003. **15**(42): p. S3011.

220. Baker, R., et al., *Effect of the surface state of iron on filamentous carbon formation.* Journal of catalysis, 1982. **77**(1): p. 74-84.
221. Audier, M., P. Bowen, and W. Jones, *Electron microscopic and mössbauer study of the iron carbides θ-Fe 3 C and X-Fe 5 C 2 formed during the disproportionation of CO.* Journal of crystal growth, 1983. **64**(2): p. 291-296.
222. Yang, K. and R. Yang, *The accelerating and retarding effects of hydrogen on carbon deposition on metal surfaces.* Carbon, 1986. **24**(6): p. 687-693.
223. Du, G., et al., *Particle-wire-tube mechanism for carbon nanotube evolution.* Journal of the American Chemical Society, 2006. **128**(48): p. 15405-15414.
224. Kwon, Y.-K., et al., *Morphology and stability of growing multiwall carbon nanotubes.* Physical review letters, 1997. **79**(11): p. 2065.
225. Deng, W.-Q., X. Xu, and W.A. Goddard, *A two-stage mechanism of bimetallic catalyzed growth of single-walled carbon nanotubes.* Nano letters, 2004. **4**(12): p. 2331-2335.
226. Hong, G., et al., *Controlling the growth of single-walled carbon nanotubes on surfaces using metal and non-metal catalysts.* Carbon, 2012. **50**(6): p. 2067-2082.
227. Xu, X., et al., *Continuous synthesis of carbon nanotubes using a metal-free catalyst by CVD.* Materials Chemistry and Physics, 2012. **133**(1): p. 95-102.
228. Khavrus, V.O., et al., *Conditions of Simultaneous Growth and Separation of Single- and Multiwalled Carbon Nanotubes.* The Journal of Physical Chemistry C, 2010. **114**(2): p. 843-848.
229. Grobert, N., et al., *Enhanced magnetic coercivities in Fe nanowires.* Applied Physics Letters, 1999. **75**(21): p. 3363.
230. Cao, A., et al., *Macroscopic three-dimensional arrays of Fe nanoparticles supported in aligned carbon nanotubes.* The Journal of Physical Chemistry B, 2001. **105**(48): p. 11937-11940.
231. Grobert, N., et al., *Alloy nanowires: Invar inside carbon nanotubes.* Chemical Communications, 2001(5): p. 471-472.
232. Zhang, X., et al., *Rapid growth of well-aligned carbon nanotube arrays.* Chemical Physics Letters, 2002. **362**(3): p. 285-290.
233. Elias, A., et al., *Production and characterization of single-crystal FeCo nanowires inside carbon nanotubes.* Nano letters, 2005. **5**(3): p. 467-472.
234. Xiang, R., et al., *Encapsulation, compensation, and substitution of catalyst particles during continuous growth of carbon nanotubes.* Advanced Materials, 2007. **19**(17): p. 2360-2363.
235. Mattevi, C., et al., *In-situ X-ray photoelectron spectroscopy study of catalyst−support interactions and growth of carbon nanotube forests.* The Journal of Physical Chemistry C, 2008. **112**(32): p. 12207-12213.
236. Su, M., et al., *Lattice-oriented growth of single-walled carbon nanotubes.* The Journal of Physical Chemistry B, 2000. **104**(28): p. 6505-6508.

237. Uchino, T., et al., *Metal catalyst-free low-temperature carbon nanotube growth on SiGe islands.* Applied Physics Letters, 2005. **86**(23): p. 233110.

238. Sui, Y., et al., *Growth of carbon nanotubes and nanofibres in porous anodic alumina film.* Carbon, 2002. **40**(7): p. 1011-1016.

239. Helveg, S., et al., *Atomic-scale imaging of carbon nanofibre growth.* Nature, 2004. **427**(6973): p. 426-429.

240. Zhu, H., et al., *Atomic‐Resolution Imaging of the Nucleation Points of Single‐Walled Carbon Nanotubes.* Small, 2005. **1**(12): p. 1180-1183.

241. Hofmann, S., et al., *In situ observations of catalyst dynamics during surface-bound carbon nanotube nucleation.* Nano letters, 2007. **7**(3): p. 602-608.

242. Ohta, Y., et al., *Density-functional tight-binding molecular dynamics simulations of SWCNT growth by surface carbon diffusion on an iron cluster.* Carbon, 2009. **47**(5): p. 1270-1275.

243. Rodríguez-Manzo, J.A., et al., *In situ nucleation of carbon nanotubes by the injection of carbon atoms into metal particles.* Nature nanotechnology, 2007. **2**(5): p. 307-311.

244. Reich, S., L. Li, and J. Robertson, *Structure and formation energy of carbon nanotube caps.* Physical Review B, 2005. **72**(16): p. 165423.

245. Reich, S., L. Li, and J. Robertson, *Control the chirality of carbon nanotubes by epitaxial growth.* Chemical physics letters, 2006. **421**(4): p. 469-472.

246. Dichiara, A.B., et al., *Effective synergistic effect of Al 2 O 3 and SiC microparticles on the growth of carbon nanotubes and their application in high dielectric permittivity polymer composites.* Journal of Materials Chemistry A, 2014. **2**(21): p. 7980-7987.

247. Dichiara, A.B., S.F. Harlander, and R.E. Rogers, *Fixed bed adsorption of diquat dibromide from aqueous solution using carbon nanotubes.* RSC Advances, 2015. **5**(76): p. 61508-61512.

248. Ihsanullah, et al., *Heavy metal removal from aqueous solution by advanced carbon nanotubes: Critical review of adsorption applications.* Separation and Purification Technology, 2016. **157**: p. 141-161.

249. Li, W., A. Dichiara, and J. Bai, *Carbon nanotube–graphene nanoplatelet hybrids as high-performance multifunctional reinforcements in epoxy composites.* Composites Science and Technology, 2013. **74**: p. 221-227.

250. Mittal, G., et al., *A review on carbon nanotubes and graphene as fillers in reinforced polymer nanocomposites.* Journal of Industrial and Engineering Chemistry, 2015. **21**: p. 11-25.

251. Jourdain, V. and C. Bichara, *Current understanding of the growth of carbon nanotubes in catalytic chemical vapour deposition.* Carbon, 2013. **58**: p. 2-39.

252. He, D., et al., *Growth of carbon nanotubes in six orthogonal directions on spherical alumina microparticles.* Carbon, 2011. **49**(7): p. 2273-2286.

253. Ci, L., et al., *Crystallization behavior of the amorphous carbon nanotubes prepared by the CVD method.* Journal of Crystal Growth, 2001. **233**(4): p. 823-828.

254. Kuo, D.-H. and M.-Y. Su, *The effects of hydrogen and temperature on the growth and microstructure of carbon nanotubes obtained by the Fe (CO) 5 gas-phase-catalytic chemical vapor deposition.* Surface and Coatings Technology, 2007. **201**(22): p. 9172-9178.

255. Weeks, R. and W. Duley, *Aerosol‐particle sizes from light emission during excitation by TEA CO2 laser pulses.* Journal of Applied physics, 1974. **45**(10): p. 4661-4662.

256. Eckbreth, A.C., *Effects of laser‐modulated particulate incandescence on Raman scattering diagnostics.* Journal of Applied Physics, 1977. **48**(11): p. 4473-4479.

257. Melton, L.A., *Soot diagnostics based on laser heating.* Applied optics, 1984. **23**(13): p. 2201-2208.

258. Will, S., S. Schraml, and A. Leipertz, *Two-dimensional soot-particle sizing by time-resolved laser-induced incandescence.* Optics letters, 1995. **20**(22): p. 2342-2344.

259. Roth, P. and A. Filippov, *In situ ultrafine particle sizing by a combination of pulsed laser heatup and particle thermal emission.* Journal of aerosol science, 1996. **27**(1): p. 95-104.

260. Vander Wal, R.L. and M.Y. Choi, *Pulsed laser heating of soot: morphological changes.* Carbon, 1999. **37**(2): p. 231-239.

261. Vander Wal, R.L., et al., *Application of laser-induced incandescence to the detection of carbon nanotubes and carbon nanofibers.* Applied optics, 2002. **41**(27): p. 5678-5690.

262. Michelsen, H., et al., *Modeling laser-induced incandescence of soot: a summary and comparison of LII models.* Applied physics B, 2007. **87**(3): p. 503-521.

263. Vander Wal, R.L., T.M. Ticich, and A.B. Stephens, *Can soot primary particle size be determined using laser-induced incandescence?* Combustion and flame, 1999. **116**(1): p. 291-296.

264. Schulz, C., et al., *Laser-induced incandescence: recent trends and current questions.* Applied Physics B, 2006. **83**(3): p. 333-354.

265. Michelsen, H.A., et al., *Time-resolved laser-induced incandescence of soot: the influence of experimental factors and microphysical mechanisms.* Applied optics, 2003. **42**(27): p. 5577-5590.

266. Michelsen, H., et al., *Modeling laser-induced incandescence of soot: Enthalpy changes during sublimation, conduction, and oxidation.* Applied Physics B, 2008. **93**(2-3): p. 645-656.

267. Kock, B.F., et al., *Comparison of LII and TEM sizing during synthesis of iron particle chains.* Proceedings of the Combustion Institute, 2005. **30**(1): p. 1689-1697.

268. Leider, H., O. Krikorian, and D. Young, *Thermodynamic properties of carbon up to the critical point.* Carbon, 1973. **11**(5): p. 555-563.

269. Cignoli, F., et al., *Two-dimensional two-wavelength emission technique for soot diagnostics.* Applied Optics, 2001. **40**(30): p. 5370-5378.

270. Möllmann, K.-P., F. Pinno, and M. Vollmer, *Two-color or ratio thermal imaging-potentials and limits.* 2011.

271. Filippov, A., M. Markus, and P. Roth, *In-situ characterization of ultrafine particles by laser-induced incandescence: sizing and particle structure determination.* Journal of Aerosol Science, 1999. **30**(1): p. 71-87.

272. Bladh, H., et al., *Influence of soot particle aggregation on time-resolved laser-induced incandescence signals.* Applied Physics B, 2011. **104**(2): p. 331-341.

273. Butland, A. and R. Maddison, *The specific heat of graphite: an evaluation of measurements.* Journal of Nuclear Materials, 1973. **49**(1): p. 45-56.

274. Aguilar-Elguézabal, A., et al., *Study of carbon nanotubes synthesis by spray pyrolysis and model of growth.* Diamond and related materials, 2006. **15**(9): p. 1329-1335.

275. Genestoux, M., *Synthèse et optimisation de renforts hybrides nano-micro.* 2008.

276. Cheung, C.L., et al., *Diameter-controlled synthesis of carbon nanotubes.* The Journal of Physical Chemistry B, 2002. **106**(10): p. 2429-2433.

277. Jeong, G.-H., et al., *Size control of catalytic nanoparticles by thermal treatment and its application to diameter control of single-walled carbon nanotubes.* Applied physics letters, 2007. **90**(4): p. 043108.

278. Okuyama, K. and I. Wuled Lenggoro, *Preparation of nanoparticles via spray route.* Chemical Engineering Science, 2003. **58**(3): p. 537-547.

279. Nakaso, K., et al., *Synthesis of non-agglomerated nanoparticles by an electrospray assisted chemical vapor deposition (ES-CVD) method.* Journal of aerosol science, 2003. **34**(7): p. 869-881.

280. Taguchi, G., *Taguchi methods: design of experiments. American Supplier Institute.* Inc., MI, 1993.

281. Lewis, K.E. and G.P. Smith, *Bond dissociation energies in ferrocene.* Journal of the American Chemical Society, 1984. **106**(16): p. 4650-4651.

282. Kuwana, K. and K. Saito, *Modeling CVD synthesis of carbon nanotubes: Nanoparticle formation from ferrocene.* Carbon, 2005. **43**(10): p. 2088-2095.

283. Linteris, G., et al., *Flame inhibition by ferrocene and blends of inert and catalytic agents.* Proceedings of the Combustion Institute, 2000. **28**(2): p. 2965-2972.

284. Dormans, G., *OMCVD of transition metals and their silicides using metallocenes and (di) silane or silicon tetra-bromide.* Journal of crystal growth, 1991. **108**(3-4): p. 806-816.

285. Hirasawa, T., et al., *Effect of ferrocene addition on sooting limits in laminar premixed ethylene–oxygen–argon flames.* Combustion and Flame, 2004. **139**(4): p. 288-299.

286. Kuwana, K. and K. Saito, *Modeling ferrocene reactions and iron nanoparticle formation: Application to CVD synthesis of carbon nanotubes.* Proceedings of the Combustion Institute, 2007. **31**(2): p. 1857-1864.

287. Benson, S. and R. Shaw, *Kinetics and mechanism of hydrogenolyses. The*

addition of hydrogen atoms to propylene, toluene, and xylene. Journal of Chemical Physics, 1967. **47**: p. 4052-4055.

288. Endo, H., et al., *CFD prediction of carbon nanotube production rate in a CVD reactor.* Chemical Physics Letters, 2004. **387**(4): p. 307-311.
289. Kuwana, K., et al., *Catalyst deactivation in CVD synthesis of carbon nanotubes.* Carbon, 2005. **43**(2): p. 253-260.
290. Wasel, W., K. Kuwana, and K. Saito, *Chemical and thermal structures of a xylene-based CVD reactor to synthesize carbon nanotubes.* Chemical physics letters, 2006. **422**(4): p. 470-474.
291. Kiefer, J.H. and W.A. Von Drasek, *The mechanism of the homogeneous pyrolysis of acetylene.* International journal of chemical kinetics, 1990. **22**(7): p. 747-786.
292. Norinaga, K. and O. Deutschmann, *Detailed kinetic modeling of gas-phase reactions in the chemical vapor deposition of carbon from light hydrocarbons.* Industrial & engineering chemistry research, 2007. **46**(11): p. 3547-3557.
293. Dichiara, A. and J. Bai, *The growth of carbon nanotube multilayers on ceramic μ-particles by catalytic chemical vapour deposition.* Diamond and Related Materials, 2012. **29**: p. 52-58.
294. Schünemann, C., et al., *Catalyst poisoning by amorphous carbon during carbon nanotube growth: fact or fiction?* ACS nano, 2011. **5**(11): p. 8928-8934.
295. Mehedi, H.-a., et al., *Etching mechanism of diamond by Ni nanoparticles for fabrication of nanopores.* Carbon, 2013. **59**: p. 448-456.
296. He, D., *Formation of hybrid structures of carbon nanotubes and alumina microparticles by CVD method: Mechanisms and Chemical kinetics*. 2010, Ecole Centrale Paris.
297. He, D., H. Li, and J. Bai, *Experimental and numerical investigation of the position-dependent growth of carbon nanotube–alumina microparticle hybrid structures in a horizontal CVD reactor.* Carbon, 2011. **49**(15): p. 5359-5372.
298. Li, H., et al., *Chemical kinetics of catalytic chemical vapor deposition of an acetylene/xylene mixture for improved carbon nanotube production.* Carbon, 2010. **48**(15): p. 4330-4342.
299. Vanpaemel, J., et al., *Dual Role of Hydrogen in Low Temperature Plasma Enhanced Carbon Nanotube Growth.* The Journal of Physical Chemistry C, 2015. **119**(32): p. 18293-18302.
300. Vlassiouk, I., et al., *Role of hydrogen in chemical vapor deposition growth of large single-crystal graphene.* Acs Nano, 2011. **5**(7): p. 6069-6076.
301. Ionescu, M.I., et al., *Hydrogen-free spray pyrolysis chemical vapor deposition method for the carbon nanotube growth: parametric studies.* Applied surface science, 2011. **257**(15): p. 6843-6849.
302. Lee, G.-D., et al., *Catalytic decomposition of acetylene on Fe(001): A first-principles study.* Physical Review B, 2002. **66**(8).
303. Khalilov, U., A. Bogaerts, and E.C. Neyts, *Microscopic mechanisms of vertical graphene and carbon nanotube cap nucleation from hydrocarbon*

growth precursors. Nanoscale, 2014. **6**(15): p. 9206-14.

304. Sakurai, S., et al., *Role of subsurface diffusion and Ostwald ripening in catalyst formation for single-walled carbon nanotube forest growth.* Journal of the American Chemical Society, 2012. **134**(4): p. 2148-2153.
305. Zhang, H., et al., *Influence of ethylene and hydrogen flow rates on the wall number, crystallinity, and length of millimeter-long carbon nanotube array.* The Journal of Physical Chemistry C, 2008. **112**(33): p. 12706-12709.
306. Chiodarelli, N., et al., *Correlation between number of walls and diameter in multiwall carbon nanotubes grown by chemical vapor deposition.* Carbon, 2012. **50**(5): p. 1748-1752.
307. Jourdain, V., et al., *Controlling the morphology of multiwalled carbon nanotubes by sequential catalytic growth induced by phosphorus.* Advanced Materials, 2004. **16**(5): p. 447-453.
308. Hoecker, C., et al., *Catalyst nanoparticle growth dynamics and their influence on product morphology in a CVD process for continuous carbon nanotube synthesis.* Carbon, 2016. **96**: p. 116-124.
309. Leonhardt, A., et al., *Synthesis, Properties, and Applications of Ferromagnetic‐Filled Carbon Nanotubes.* Chemical vapor deposition, 2006. **12**(6): p. 380-387.
310. Elihn, K. and K. Larsson, *A theoretical study of the thermal fragmentation of ferrocene.* Thin solid films, 2004. **458**(1): p. 325-329.
311. Dresselhaus, M., A. Jorio, and R. Saito, *Characterizing graphene, graphite, and carbon nanotubes by Raman spectroscopy.* Annu. Rev. Condens. Matter Phys., 2010. **1**(1): p. 89-108.
312. Behr, M.J., et al., *Hydrogen etching and cutting of multiwall carbon nanotubes.* Journal of Vacuum Science & Technology B, 2010. **28**(6): p. 1187-1194.
313. Zhang, R., et al., *Nanostructure dependence of field-effect mobility in regioregular poly (3-hexylthiophene) thin film field effect transistors.* Journal of the American Chemical Society, 2006. **128**(11): p. 3480-3481.
314. Bianco, A., et al., *Eu-doped titania nanofibers: processing, thermal behaviour and luminescent properties.* Journal of nanoscience and nanotechnology, 2010. **10**(8): p. 5183-5190.
315. Moon, M., et al., *Dithienogermole‐Containing Small‐Molecule Solar Cells with 7.3% Efficiency: In‐Depth Study on the Effects of Heteroatom Substitution of Si with Ge.* Advanced Energy Materials, 2015. **5**(9).
316. Chase, M.W., Jr., *NIST-JANAF Thermochemical Tables, Fourth Edition, J. Phys. Chem. Ref. Data, Monograph 9, 1998, 1-1951.*
317. Chao, J., K.R. Hall, and J.-M. Yao, *Chemical thermodynamic properties of toluene, o-, m-and p-xylenes.* Thermochimica acta, 1984. **72**(3): p. 323-334.
318. Draeger, J., *The methylbenzenes II. Fundamental vibrational shifts, statistical thermodynamic functions, and properties of formation.* The Journal of Chemical Thermodynamics, 1985. **17**(3): p. 263-275.
319. *Selected Values of Properties of Chemical Compounds., Thermodynamics Research Center, Texas A&M University, College Station, Texas*. 1997.